Aerodynamics of vertical-axis wind turbines in full-scale and laboratory-scale experiments

Thesis by

Daniel Borsodi Araya

In Partial Fulfillment of the Requirements

for the Degree of

Doctor of Philosophy

California Institute of Technology

Pasadena, California

2016

(Defended November 13, 2015)

© 2015

Daniel Borsodi Araya

All Rights Reserved

Acknowledgments

The completion of this thesis marks the end of my journey at Caltech. I would sum up my experience by saying that the standards for success were set very high, but equally high was the support that I received from many brilliant people who wanted me to succeed.

I am especially grateful to my advisor, John Dabiri, for showing me how to think like a scientist and how to lead others with compassion. I have enjoyed my brief time in his research group, which has introduced me to many new and long-lasting friendships. I am indebted to Matthias Kinzel, Janna Nawroth, Monica Martinez Wilhelmus, Robert Whittlesey, Clara O'Farrell, Ian Brownstein, Kristy Schlueter, and Roberto Zenit, who have all had some influence in my work.

I am also fortunate to have had a close working relationship with my candidacy committee, including Beverley McKeon, Tim Colonius, and Mory Gharib. Their sage advice helped to shape my research path and many of their suggestions are reflected in the better parts of this thesis. I am also deeply grateful to Tony Leonard for joining my thesis committee and making valuable contributions to the final text.

Financial support was granted to me through graduate research fellowships with the National Science Foundation (GRFP), the Department of Defense (NDSEG), and the Resnick Sustainability Institute at Caltech, all of which have given me a great amount of freedom in my research activities. Partial support through grants to J.O.D by the Office of Naval

Research (N000141211047) and the Gordon and Betty Moore Foundation (No. GBMF2645) is also gratefully acknowledged.

Additionally, I would like to expressly thank Guruswami 'Ravi' Ravichandran for his personal guidance and exceptional leadership, along with my peers at Caltech who have demonstrated kindness and solidarity throughout my time there.

Finally, I owe more than I can express to my wife, Carolina, who has now lived through graduate school twice, a feat in and of itself. These years have been trying for both of us, and she deserves much praise and admiration for her strength through it all. To my daughter, Leila, and my son, Oliver, if you read this later, know that your laughter has brought me a great amount of joy, and that you single-handedly taught me the importance of a balanced life.

Abstract

Within a wind farm, multiple turbine wakes can interact and have a substantial effect on the overall power production. This makes an understanding of the wake recovery process critically important to optimizing wind farm efficiency. Vertical-axis wind turbines (VAWTs) exhibit features that are amenable to dramatically improving this efficiency. However, the physics of the flow around VAWTs is not well understood, especially as it pertains to wake interactions, and it is the goal of this thesis to partially fill this void. This objective is approached from two broadly different perspectives: a low-order view of wind farm aerodynamics, and a detailed experimental analysis of the VAWT wake.

One of the contributions of this thesis is the development of a semi-empirical model of wind farm aerodynamics, known as the LRB model, that is able to predict turbine array configurations to leading order accuracy. Another contribution is the characterization of the VAWT wake as a function of turbine solidity. It was found that three distinct regions of flow exist in the VAWT wake: (1) the near wake, where periodic blade shedding of vorticity dominates; (2) a transition region, where growth of a shear-layer instability occurs; (3) the far wake, where bluff-body oscillations dominate. The wake transition can be predicted using a new parameter, the dynamic solidity, σ_D, which establishes a quantitative connection between the wake of a VAWT and that of a circular cylinder. The results provide insight into the mechanism of the VAWT wake recovery and the potential means to control it.

Contents

Acknowledgments **iii**

Abstract **v**

1 Introduction **1**

1.1 Motivation 1

1.2 A brief overview of VAWTs 2

1.3 Scope of the current work 3

2 Low-order modeling of wind farm aerodynamics using leaky Rankine bodies (LRBs) **5**

2.1 Introduction 5

2.2 Analytical model 9

2.3 Experimental Methods 12

2.3.1 Field site and wind turbines 12

2.3.2 Wind velocity measurements 13

2.3.3 Power measurements 14

2.3.4 LRB Model Calibration 18

2.4 Results 20

2.4.1 LRB model prediction of individual turbine performance 20

2.4.2 LRB model prediction of turbine array performance 24

2.4.3 Robustness of LRB model prediction of array performance 28

2.5 Conclusions 30

3 A comparison of measurements in motor-driven and flow-driven turbine experiments 32

3.1 Introduction 32

3.2 Description of experimental test cases 34

3.2.1 Flow-driven turbine 34

3.2.2 Motor-driven turbine 36

3.3 Experimental Setup 38

3.3.1 Model turbine 38

3.3.2 Water channel facility 39

3.3.3 Diagnostics 40

3.4 Experimental procedure 43

3.4.1 Turbine neutral curve 43

3.4.2 PIV measurement conditions 44

3.4.3 Calculation of wake statistics 47

3.4.4 PIV error analysis 50

3.5 Results 50

3.5.1 PIV measurements on or below the neutral curve 50

3.5.2 Measurements on or above the neutral curve 58

3.5.3 Circulation and torque measurements 59

3.6 Conclusion 62

4 Transition to bluff body dynamics in the wake of vertical-axis wind turbines **64**

4.1 Introduction 64

4.2 Experimental methods 67

4.2.1 Turbine rotor and cylinder geometry 67

4.2.2 PIV setup 67

4.2.3 Experimental procedure 69

4.2.4 Turbine and cylinder power coefficient, C_p 71

4.2.5 PIV measurement conditions 73

4.2.6 Calculation of wake statistics 73

4.3 Results & discussion 76

4.3.1 PIV measurements for load-free shaft conditions 76

4.3.2 PIV measurements for loaded-shaft conditions 85

4.3.3 Dynamic solidity of a VAWT 85

4.3.4 Effect of dynamic solidity on wake transition 89

4.3.5 Effect of dynamic solidity on velocity recovery 92

4.3.6 Insight into three-dimensional effects 98

4.3.7 Rotating cylinder comparison 100

4.4 Concluding remarks 104

5 Summary and future work **106**

5.1 Summary of thesis contributions 106

5.2 Avenues for future work 108

Chapter 1

Introduction

1.1 Motivation

> *"While poets and song writers say it is love that makes the world go round, and bankers say it is money, it is really energy that makes the world go round. Energy heats our homes, cooks our food, lights our evenings, powers our transportation, runs our industries, powers our communications, and drives our digital world."*
>
> - Burton Richter (2014)

The underlying motivation of this thesis is a desire to advance the technology necessary for a sustainable energy future. While there is ongoing debate about the sustainability of fossil fuel reserves to meet the rising global demand for energy, there is diminishing doubt that the cumulative effect of CO_2 emissions from burning these fuels is having a detrimental impact on the global climate (see, e.g., Raupach *et al.*, 2007). The issue is so pressing that it has risen to the forefront of global politics, most recently with U.S. President Obama putting forward 'The Clean Power Plan' to take action on limiting CO_2 emissions in the United States (U.S. Environmental Protection Agency, 2015).

Harvesting wind energy is a socially responsible alternative to fossil fuels, but key challenges remain that must be overcome in order to access its full potential. One such challenge is the mitigation of performance losses within a wind farm due to turbulent wake interactions among individual wind turbines. Porté-Agel *et al.* (2013) demonstrated this wake loss effect in a case study of the Horns Rev wind farm, which consisted of 80 2MW horizontal-axis wind turbines (HAWTs) within an area of 20km^2. They showed that a change in wind

direction of just 10° was enough to affect the total wind farm power output by as much as 43%. Modern HAWT farms are designed to minimize these wake losses by spacing individual turbines far apart, typically 3-5 rotor diameters (D) in the crosswind direction and 6-10 D in the streamwise direction (Hau, 2005). Meyers & Meneveau (2012) suggested an even larger streamwise spacing of approximately 15 D in order to optimize performance. While this strategy of placing turbines far apart is simple and may be effective in maximizing the performance of individual turbines, it is fundamentally limited by the availability of land, which can be significantly constrained by geographic and even political limitations (Haggett, 2008). Furthermore, it effectively neglects the problem of wake interactions among turbines altogether.

In contrast, Kinzel *et al.* (2012) demonstrated that a full-scale array of counter-rotating vertical-axis wind turbines (VAWTs), with spacing as small as 1.65 D in the crosswind direction, could achieve a power density of 24 Wm^{-2} for the overall planform area of the array, approximately 10 times greater than the power density of typical HAWT arrays. This provides evidence to suggest that the wake interactions among individual VAWTs could improve, rather than purely diminish, the overall performance of an array. Exploiting such constructive wake interactions would represent a paradigm shift in the design of efficient wind farms. However, a major difficulty lies in the fact that the aerodynamics of the VAWT wake is not well understood, and thus provides an opportunity for further investigation.

1.2 A brief overview of VAWTs

A VAWT is a wind turbine that rotates on an axis perpendicular to the incident flow. This is contrary to the HAWT design, where the axis of rotation is aligned parallel to the incident flow. The physical mechanism that drives the rotation of the two turbine designs is the same: lift and drag are generated by the individual turbine blades, which in turn produce a net torque that is typically transferred to an electrical generator, thus extracting energy from the flow. Two major advantages of the VAWT design are an insensitivity to wind direction, eliminating the need for a yaw system, and the ability to mount the power generation equipment near the ground, potentially saving on operationals costs.

The practical use of VAWTs dates back to at least the 9th century AD (al Hassan & Hill, 1986). Despite this history, VAWTs have not seen as much commercial success as HAWTs in modern times, and a consequence of this has been a lag in the literature focused on improving their design. In the U.S., a great deal of work was done to develop VAWT technology at Sandia National Laboratories beginning in the 1970's and concluding in the 1990's; a comprehensive review of the lessons learned from that work is given by Sutherland *et al.* (2012). The authors of this review note that VAWTs fell out of favor within the wind turbine community in the mid-1990's after the downfall of FloWind Corporation, a private company that partnered with Sandia and other government agencies to try to commercialize VAWT technology. Only within the last 5-10 years, with a global resurgence of investment into sources of alternative energy, has interest again shifted to VAWTs, predominately because of their aforementioned mechanical advantages. Still, much of the VAWT development has focused on its mechanical design. Studying the flow characteristics of VAWTs, and in particular groups of VAWTs, is a crucial step needed toward optimizing their performance within a wind farm.

1.3 Scope of the current work

The remainder of this manuscript is composed mainly of two peer-reviewed journal articles as well as a third article currently under review, all written by the thesis author. Contributions made by co-authors are noted in the text. The comprehensive aim of this body of work is to provide insight into the aerodynamics of VAWTs using a combination of full-scale field measurements, modeling, and laboratory-scale experiments.

The text is presented in chronological order, beginning in Chapter 2 with a broad look at wind farm aerodynamics. Here it is shown how a low-order potential flow model can be composed for a VAWT wind farm that has sufficient accuracy to rank the performance among unique arrays of turbines, all of which is supported by full-scale field measurements. While of high value, the field measurements were limited in spatial fidelity to several single-point measurements collected over a series of weeks with weather and operational constraints taken into consideration. This restricted the VAWT wake analysis and prompted an interest

in more controlled laboratory-scale experiments. Chapter 3 introduces these experiments by a detailed account of the practical use of a motor when kinematic similarity is of primary concern in investigations of wind turbine aerodynamics. The result of this analysis is then applied to more comprehensive laboratory-scale experiments presented in Chapter 4, where the characteristics of the near and far wake of a VAWT is explored in detail. Specifically, the velocity in the wake of three different turbine models is compared against that of a circular cylinder of the same aspect ratio. The subsequent analysis leads to the establishment of a quantitative connection between the cylinder and VAWT wake using a newly-defined parameter, the dynamic solidity. The results also demonstrate a link between the dynamic and steady characteristics of the VAWT wake, which has important implications for power production within a wind farm. Finally, Chapter 5 summarizes the contributions of this thesis and suggests potential avenues for future research.

Chapter 2

Low-order modeling of wind farm aerodynamics using leaky Rankine bodies (LRBs)

The material presented in this chapter was authored by Araya *et al.* (2014) and published in *J. Renewable Sustainable Energy* **6** : 063118. The contributions of each author were the following: D.B.A. and J.O.D. developed the LRB model, which followed the conceptual framework established by A.E.C. and J.O.D. in a senior thesis at Caltech. M.K. worked with D.B.A. to collect the field data and aided in its analysis. D.B.A performed the final analysis of the field data, conducted the LRB simulations, and prepared the manuscript. J.O.D. advised and made final edits to the manuscript. Some minor revisions to the published text have been made here in order to incorporate it with the rest of this thesis.

2.1 Introduction

There is a persistent need for simple yet reliable models of wind turbine aerodynamics that can aid in the design of wind farms. Originating with the work of Rankine (1865), actuator disk theory is perhaps the most widely used example of such a model (see, e.g., Yang *et al.*, 2014; Spera, 2009; Hansen *et al.*, 2006). It represents an individual turbine rotor as an infinitely thin permeable disk whose extent is defined by the rotor swept area. The energy extraction process is idealized to take place at the disk, resulting in induced streamwise velocity variations ahead of and behind the turbine. Betz (1920) used this concept along with one-dimensional linear momentum theory and Bernoulli's principle to

derive the well-known theoretical limit to the amount of energy that can be extracted from the flow upstream of a HAWT, which is approximately 59%. Lissaman (1979) also used linear momentum theory and a semi-empirical wake model to investigate the performance of large arrays of HAWTs by superposing multiple model wakes together. A numerical sensitivity analysis showed the effects of streamwise and crosswind HAWT spacing as well as ambient turbulence, turbine hub height ratio, and other turbine characteristics on array performance (Lissaman *et al.*, 1982). This work demonstrated that streamwise spacing and ambient turbulence are primary factors that determine array efficiency.

As noted in Chapter 1, modern wind farms are typically composed of HAWTs that are spaced far apart in an effort to mitigate performance losses due to turbine wake interactions. While large HAWT spacing may optimize the power production of each turbine in the array, it potentially reduces the amount of power that can be extracted from a given wind farm footprint. The footprint power density can be an important design constraint in areas where land is limited, such as near population centers, or where the source of wind is isolated to a narrow region of terrain, such as along a ridgeline or shoreline. VAWTs have recently been suggested to achieve higher turbine power output per unit land area than HAWTs (Dabiri, 2011; Kinzel *et al.*, 2012). This is in part due to the fact that, unlike for HAWTs, it is possible to increase the swept area of a VAWT independent of its footprint. Despite the more complex aerodynamics of VAWTs as compared to HAWTs, there have been significant efforts made to improve the modeling of VAWT aerodynamics. The methods, mostly developed in the 1970s, can be classified into three categories: 1) momentum methods, including variants of single and multiple streamtube models; 2) vortex methods, where the effect of the turbine on the flow is modeled using sheets of discrete vorticity; and 3) local-circulation methods, which include some of the features of the other two methods. Detailed summaries of each of the methods are given by Touryan *et al.* (1987) and also in a more recent review by Islam *et al.* (2008). Of particular note is the work of Templin (1974), who introduced a single streamtube model for VAWTs, following the same actuator disk theory used by Betz. Specifically, the streamwise forces on the VAWT rotor blades are equated to the change in streamwise wind momentum. This results

in an induced velocity that is assumed to be constant through the rotor, which is itself replaced by an equivalent actuator disk. Computational work by Martinelli & Smits (2012), Shamsoddin & Porté-Agel (2014), and Tsai & Colonius (2014), to name a few, has made progress toward numerical techniques well-suited for the analysis of the flow around VAWTs. These numerical tools aid in developing a better physical understanding of the VAWT wake dynamics, which ultimately leads to more efficient wind farm designs.

Despite the existence of a variety of aerodynamic models and increasing simulation efforts for individual VAWTs, there is rather limited literature on the performance of arrays of VAWTs. Rajagopalan *et al.* (1990) examined the performance of clusters of co-rotating VAWTs by idealizing the rotors as momentum sources in a two-dimensional incompressible flow field. They concluded that the physical positioning of the VAWTs relative to each other had a significant effect on their aerodynamic performance, and that downwind turbine performance within an array could be improved by judicious selection of the turbine positions to maximize the overall array performance. Another VAWT array study was conducted by Whittlesey *et al.* (2010), who showed by a semi-empirical analysis based on potential flow theory that an order-of-magnitude improvement in footprint power density was possible for wind farms composed of counter-rotating VAWT pairs. This was subsequently supported in full-scale experiments by Dabiri (2011), and additional full-scale experiments have shown that this arrangement of VAWTs allows for a reduction in the average inter-turbine spacing relative to HAWT arrays (Kinzel *et al.*, 2012). What is lacking, however, is a reliable means to predict the array configurations that would optimize this performance.

It is worth noting that the suggestion of exploiting positive aerodynamic interference effects to boost wind farm performance is not limited to VAWT arrays. Ammara *et al.* (2002) adopted a similar approach to that proposed by Rajagopalan *et al.* (1990) in their study of HAWTs. Their numerical study revealed that similar positive interference effects can be present in HAWT arrays, such that a strategically-designed dense array could produce energy at levels similar to those of a sparse arrangement.

Due to the sensitivity of the overall wind farm efficiency to its layout, identifying the optimal design by experiment alone would be impractical due to the time and expense involved.

The practical alternative that most optimization studies for HAWT farms have employed is the use of simplified models either as standalone predictive tools (e.g., Marmidis *et al.*, 2008) or embedded within higher fidelity numerical simulations (e.g., Meyers & Meneveau, 2012). The latter work incorporates knowledge about the complex turbulent flow patterns within a wind farm, which have been shown to be important in the vertical transport of energy (Calaf *et al.*, 2010). A wind tunnel study by Chamorro & Porté-Agel (2010) on the effects of thermal stability and incoming boundary layer flow characteristics on HAWT wakes demonstrated that the velocity deficit at hub height along the center of the wake was key to the characterization of the overall wake and that its adequate prediction was essential in order to assess performance.

This prior experience in optimizing HAWT array performance motivates our work to develop a simple model to discover and characterize optimal VAWT arrays. We present an application of actuator disk theory for VAWTs within the framework of two-dimensional potential flow theory. Potential flows in general, and source distribution methods in particular, have been used extensively in both naval hydrodynamics (see, e.g., Dawson, 1977; Zhang *et al.*, 2009) and airplane aerodynamics (see, e.g., the review by Hess, 1990) to model inviscid flow past bluff bodies. In the latter review, the author points out that the predictions of such methods have been found to agree well with experiments over a large range of flow conditions. In addition, even when the results do not agree quantitatively with experiments, they are frequently useful in predicting the incremental effect of a proposed design change or in ordering various designs in terms of effectiveness, which is arguably the level of fidelity most useful in a wind farm layout optimization study.

The remainder of this chapter is organized as follows: section 2.2 describes the analytical potential flow model; section 2.3 describes the full-scale field measurements used to validate the model; section 2.4 compares the model predictions with field measurements; and finally, section 2.5 summarizes and discusses the contributions of this work.

2.2 Analytical model

The flow around an isolated VAWT is approximated by using a two-dimensional potential flow model consisting of a uniform flow, a potential source, and a potential sink. This can be expressed mathematically by the complex velocity, $W(z)$:

$$W(z) = V_\infty e^{-i\alpha} + \left[\frac{m_{so}}{2\pi z} - \frac{m_{si}}{2\pi(z - z_s)}\right], \tag{2.1}$$

where V_∞ is the magnitude of the freestream velocity, α is the freestream angle of incidence, and m_{so} and m_{si} are the source and sink strength, respectively. The source denotes the center of the conceptual VAWT, and it is located at the origin; z_s is the downstream position of the sink. The resulting velocity vector at a point in the flow is $\mathbf{V}(z) = \Re(W)\hat{\mathbf{x}} - \Im(W)\hat{\mathbf{y}}$, where $\hat{\mathbf{x}}$ and $\hat{\mathbf{y}}$ are Cartesian unit vectors.

When the source and sink are of equal strength, closed streamlines are formed in the shape of what is known as a Rankine body. In the present work, we define a "leaky Rankine body" (LRB) that is analogous to the Rankine body, but with a sink that is stronger than the source. The relative strengths of the source and sink are determined by the VAWT power coefficient as described below. A representative comparison between the streamlines around a Rankine body and an LRB with the same source strength and downstream spacing from source to sink (but different sink strength) is shown in Figure 2.1. Note that the Rankine body is shaded as a black ovoid in Figure 2.1(a) and that an individual VAWT is shaded as a black circle in Figure 2.1(b) with a diameter equal to the rotor diameter. To model an array of VAWTs, a superposition of individual LRBs is used. Figure 2.1(c) shows representative streamlines around a pair of VAWTs. The LRB streamlines have a qualitatively similar appearance to the separated wake of a bluff body. This is used presently to model the effect of each VAWT wake on other VAWTs within an array.

The LRB model implicitly assumes that the flow around each VAWT is steady and irrotational everywhere. The assumption of steady flow is reasonable to first order since the turbine output power typically scales cubically with the mean wind speed at hub height (Hau, 2005). The assumption of irrotational flow is frequently used in high Reynolds num-

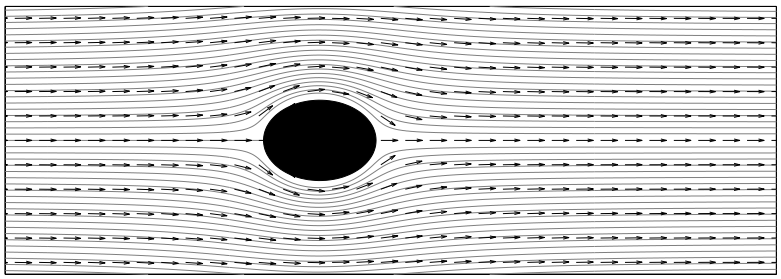

(a)

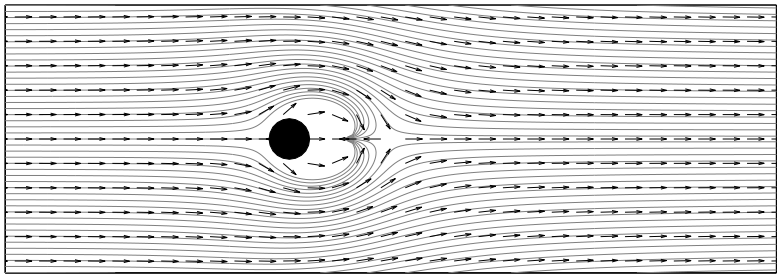

(b)

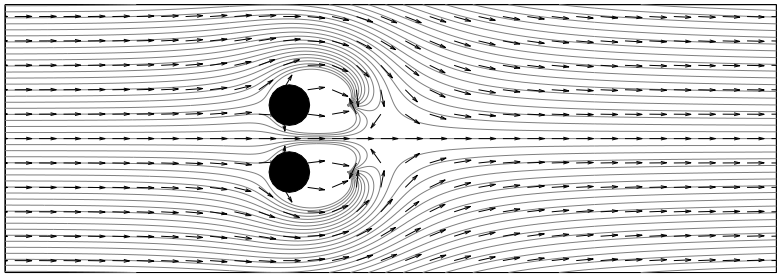

(c)

Figure 2.1: (a) Streamlines formed by a source and sink of equal strength separated by distance s_s. Closed streamlines are shaded with a solid black ovoid, which is known as a Rankine body. (b) LRB streamline pattern formed by a source and sink separated by distance s_s. The sink strength in figure (b) is greater than in (a) with all other parameters the same. The solid black circle indicates the size and position of the VAWT that is modeled. (c) Streamlines formed by the superposition of two LRB models.

ber flows with limited separation, but is known to lead to an erroneous prediction of zero net drag for any body formed by a closed streamline that encloses all singularities (Batchelor, 1967). Hence, if a classical Rankine body were used for the VAWT model, the zero drag prediction would imply that the model turbine does not exchange energy with the flow. However, a branch of potential flow theory known as free-streamline theory has been successfully employed to estimate the drag and shape of the steady wake in cavity flows (Birkhoff & Zarantonello, 1957) and behind bluff bodies (Wu, 1962). More recently, another potential flow model known as the Föppl point vortex system has been used to study vortex dynamics and control for solid bodies (Protas, 2008; Vasconcelos *et al.*, 2011). An underlying assumption of both the Föppl system and free-streamline theory is that a non-zero drag on a body in potential flow requires that a wake region be modeled explicitly; this is a feature of the LRB model. More precisely, it can be shown that there exists a finite force required to hold a source or a sink in place within a uniform flow (Milne-Thomson, 1960). Since the LRB model produces a net sink flow within a uniform flow, the force required to hold these singularities in place is an analogous representation of the drag on the turbine. Thus, the model is similar in physical principle to the actuator disk concept.

The LRB model for an isolated VAWT is fully specified by three parameters: the source strength m_{so}, sink strength m_{si}, and downstream spacing from source to sink s_s. The source and sink strength are determined by application of Bernoulli's equation and the conservation of mass and momentum (i.e., actuator disk theory) to specify the speed of the flow upstream of each turbine (i.e., U_2) and in its far wake (i.e., U_4). Given the freestream speed U_1, it can be shown that $U_2 = U_1(1-a)$ and $U_4 = U_1(1-2a)$, where the induction factor $a \equiv (U_1 - U_2)/U_1$ is determined from the turbine power coefficient $C_p = 4a(1-a)^2$. Thus the primary input to the model is the nominal individual VAWT efficiency. For a given freestream speed U_1, and induction factor a, the LRB model parameters are related by the following linear system of equations:

$$\begin{aligned} -aU_1 &= -\frac{m_{so}}{2\pi r_u} + \frac{m_{si}}{2\pi(r_u + s_s)} \\ -2aU_1 &= \frac{m_{so}}{2\pi r_w} - \frac{m_{si}}{2\pi(r_w - s_s)}, \end{aligned} \tag{2.2}$$

where r_u and r_w are the nominal positions of the upstream and far wake flow speeds, respectively. The sink spacing s_s, however, remains as a free parameter in this model and is calibrated presently by a least-squares fit to velocity data collected in the field. In the results that follow, the VAWT efficiency is taken as nominally 10%, which is consistent with the field data. The upstream position is set at 3 D in front of each turbine and the far wake is 10 D downstream. It is shown later that the model is relatively insensitive to different quantitative choices for all of the aforementioned input parameters. To be sure, the model does begin to exhibit discrepancies with the field data if the upstream point is less than approximately 3 D away from the turbine, due to the effect of the singularity (i.e., the source) located at the turbine axis.

In the present work, individual VAWTs are located on a Cartesian grid with 0.15 D resolution in the x-y plane. The turbine spacing mimics the configuration of VAWTs described in the experimental methods section below. Because the power produced by each turbine is proportional to the cube of the upstream wind speed, the performance of each array is quantified by the average value of U_2^3 over all of the turbines in the array. A more detailed development of the LRB model and its connection to actuator disk theory is given in appendix A.

2.3 Experimental Methods

2.3.1 Field site and wind turbines

Field measurements of an array of full-scale VAWTs (Windspire Energy Inc.) were conducted in the Antelope valley of northern Los Angeles County in California, USA from 2011 to 2013. The layout of the facility is shown in the photograph in Figure 2.2. The VAWT array was initially composed of nine counter-rotating turbine pairs arranged on an equidistant grid spaced 8 D apart with the turbines in each pair separated center-to-center by 1.65 D. Six additional turbines were added subsequently, of which one was used in a study described below. The VAWTs have a lift-based rotor design consisting of three airfoil blades and a rated power output of 1.2 kW. The total height of each turbine is 9.1 m with a rotor height of 6.1 m and a diameter of 1.2 m. The nominal cut-in and cut-out speeds of

the turbines are 4 ms^{-1} and 12 ms^{-1}, respectively. The turbines operate at a rotation rate of approximately 350 rpm and a tip speed ratio of 2.3 in incident winds of 8 ms^{-1}. Further discussion of the measurements in relation to atmospheric conditions are given in Kinzel *et al.* (2012).

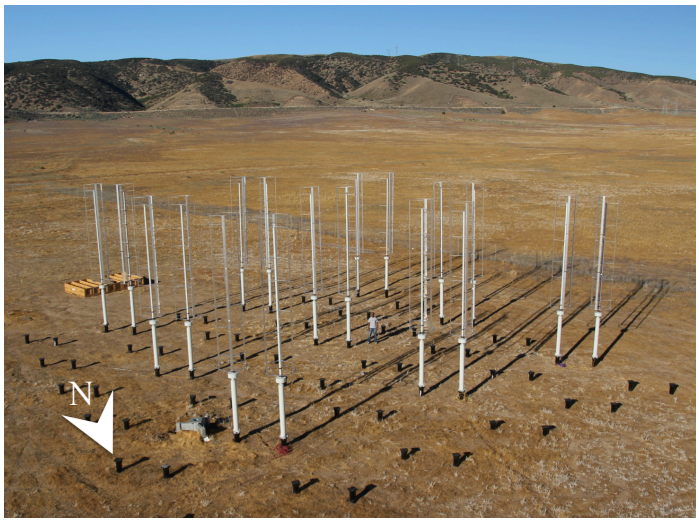

Figure 2.2: Photograph of the experimental VAWT array.

2.3.2 Wind velocity measurements

Wind velocity was measured using seven three-component ultrasonic anemometers (Campbell Scientific CSAT3) mounted on a 10 m meteorological tower (Aluma-Towers Inc.) and vertically spaced in 1 m increments over the turbine rotor height. The CSAT3 sensors were operated at a sampling frequency of 10 Hz with a measurement uncertainty of 0.161 ms^{-1}. Both the sensors and the data logger (Campbell Scientific CR3000) were powered by a solar panel and battery system to make the apparatus fully portable. An additional reference meteorological tower was positioned southeast of the array. This 10 m tower continuously recorded both wind speed and direction at ten-minute intervals using a cup anemometer (Thies First Class). The data was subsequently uploaded to a database via satellite link.

Vertical profiles of wind velocity were measured at nine positions along the centerline of a four-turbine array as indicated in Figure 2.3 (a). The four turbines were aligned with a southwesterly wind direction and the measurement duration at each position was approximately 150 h. Data was also collected with all eighteen turbines erected. During this

period, vertical profiles of wind velocity were measured at four positions along the centerline of the array as shown in Figure 2.3 (b). For both measurement periods, the prevailing wind direction was from the southwest. For each meteorological tower position, the data was first conditioned to include only wind directions between $215° - 235°$. The measured streamwise velocity was then normalized by the reference tower streamwise velocity and averaged spatially over the seven sensors and in time. This resulted in one normalized streamwise velocity measurement, U, per measurement location. For comparison with the LRB model, this normalized velocity U at the array centerline position $A_{CL}/D = -15$ in Figure 2.3 (b) was used as the normalized freestream velocity, i.e., U_∞.

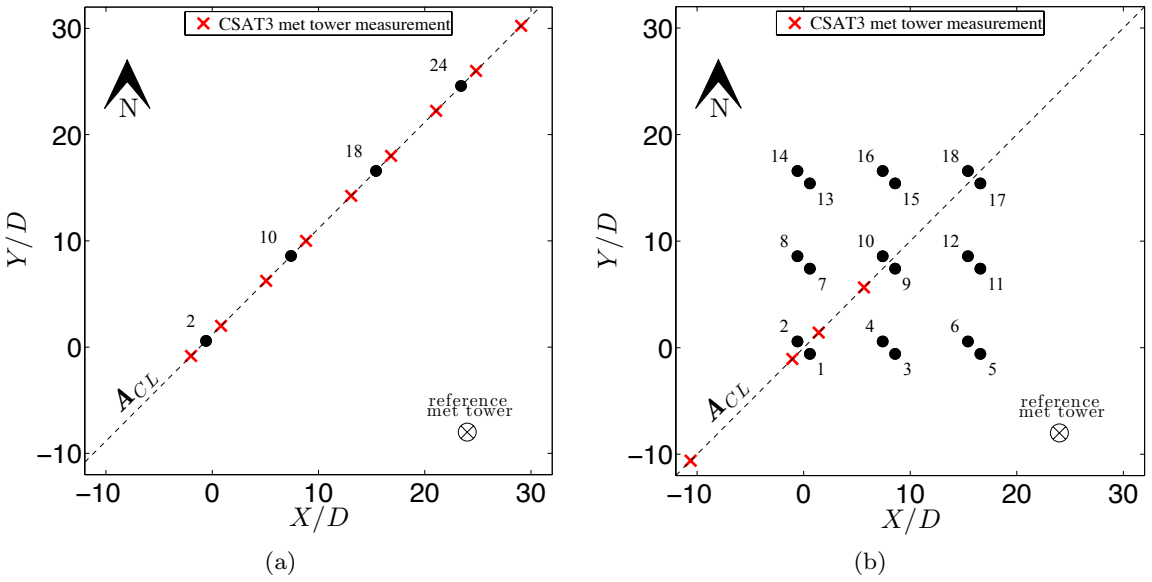

Figure 2.3: (a) Schematic top view of the four VAWT array, (b) Schematic top view of the eighteen VAWT array. VAWTs are drawn to scale with black circles and numbered individually. Velocity measurement positions are indicated by red X's. The position of the reference meteorological tower is not drawn to scale. The axis dimensions are given in rotor diameters where $D = 1.2$ m.

2.3.3 Power measurements

Turbine output power was continuously recorded to a Campbell Scientific data logger (CR3000) at ten-minute intervals and then uploaded to a database via satellite link. The power data was conditioned to examine the performance among individual turbines within the 4-turbine array and also the 18-turbine array. The average performance between five

12-turbine subsets of the 18-turbine array was also examined as described below. For each ten-minute power measurement, the power coefficient, $C_p = P/\frac{1}{2}\rho A V_\infty^3$, was calculated for each turbine. Here P is the power produced by the turbine, $\rho = 1.2$ kgm^{-3} is the density of air, $A = 7.3$ m^2 is the projected area of the rotor, and V_∞ is the reference meteorological tower wind speed.

Figure 2.4 (a) shows a box plot of the power coefficient for each of the four turbines when all four turbines were simultaneously operational. In this case, power data was only included for wind speeds between 6-10 ms^{-1}, but all wind directions were allowed in order to examine its effect on performance. A radial histogram of wind direction for this case is shown in Figure 2.4 (c), which also indicates the number of hours of power data collected. The effect of wind direction on turbine performance was obtained by comparing the mean C_p of each turbine for wind directions between $185^\circ - 210^\circ$, $210^\circ - 235^\circ$, $235^\circ - 260^\circ$, $260^\circ - 285^\circ$, and $285^\circ - 310^\circ$. A paired Student's t-test was used to evaluate the statistical significance of each comparison. The result was considered statistically significant if the null hypothesis, i.e., that the difference between the two mean values of C_p was due to random variation, could be rejected with greater than 95% confidence. For the case of the eighteen-turbine array, the power coefficient for each turbine when all turbines were simultaneously operational is shown in Figure 2.4 (b). In this case, power data was only included for wind speeds between 6-10 ms^{-1} and wind direction between $215^\circ - 235^\circ$. The corresponding radial histogram is shown in Figure 2.4 (d). Individual turbine performance was examined by calculating an average C_p for each turbine and performing a paired t-test between that turbine and each of the other seventeen turbines.

Because not all eighteen turbines were continuously operational during the measurement campaign (e.g., due to turbine maintenance), the field measurements also characterized various configurations composed of subsets of the eighteen turbines. We identified five unique array configurations with twelve VAWTs producing power during similar wind conditions (i.e., wind speeds between 6-10 ms^{-1} and wind direction between $215^\circ - 235^\circ$). These five unique array configurations, shown schematically in Figure 2.5, were selected for detailed analysis of relative array performance. It was observed that turbines 1 and 2 at the front of

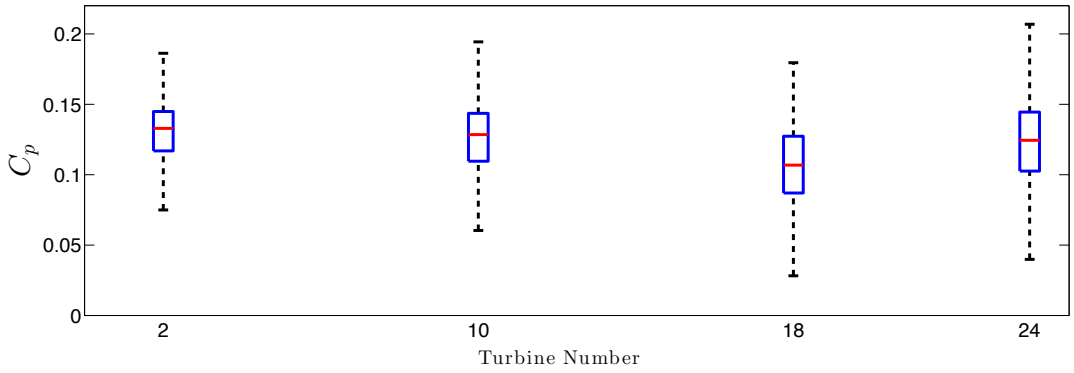

(a)

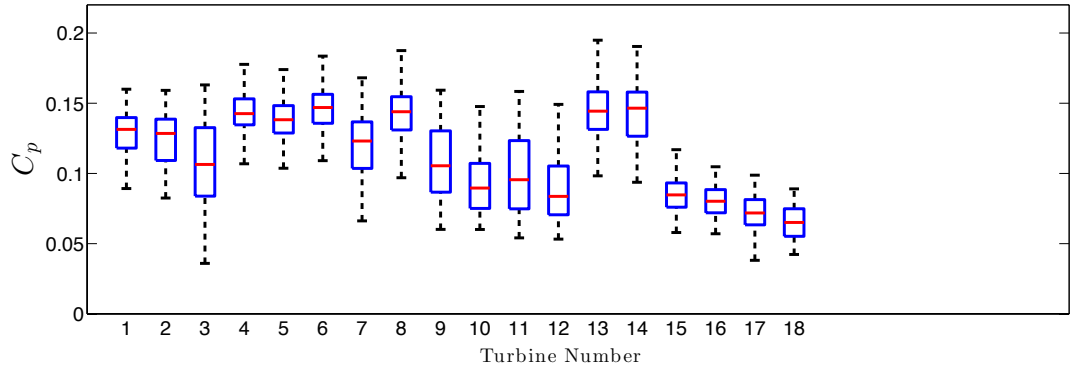

(b)

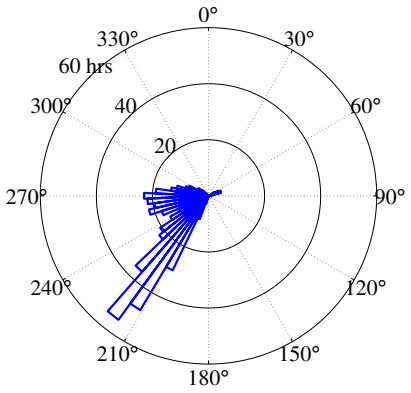

(c)

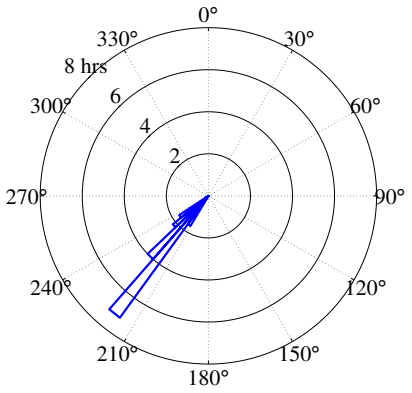

(d)

Figure 2.4: Box plot of individual turbine power coefficient (a) when four turbines are operational for all wind directions, and (b) when eighteen turbines are operational and wind direction is between $215° - 235°$.(c) Wind rose in degrees from due north for the four-turbine array, and (d) the eighteen-turbine array. Wind speeds are between 6-10 ms^{-1} for both cases.

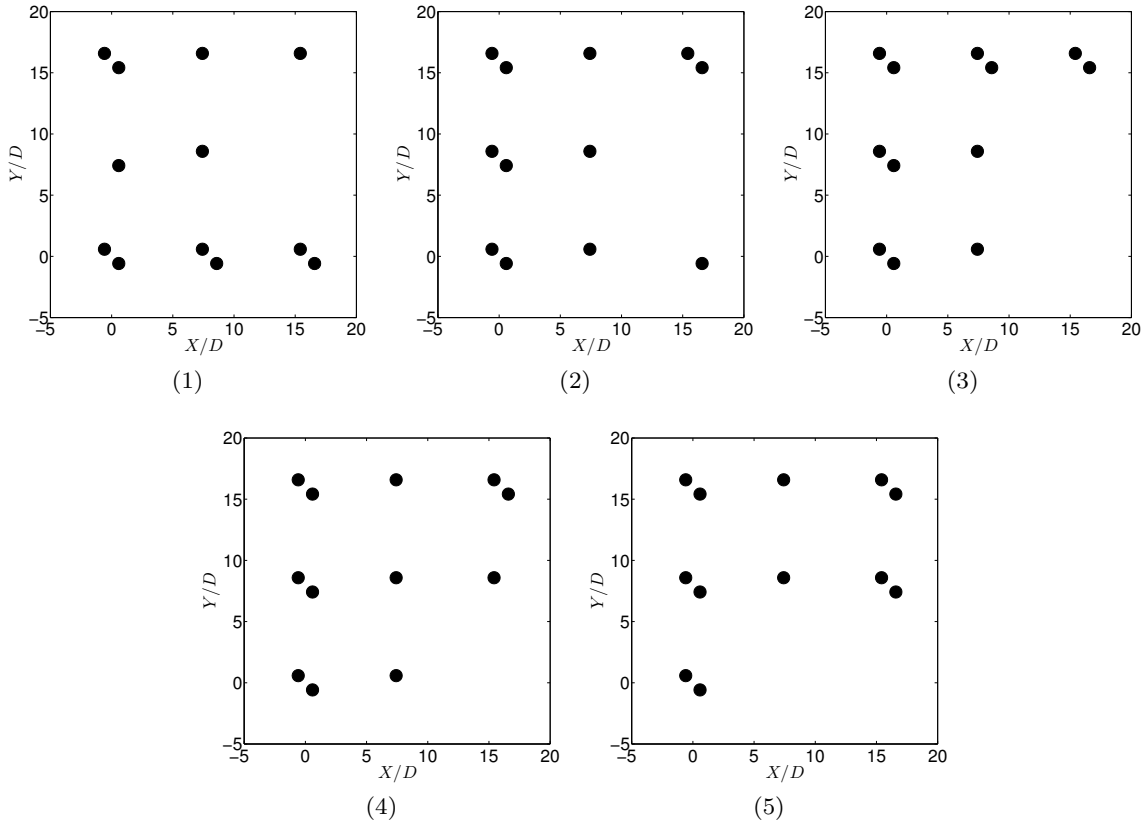

Figure 2.5: Five 12-turbine array configurations selected for analysis of relative array performance. The power data for each configuration is a subset of the data collected from the full 18-turbine array when only 12 turbines are producing power with wind speeds between 6-10 ms^{-1} and wind direction between $215^\circ - 235^\circ$. Only turbines that are operational are indicated by the solid black circles. Configuration (1) includes 43 ten-minute average data points, configuration (2) includes 15 data points, configuration (3) includes 31 data points, configuration (4) includes 47 data points, and configuration (5) includes 12 data points.

the array had a different C_p for each of the different configurations. This was attributable to differences in wind conditions during the measurement of each configuration, rather than to an inherent difference in efficiency for each configuration. To account for this, the C_p of each turbine in each array was normalized by the average C_p of the front two turbines in that array. The relative performance of the arrays, i.e., the average of the normalized C_p for each configuration, was compared using a paired t-test.

2.3.4 LRB Model Calibration

The centerline meteorological tower data for a single VAWT and a VAWT pair were both used to determine the sink spacing, s_s, for the LRB model. For the single VAWT (c.f. Figure 2.3 (a)), only the measurement locations at $A_{CL}/D = -2,\ 2$, and 8 were used to give velocity measurements around the first turbine in the array. Velocity measurements at $A_{CL}/D = -15$ were taken only for the VAWT pair but were also used with the single VAWT data. For the VAWT pair (c.f. Figure 2.3 (b)), all of the measurement locations were used in the calibration, i.e., $A_{CL}/D = -15,\ -1.5,\ 2$, and 8. The calibration consisted of finding the sink spacing that minimized, in the least-squares sense, the difference in the model prediction of the velocity and the field data at the specified positions.

As shown in Figures 2.6 (a) and 2.6 (b), the best-fit curves to the respective data sets achieve reasonable agreement between the LRB model and the field measurement. However, rather than use two different values for s_s (i.e., one from the single VAWT calibration and one from the VAWT pair), an intermediate value of $s_s/D = 1.44$ is used subsequently for all of the LRB model predictions. This value was obtained by minimizing the sum of the least-squares error between the field data and the respective LRB model predictions. The sensitivity of the LRB model to the choice of s_s is quantified in section 2.4.3. It is worth noting that the point directly behind the single turbine, i.e., $A_{CL}/D = 2$, sits very close to a singularity, i.e., the potential sink, which makes an LRB prediction of velocity at this point very sensitive to small changes in the flow field.

The calibrated LRB model was used to reconstruct the remainder of the centerline meteorological tower velocity data for the four-turbine array as shown in Figure 2.7. There

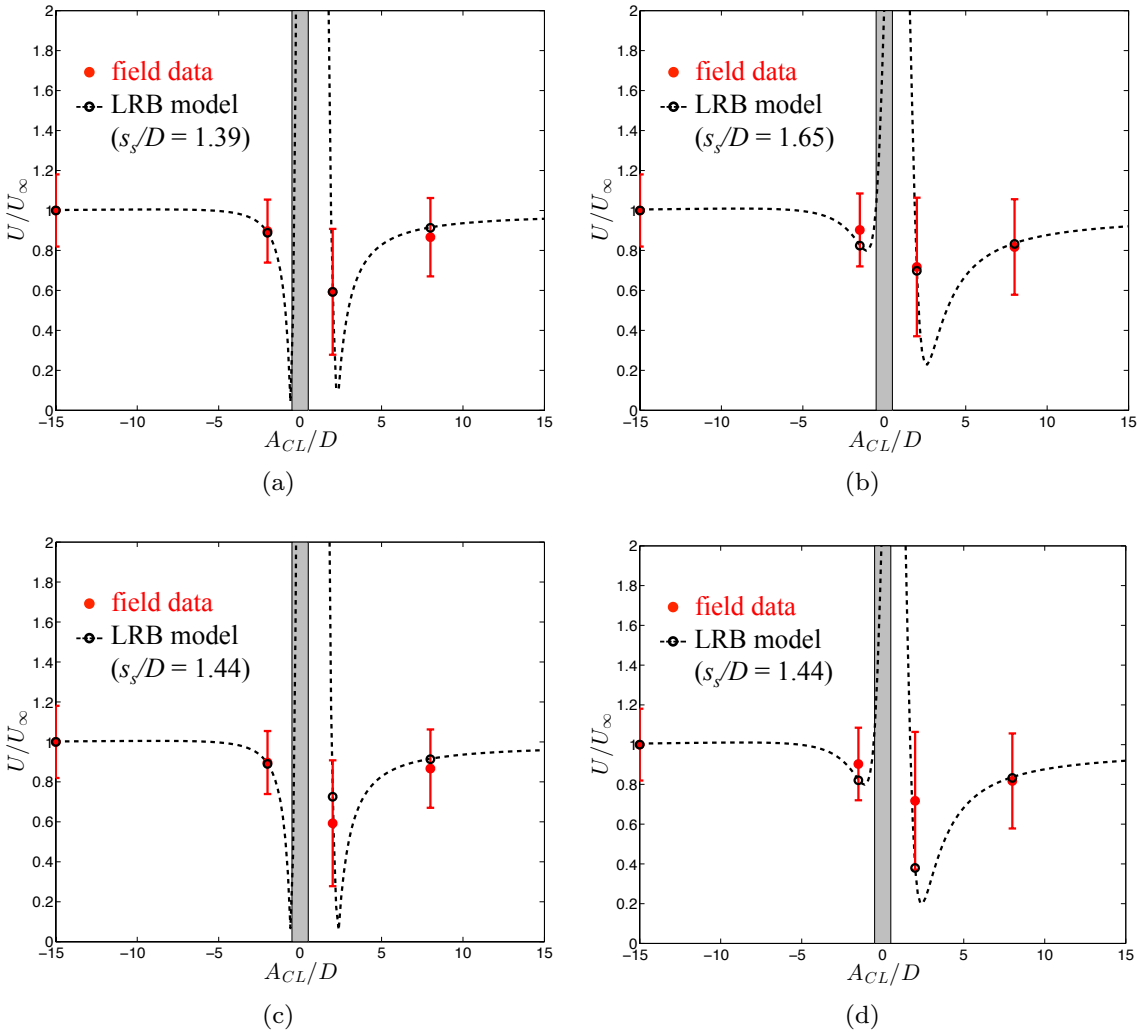

Figure 2.6: Calibration of the sink spacing model parameter, s_s. (a) Least-squares fit to the field data for the single VAWT. (b) Least-squares fit to the field data for the VAWT pair. Best fit model parameter, $s_s/D = 1.44$, to the combined field data for the (c) single VAWT and (d) pair of VAWTs. Open black circles indicate the LRB model prediction of flow speed at the field measurement locations. Gray rectangles indicate turbine positions.

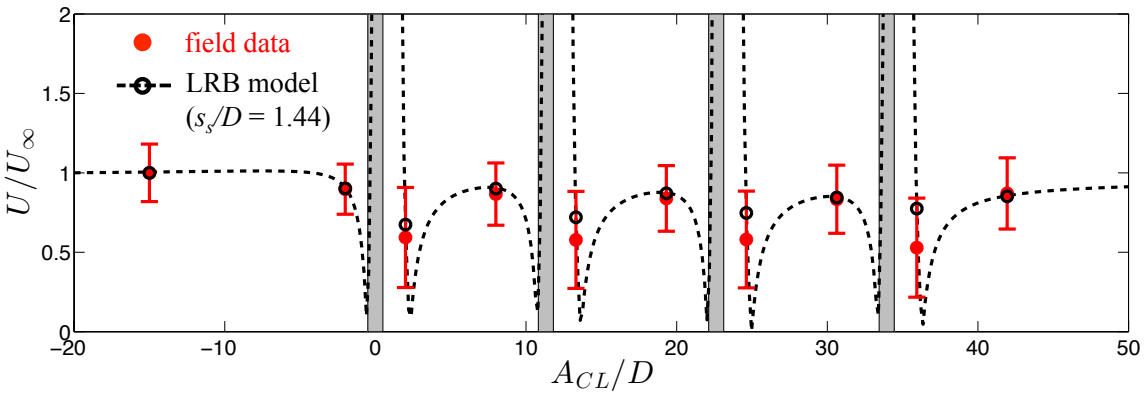

Figure 2.7: Comparison of the LRB model with meteorological tower streamwise velocity measurements for the four-turbine array. Open black circles indicate the LRB model prediction of flow speed at the field measurement locations. Gray rectangles indicate turbine positions.

is reasonable agreement between the model and the field data beyond the original four calibration points. Notably, the best agreement with the LRB model is seen directly in front of the each turbine, which is most important for predicting turbine performance. The worst agreement is directly behind each turbine due to the aforementioned model sensitivity near the singularities.

2.4 Results

2.4.1 LRB model prediction of individual turbine performance

Figure 2.8 shows the effect of wind direction variation on turbine performance for the four-turbine array. Figure 2.8 (a) indicates the bins for wind direction that were used to sort the field data. The variation of the individual turbine C_p with wind direction is shown in Figure 2.8 (b). The LRB model prediction of individual turbine performance is shown in Figure 2.8 (c).

For each data point in Figure 2.8 (b), the mean C_p for a given turbine and wind direction has been normalized as follows: the mean C_p of each turbine was first normalized by its mean C_p when the wind was near perpendicular to the array (i.e., $285°-310°$). An exception is for turbine 18, which had erroneous velocity data when the wind velocity was between $285° - 310°$. Hence, the C_p for turbine 18 was normalized by the average C_p when the wind

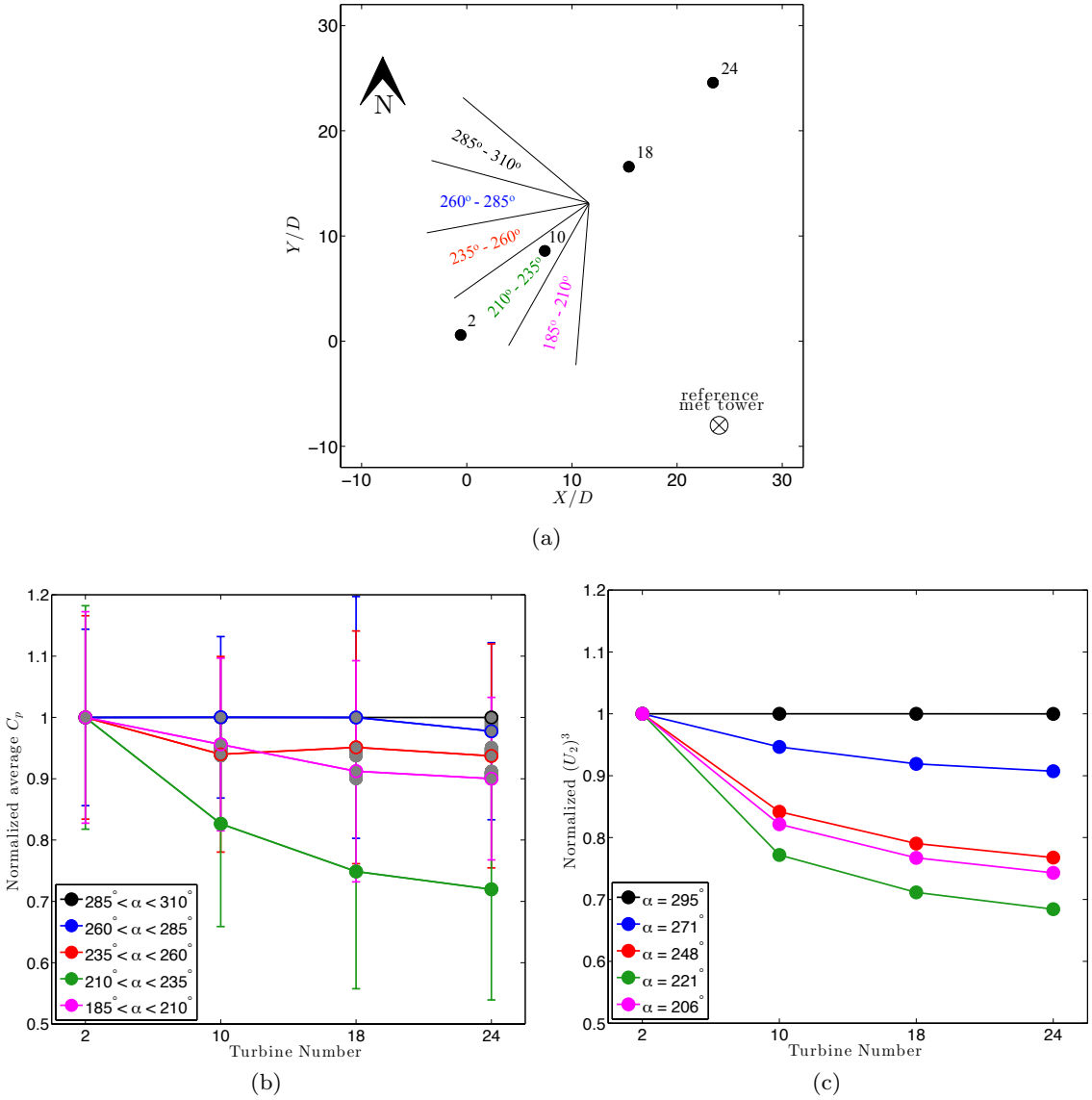

Figure 2.8: The effect of wind direction on turbine performance for the indicated four-turbine array. (a) Schematic of the array with the bins of wind direction. (b) Field measurements of individual turbine performance. Error bars indicate one standard deviation. (c) LRB model prediction of turbine performance for each wind direction, taken as the average in each bin.

direction was between $260^\circ - 285^\circ$. The normalized C_p was then divided by the C_p of the lead turbine (i.e., turbine 2) to give the relative trend among the turbines.

The result of each $t-$test between pairs of data points in Figure 2.8 (b) is shown graphically using closed symbols to denote mean values that are statistically significantly different when compared to any other data point, and open symbols to denote mean values that are not statistically significantly different between points that coincide within the gray region. For example, for turbine 10, the blue data point is directly on top of the black data point, and is indicated by an open blue symbol filled with gray. This blue point is greater than the red, pink, and green data point; similarly, the solid green data point is lower than all of the rest. However, the difference between the red and pink data points is not statistically significant, as indicated by open symbols connected by a gray bar.

The LRB model results shown in Figure 2.8 (c) are normalized in an analogous manner as the field data. There is reasonable agreement between the field measurements and the LRB model, which is able to capture the qualitative trends in individual turbine performance and also correctly predicts the ordering of the colored curves. The best turbine performance occurs when the wind is nearly perpendicular to the array (black curve) and the worst turbine performance occurs when the wind is nearly parallel to the array (green curve), as would be expected intuitively. What is less intuitive is the slope of these curves, i.e., the percent change in performance of one turbine downstream of another. It can be seen that there is good agreement again between the LRB model and the field data for the limiting case of incident wind nearly parallel to the array. However, the LRB model tends to over-predict the effect of the wake as the wind direction moves around toward perpendicular to the array. The field data indicates that when the wind direction is greater than approximately 270°, there is no loss in performance due to the wake of the upstream turbines. However, for a wind direction of 271° (i.e., the mean of the $260^\circ - 285^\circ$ bin), the LRB model predicts a monotonic decrease in performance for each turbine, ending with a loss of power of about 10% at turbine 24 relative to turbine 2. Similarly, the LRB model amplifies the magnitude of the power lost among the downstream turbines for the intermediate wind directions, which indicates that the modeled LRB wake is broader than the actual VAWT wake. This

overprediction of power loss suggests that the LRB model, while effective in capturing the rank ordering of turbine performance, is a conservative estimate of array performance.

Figure 2.9 shows a comparison between the field data and the LRB model for the eighteen-turbine array configuration when all turbines are simultaneously operational. The

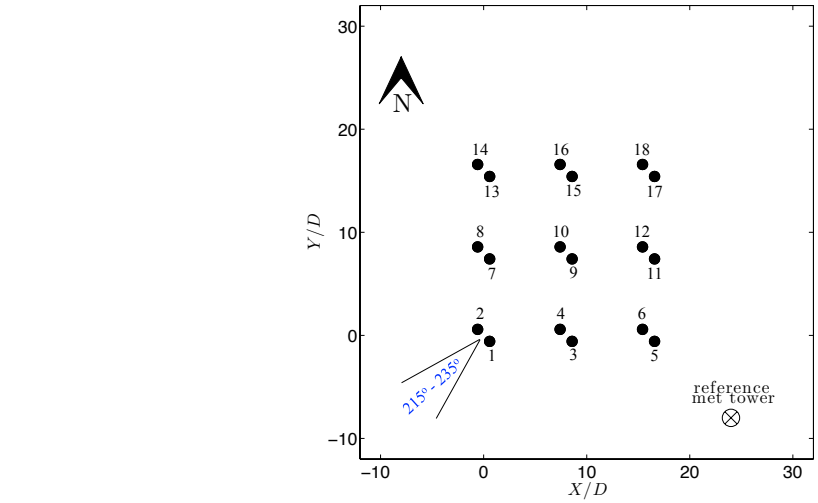

(a)

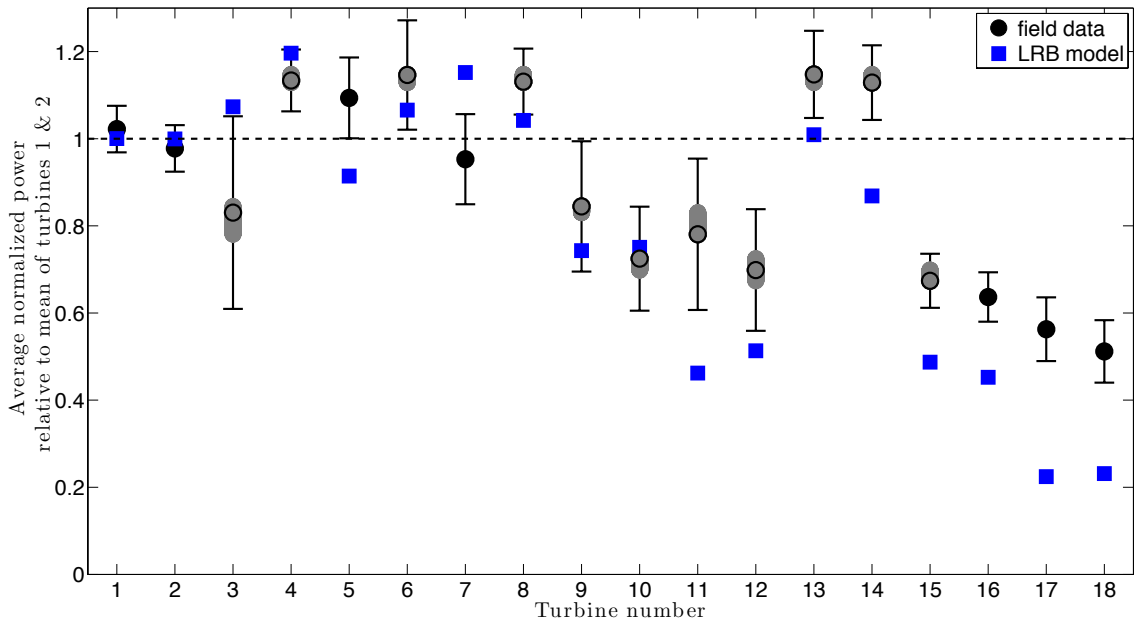

(b)

Figure 2.9: (a) Schematic of the eighteen-turbine array with the bin of wind direction. (b) Comparison of field measurements and LRB model prediction for the performance of individual turbines within the array. Error bars indicate one standard deviation.

average wind direction of 222° is used for the LRB model prediction. The mean C_p for a

given turbine is normalized by the average C_p of the front two turbines, i.e., turbines 1 and 2. Qualitatively, there is good agreement between the plots of the field data and that of the LRB model. During the measurement campaign, turbines 3 and 7 experienced a number of maintenance issues. This is reflected in the large variance in turbine 3 and the relatively low performance of both turbines.

While it is possible that other discrepancies between the two plots in Figure 2.9 are due to individual variations among the turbines, we are not able to quantify these effects because the individual performance characteristics of each turbine in isolation are unknown. However, if we assume that each turbine in the array is identical, as they ideally should be, then the qualitative agreement with the LRB model gives some insight into the characteristics of the flow within the array. One interesting feature is that both the field data and the LRB model indicate that there are specific turbines within the array that perform better than the front two turbines. Specifically, the LRB model predicts that turbines 3, 4, 6, 7, 8, and 13 all perform better than the front two turbines to some degree. Similarly, the field data shows that turbines 4, 5, 6, 8, 13, and 14 consistently perform better than the front two turbines. This seems to suggest that a position such as that of turbine 4, which is slightly set back within the array, has an inherent aerodynamic advantage over, e.g., turbines 1, 2, or 3. The physical mechanism that promotes such an advantage is addressed in the next section. Also of interest is that the LRB model seems to under predict the performance of turbines 5 and 14, which are on the outer corners of the array. This discrepancy is attributed to the overly broad nature of the LRB wake as observed in the previous section.

2.4.2 LRB model prediction of turbine array performance

While it is desirable to accurately predict the percent change in power loss for individual turbines within an array, a primary goal of the proposed low-order model is to be able to predict differences in average performance between unique array configurations. As discussed in the experimental methods section, a subset of five unique turbine configurations from the eighteen-turbine array was examined for this purpose. Figure 2.10 shows a comparison

between the field measurements and the LRB model prediction of array performance for the five unique turbine configurations.

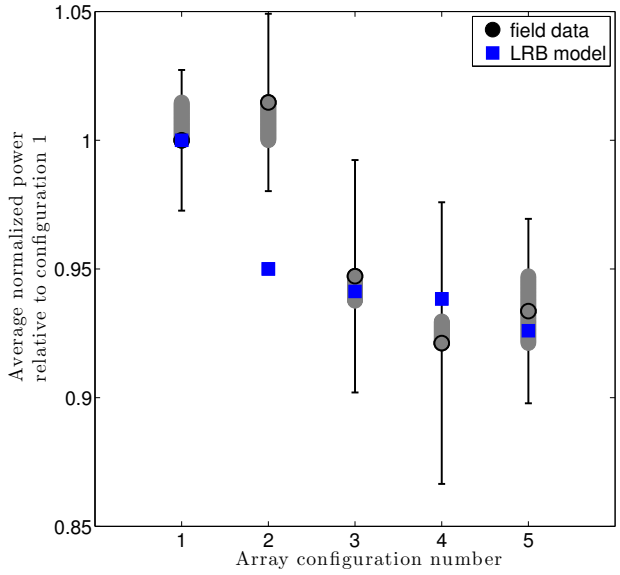

Figure 2.10: Comparison of field measurements and LRB model prediction of average array performance for the five unique configurations of twelve VAWTs. Error bars indicate one standard deviation.

The most significant result is that the LRB model correctly predicts the ranking of all of the array configurations to within statistical certainty. Specifically, the performance of both configurations 1 and 2 are found to be greater than 3, 4, and 5 with greater than 95% confidence that the null hypothesis can be rejected. There is a seemingly large discrepancy between the LRB model prediction and the field data for array configuration 2. One possible explanation for this is the aforementioned tendency for the model to overpredict the wake effect. Configuration 1 has nine turbines on the front edges of the array facing into the freestream whereas configuration 2 only has eight (c.f. Figure 2.5). Therefore, it is reasonable to expect that configuration 1 performs better than configuration 2, as the LRB model suggests. However, the limited sample size of each of the subset turbine configurations is such that the difference in performance between configuration 1 and 2 was not found to be statistically significant (as indicated by the vertical gray bars). While the difference in performance between configuration 3 and 5 and also 4 and 5 is not statistically significant, the

difference in performance between configuration 3 and 4 is significant. In each case where the measured difference in array performance is statistically significant, the LRB model prediction of array performance is in agreement with this result. It is noteworthy that the magnitude of the difference in performance among the arrays in this case is modest, not exceeding about 10%, and even less than 1% between the LRB model predictions. Yet the model is nonetheless effective in correctly identifying the relative array performances.

Using the LRB model, we can now identify the physical mechanisms that lead to enhanced array performance. A qualitative comparison between the streamlines of the best and worst array configuration is shown in Figures 2.11 (a) and 2.11 (b), respectively. An im-

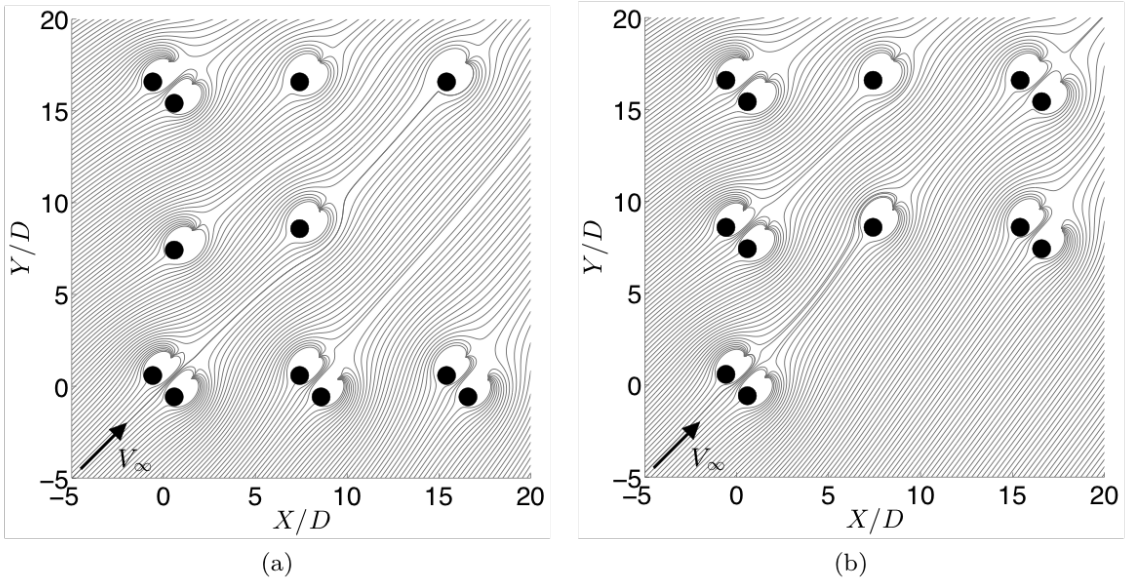

Figure 2.11: Streamlines generated by the LRB model for the (a) best and (b) worst performing arrays as predicted by the model, i.e., configuration 1 and 5, respectively.

mediate observation is that the best array configuration has the greatest number of turbines exposed to the freestream. However, this metric is insufficient to distinguish between all five configurations. For example, configurations 3 and 4 have the same number of turbines exposed to the freestream, yet configuration 3 exhibits better performance than configuration 4. For further investigation, smaller two- and three-turbine array configurations can be examined.

Figure 2.12 (a) shows a schematic of a two-turbine array configuration in which turbine

A is moved diagonally in front of turbine B. The total array performance, i.e., the average

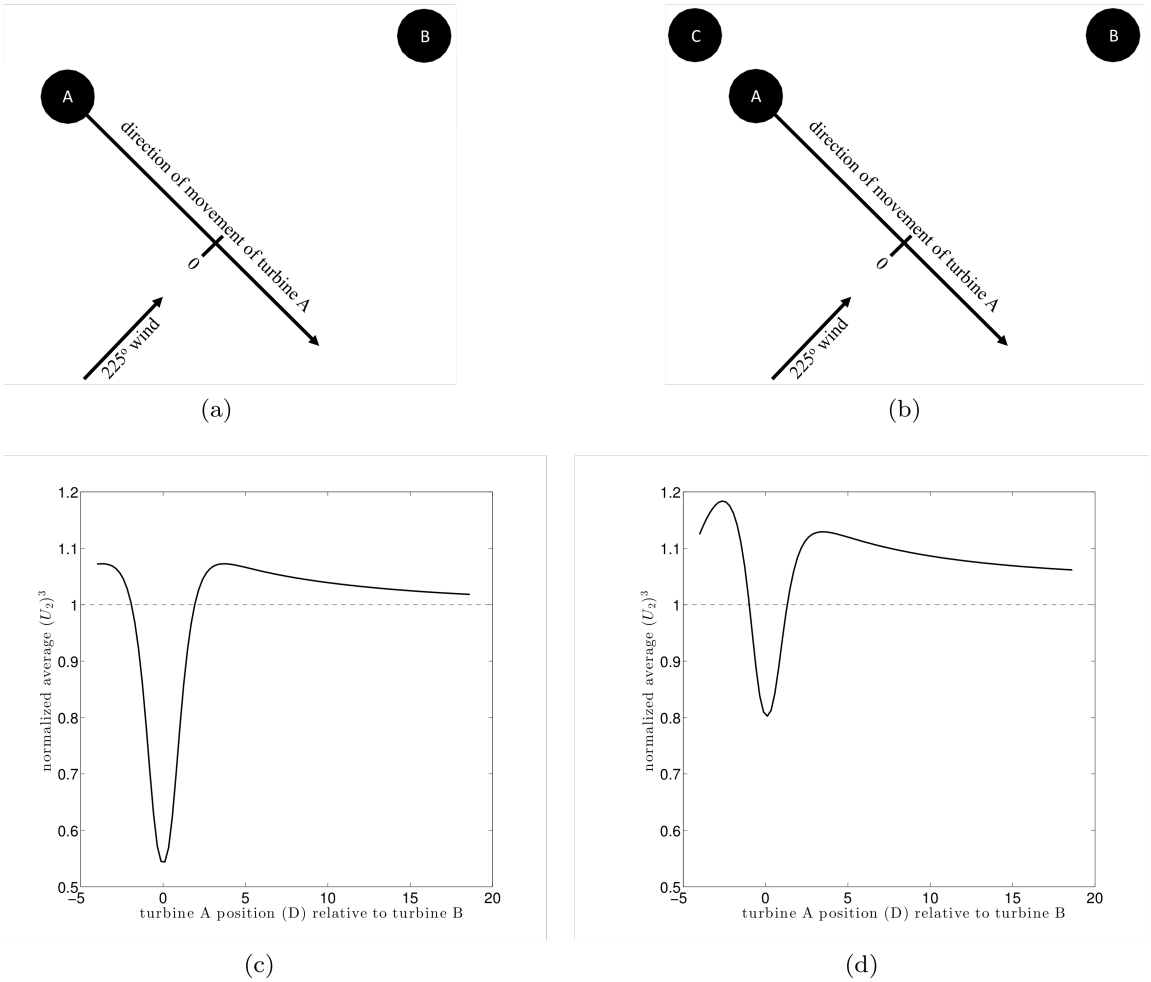

Figure 2.12: (a) Schematic for a two-turbine array and (b) three-turbine array, and the LRB model prediction of array performance for each, (c) and (d), respectively. Turbines are drawn to scale with the initial position of turbine A indicated in the figures.

of U_2^3 of the two turbines, as a function of the position of turbine A is shown in Figure 2.12 (c). The average value of U_2^3 has been normalized by the value for an isolated turbine. As expected, the curve is symmetric about the point where the two turbines are aligned with the freestream. There is also a region that is approximately 4 D wide where the wake of the upstream turbine negatively impacts array performance. Interestingly, the best orientation for the two turbines occurs when turbine B is just slightly outside of the wake region of turbine A, where there is an increase in performance of about 7% relative to the turbines in isolation. A similar result has been observed in previous field experiments (Dabiri, 2011).

Beyond this point, the normalized array performance asymptotically decreases toward 1 as the turbines are spread further apart.

Figure 2.12 (b) shows a similar schematic as in Figure 2.12 (a), but with an additional turbine that is fixed in place adjacent to turbine A. Again, turbine A is moved diagonally across the line indicated in the plot. The total array performance as a function of the position of turbine A is shown in Figure 2.12 (d). There is now an asymmetry to the array performance curve about the point where turbines A and B are aligned with the freestream due to the presence of the third turbine. The best array performance occurs when turbine A is in between turbines C and B. Furthermore, the entire curve has shifted upward relative to the two-turbine configuration due to the addition of turbine C. There is also a noticeable reduction in the difference between the best and worst configurations, as indicated by the shallower drop in array performance when turbine A is directly in front of turbine B. The LRB model suggests a competition within the array between turbine blockage that can locally accelerate the flow and wake losses that slow the flow down. Optimal array configurations will position turbines to exploit local flow acceleration and avoid regions of wake loss.

2.4.3 Robustness of LRB model prediction of array performance

The robustness of the LRB model depends on its sensitivity to the choices of C_p, r_u, r_w, and s_s. In the present evaluation, the LRB model is considered to remain effective if it accurately predicts the ranking of the array configurations in Figure 2.10. To test the model, the nominal turbine efficiency is varied from 5-59% (i.e., the Betz limit); r_u/D is varied from 1-6; and r_w/D is varied from 5-10. The results for these test cases are shown in Figures 2.13 (a) - (f). In these figures, the black circles indicate that the LRB model correctly predicts the array ranking and an "X" indicates that the model fails. The red circle indicates the nominal values of the LRB model. This test shows that the model prediction is robust to increases in the value used for C_p but that it fails when C_p is too low (5%) and for very large C_p (59%).

Two cases were considered to evaluate the effect of varying the sink spacing, one with

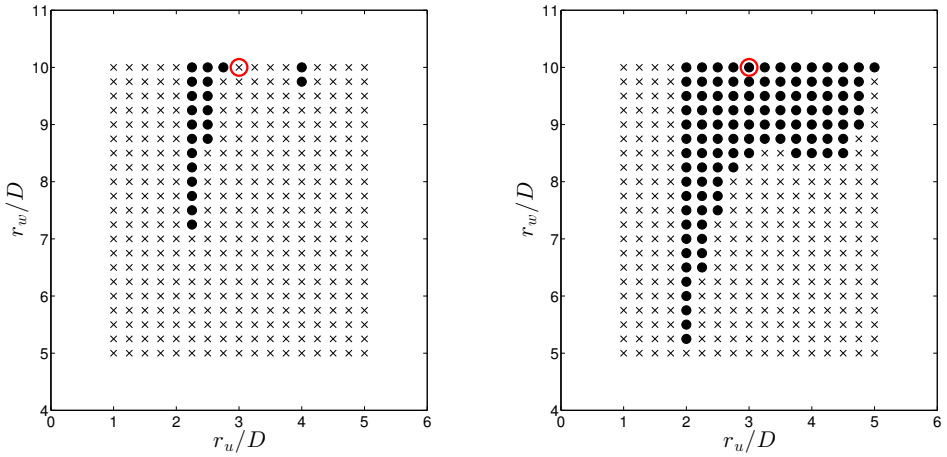

(a)

(b)

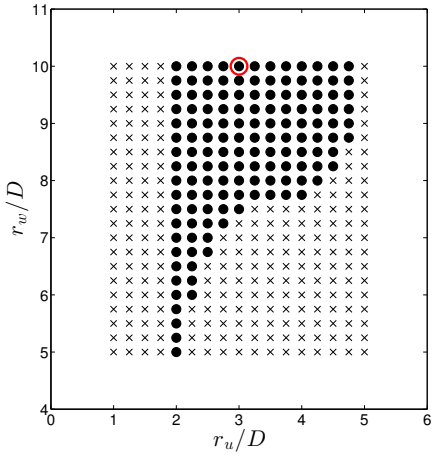

(c)

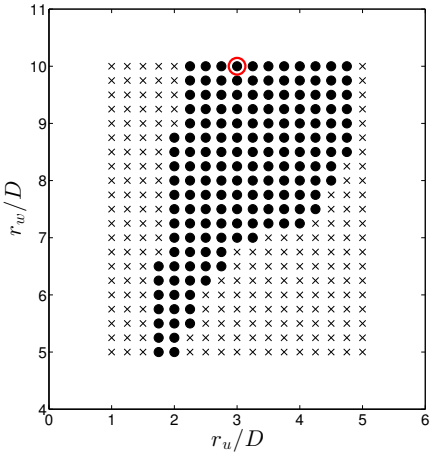

(d)

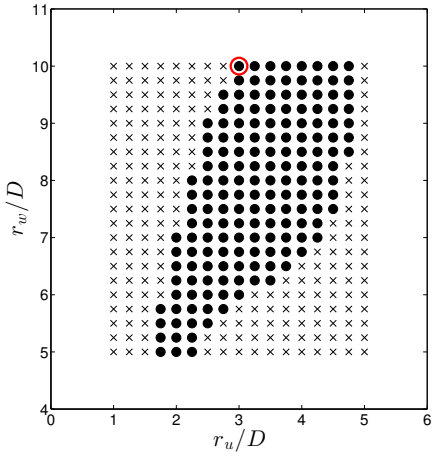

(e)

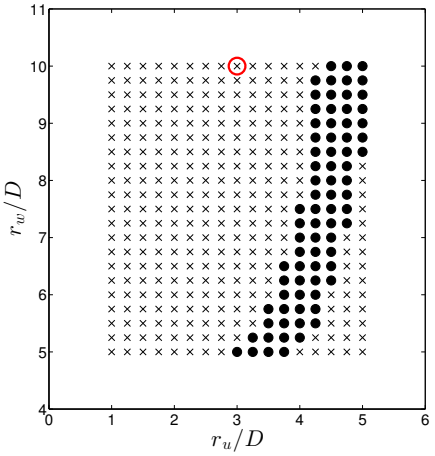

(f)

Figure 2.13: Parameter study of the LRB model prediction of array performance with varying C_p as (a) 5%, (b) 10%, (c) 15%, (d) 20%, (e) 30%, and (f) 59%. Black circles indicate the model correctly predicts the ordering of array performance and black X's indicate where the model fails. The red circle indicates the nominal model parameters of $r_u/D = 3$ and $r_w/D = 10$.

$s_s/D = 1.0$ and another for $s_s/D = 2.0$. Figures 2.14 (a) and 2.14 (b) show that the LRB model is relatively insensitive to these choices of the sink spacing parameter, which are considered extreme cases given the small difference in least-squares estimates of s_s during the model calibration.

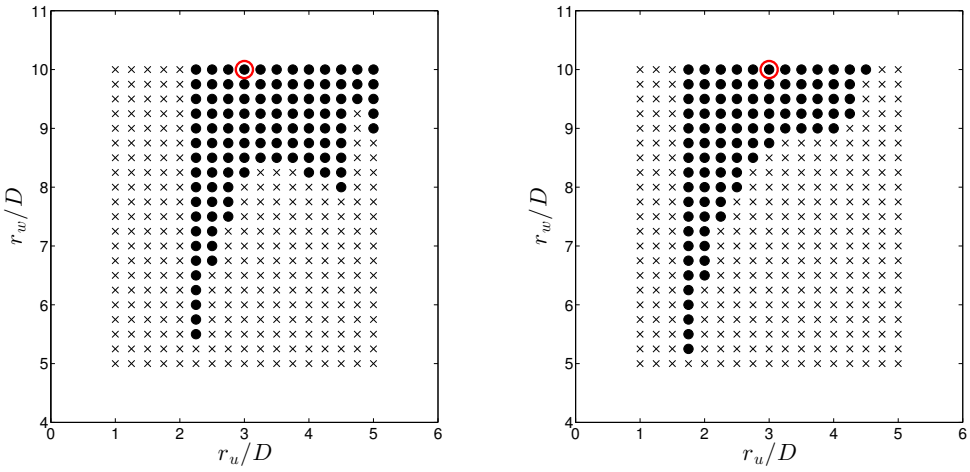

(a) (b)

Figure 2.14: Parameter study of the LRB model prediction of array performance with varying the sink spacing, s_s, model parameter. (a) $s_s/D = 1.0$, (b) $s_s/D = 2.0$. Black circles indicate the model correctly predicts the ordering of array performance and black X's indicate where the model fails. The red circle indicates the nominal model parameters of $r_u/D = 3$ and $r_w/D = 10$.

2.5 Conclusions

The low-order LRB model has been developed to rapidly distinguish the performance of arbitrary configurations of VAWT arrays. Comparison with field measurements validated that the LRB model is able to not only asses differences among individual turbines within an array but also to predict the ranking of the average performance of unique VAWT arrays with better than 95% statistical certainty. The LRB model is conservative in that it overpredicts the losses caused by the turbine wakes. In conjunction with the field data, the LRB model also provides insight into the physical mechanisms that determine individual turbine dynamics and array performance. A key conclusion that can be drawn from the present results is that there are two primary competing fluid dynamic mechanisms within

the array that contribute to the overall performance. The first is turbine blockage, which can locally accelerate the flow adjacent to a turbine and, perhaps surprisingly, can thereby increase the performance of neighboring turbines above their performance in isolation. The other effect is that of the turbine wake, which locally decelerates the flow and leads to a decrease in performance for downstream turbines. The combined effect is captured by the LRB model, and therefore it achieves a reasonable estimate of performance based on the average wind speed directly ahead of each turbine.

It is prudent to note that this simplified model is not intended to capture the complex structure and dynamics of the three-dimensional turbulent flow that occurs in wind farms, e.g., the vertical shear of the incoming atmospheric boundary layer, or the dynamics of the energy exchange between the atmospheric boundary layer and the array. Rather, the model is intended to serve as a tool that can rapidly assess, to a first approximation, the viability of one wind farm configuration relative to another. This approach is akin to the work of Betz, which, despite assumptions of inviscid flow among other simplifications, can be quite useful for performing engineering calculations of wind turbines. Additionally, the benefit of the current approach is that optimal array configurations can be found with significantly less computational expense than higher fidelity numerical simulations such as LES and much more rapidly than in experiments.

As follow up to this work, recent wind tunnel experiments have demonstrated that the LRB model is quite robust in its ability to predict the ranking of array configurations among VAWTs with completely different geometry than those of the original field experiments (I. Brownstein, personal communication). Further work has also been undertaken to use the model in an evolutionary algorithm seeking to find optimal array configurations, with support from additional field measurements (Dabiri & Brownstein, 2015). Still, the model is inherently limited in many respects, including in its inability to characterize the dynamics of the VAWT wake. For this, more detailed and controlled experiments are needed, which are laid out in the next two chapters.

Chapter 3

A comparison of measurements in motor-driven and flow-driven turbine experiments

The material presented in this chapter was authored by Araya & Dabiri (2015) and published in *Exp. Fluids* **56** : 7. Its purpose is to introduce the laboratory-scale VAWT experiments by an account of determining the appropriate use of a motorized turbine, a necessary constraint on some of the subsequent experiments presented in Chapter 4. Some minor revisions have been made to the published text, references, and formatting of figures in accordance with the rest of this thesis.

3.1 Introduction

When studying flow phenomena in a scaled laboratory experiment or in a computational simulation, it is often not possible to achieve dynamic similarity with the full-scale flow of interest. In the case of wind and water turbine experiments, a scaled model turbine may not perform as well as in the field, or perhaps not at all, due to a mismatch of Reynolds number and other scaling difficulties such as increased bearing friction. Grant & Parkin (2000) note that in very small-scale model turbine experiments the blades may operate below their design Reynolds number, causing extensive flow separation, which can limit the extrapolation of these model tests to full scale rotors. Despite this, both wind and water tunnel experiments are used as a practical means to study the flow characteristics of turbines even when dynamic similarity cannot be achieved.

Recent progress has been made in understanding the aerodynamics of VAWTs, also known as cross-flow turbines. Bachant & Wosnik (2014) examined the effect of Reynolds number on the near-wake characteristics of VAWTs. They found that turbine performance becomes nearly independent of Reynolds number at turbine diameter Reynolds number of $Re_D = 8 \times 10^5$. They also observed that near-wake statistics, such as mean velocity and turbulence intensity, showed only slight differences across the full range of Reynolds number that was examined, i.e., $Re_D = 3 - 13 \times 10^5$. Fujisawa & Shibuya (2001) as well as Ferreira *et al.* (2009) investigated the dynamic stall characteristics of VAWTs using an isolated turbine blade. To mimic the VAWT dynamics, they used a motor to rotate the blade about a central axis within a freestream flow and observed the successive generation and shedding of vortices from the blade as it was rotated. Both studies concluded that the development of these vortices changed as the tip speed ratio, λ, the ratio of blade speed to freestream flow speed, was increased, but neither made reference as to whether such observations were physical with respect to a functional VAWT whose rotation is only driven by the oncoming flow.

This practice of prescribing the motion of turbine blades within a flow is common among both experimental and numerical turbine investigations. A survey of previous literature is tabulated in appendix B, with a distinction made between studies that used 'flow-driven' and 'motor-driven' turbines, details of which are provided in Section 3.2. The compilation highlights the frequent use of the motor-driven technique and also inconsistencies in reporting power or torque measurements, which is shown in the current work to be an important aspect of matching the wake characteristics of flow-driven turbines.

Intuitively, one might anticipate that a motor-driven turbine whose geometry, shaft torque, and λ matches that of a flow-driven turbine would also share the same performance and wake characteristics. However, this conjecture has not been experimentally tested. A computational study by Le *et al.* (2014) compared the performance of a flow-driven turbine subject to a given load with that of one where λ was specified. Their results show reasonable agreement in the measured power coefficient of the two configurations, which is consistent with the aforementioned hypothesis. Still, it remains unclear how the prescribed motion af-

fects the resulting flow field measurements, e.g., the wake velocity profile and power spectra. To address this, two-dimensional particle image velocimetry is used to measure the velocity in the near wake region of a 3-bladed VAWT. From this, the average velocity is examined as well as the velocity power spectra, wake circulation, and measurements of shaft torque among various flow-driven and motor-driven configurations.

3.2 Description of experimental test cases

3.2.1 Flow-driven turbine

Under normal operating conditions, the rotation of a turbine rotor about its central axis is driven by the oncoming flow. In practice, this means that the turbine rotation rate is fixed by the torque due to aerodynamic forces as well as any additional applied load, such as bearing friction, an electrical generator, or, often in experiments, an unpowered DC motor used to model a generator (see, e.g., Kang & Meneveau, 2010). In a numerical simulation, this additionally implies that the fully coupled fluid-structure interaction (FSI) is modeled for the turbine. Of the literature surveyed, relatively few researchers (see, e.g., Bazilevs *et al.*, 2011; Hsu & Bazilevs, 2012; Le *et al.*, 2014) included the turbine FSI in their numerical simulations.

A schematic of the aerodynamic forces acting on a VAWT airfoil is shown in Figure 3.1. In the absence of any externally applied load, the turbine is free to spin to an average rate dependent solely on the balance of torque due to lift and drag of the blades. This is referred to henceforth as the 'free-spin' operating condition of the turbine and is shown schematically in Figure 3.2. Note that this condition is the theoretical upper bound on the average rotation rate for a given turbine geometry and flow Reynolds number. The addition of friction into the system or power extraction via an electrical generator serves to apply a torque in the direction opposing the torque due to lift, as indicated in Figure 3.3, which slows the turbine to a new, lower equilibrium rotation rate.

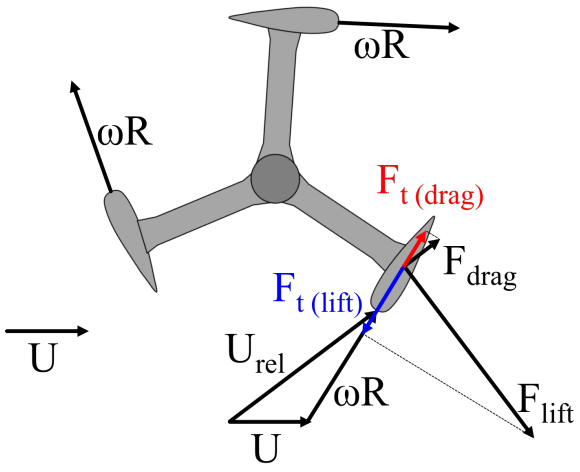

Figure 3.1: Vector diagram of the aerodynamic forces acting on a VAWT airfoil. Here U is the freestream velocity, ω is the angular velocity of the turbine, R is the turbine radius, U_{rel} is the relative freestream velocity as seen by the turbine blade, and $F_{t(lift)}$ and $F_{t(drag)}$ are the tangential components of the lift and drag forces, i.e., F_{lift} and F_{drag}, respectively.

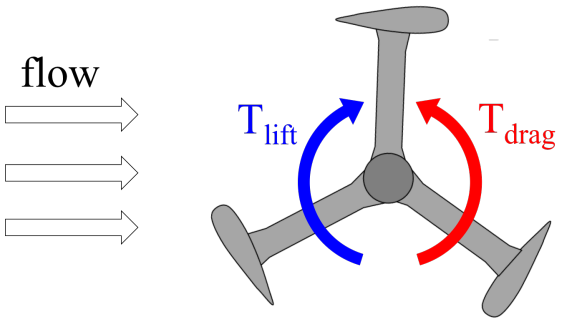

Figure 3.2: Free-body diagram (top view) of a flow-driven VAWT for the free-spin operating condition. Here the net torque due to lift, T_{lift}, balances with the net torque due to drag, T_{drag}.

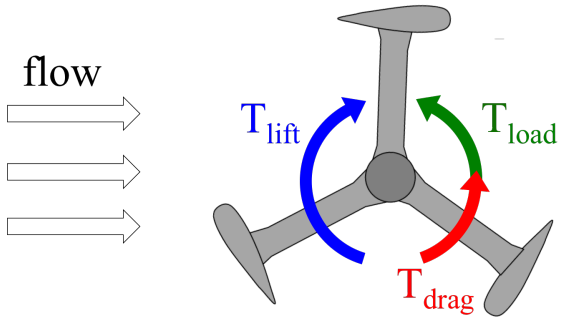

Figure 3.3: Free-body diagram (top view) of a flow-driven VAWT operating with an applied load. Here the net torque due to lift, T_{lift}, of the blades exceeds the torque due to drag, T_{drag}, and is balanced by the torque added by an applied load, T_{load}.

3.2.2 Motor-driven turbine

A scaled turbine often cannot produce sufficient torque to reach the tip speed ratio observed at full-scale. This could be the result of excessive friction in the system, reduced aerodynamic performance at the Reynolds number of the scaled turbine, or perhaps because an isolated blade is being investigated. Regardless, it often leads to the use of a motor to actively drive the motion of the turbine blade(s). A similar practice is common in numerical turbine simulations where the blade kinematics are specified but the dynamic fluid-structure interaction is neglected to reduce computational costs. By using a motor in an experiment, additional forces are applied to the turbine system. In particular, the motor itself has a finite amount of internal resistance that results in a torque in the same direction as the aerodynamic drag on the turbine blades. Thus, in order to rotate the turbine shaft, power must first be supplied to the motor to overcome its own resistance and further power must be supplied to accelerate the turbine shaft. It is important to emphasize, however, that the lift and drag produced by the oncoming flow past the blades is always present, regardless of the motor. Therefore, it is the sum of all of these forces that determines the kinematics of the turbine, as illustrated in Figure 3.4.

During steady operation, the motor can control the turbine rotation within three distinct operational regimes: (a) a lift-dominated regime, wherein the net torque due to aerodynamic lift on the blades exceeds the net torque due to drag and the motor effectively acts as a

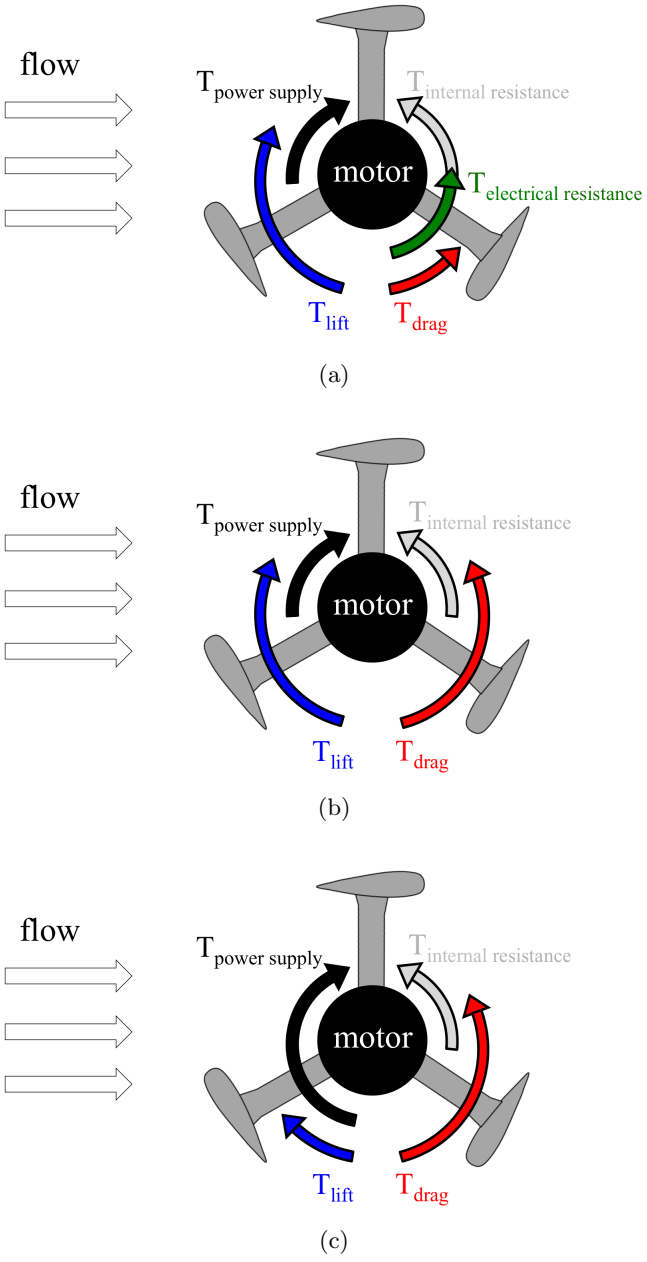

Figure 3.4: Free-body diagram of the motor-driven turbine when operating in (a) the lift-dominated regime, (b) the neutral regime, and (c) the drag-dominated regime. The components of torque that contribute to the overall shaft torque are shown in each regime with colored arrows. Note that only torques due to the motor and aerodynamics are considered, i.e., friction is neglected.

generator to mimic power extraction in a flow-driven case, (b) a neutral regime, wherein the net torque due to aerodynamic lift of the blades is balanced by the torque due to drag (i.e., the free-spin condition), and the motor only acts to overcome its own internal resistance, and (c) a drag-dominated regime, wherein the net torque due to aerodynamic drag of the blades exceeds the torque due to lift and the motor acts to accelerate the turbine to a rotation rate that it could not achieve under flow-driven conditions alone. These three regimes are shown schematically in Figures 3.4(a), 3.4(b), and 3.4(c), respectively. In what follows, the near wake characteristics of a 3-bladed VAWT are evaluated across all three regimes and compared with flow-driven cases when possible.

3.3 Experimental Setup

3.3.1 Model turbine

A three-bladed model turbine was 3D printed for the experiment using a polycarbonate-like material (3D Systems Accura® 60 Plastic). The printed model was sanded and bead blasted to 320-grit, giving a smooth surface finish. Figure 3.5 shows a CAD drawing of the turbine along with relevant dimensions. Each of the three turbine blades consisted of a NACA 0018

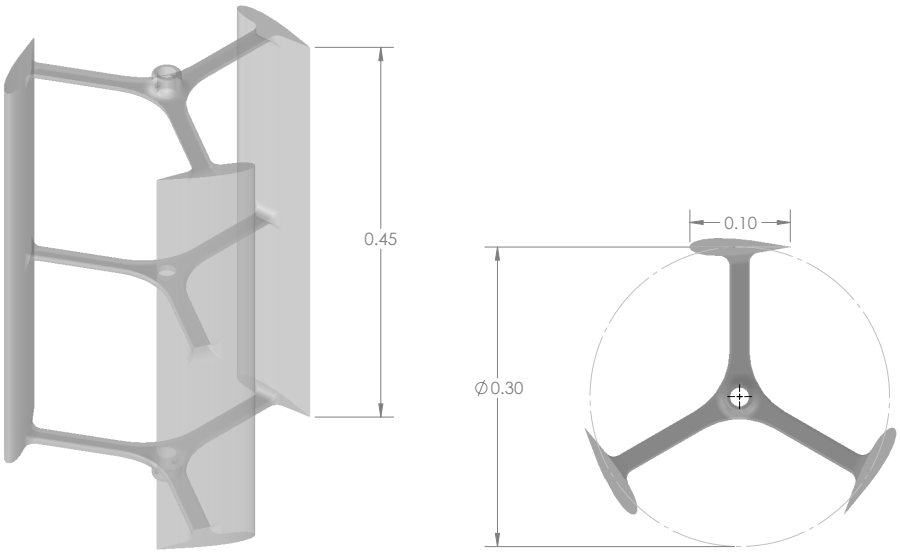

Figure 3.5: CAD drawing of the 3-bladed model turbine used in the experiment. (a) Isometric view and (b) top view. All dimensions are given in meters.

airfoil with a 0.1 m chord and extruded to a length of 0.45 m. The turbine diameter was 0.3 m, as measured by a circle tangent to the chord of each airfoil. The turbine blockage ratio, based on its frontal projected area, varied between 8-16% over one revolution.

3.3.2 Water channel facility

Experiments were conducted in a 40 m long, 1.1 m wide, and 0.6 m deep, free-surface, recirculating water channel facility capable of flow speeds up to approximately 26 cms^{-1}. The bottom end of the turbine central shaft was attached to a flange mount with Type 316 stainless steel ball bearings. This flange was mounted to a stainless steel plate that anchored the turbine to the floor of the water channel. The top end of the turbine shaft was connected to a rotary torque sensor with digital encoder (Futek TRS705). The torque sensor had a 0-20 N-m measurement range with a maximum system error of +0.020% rated output (i.e., +0.004 N-m) in clockwise torque and -0.025% rated output (i.e., -0.005 N-m) in counterclockwise torque. An optically clear, cast acrylic sheet, approximately 1.8 m in length and spanning the width of the channel, was suspended to be flush with the free surface in order to eliminate surface distortion. A cross-section view of the model turbine mounted in the water channel is shown in Figure 3.6.

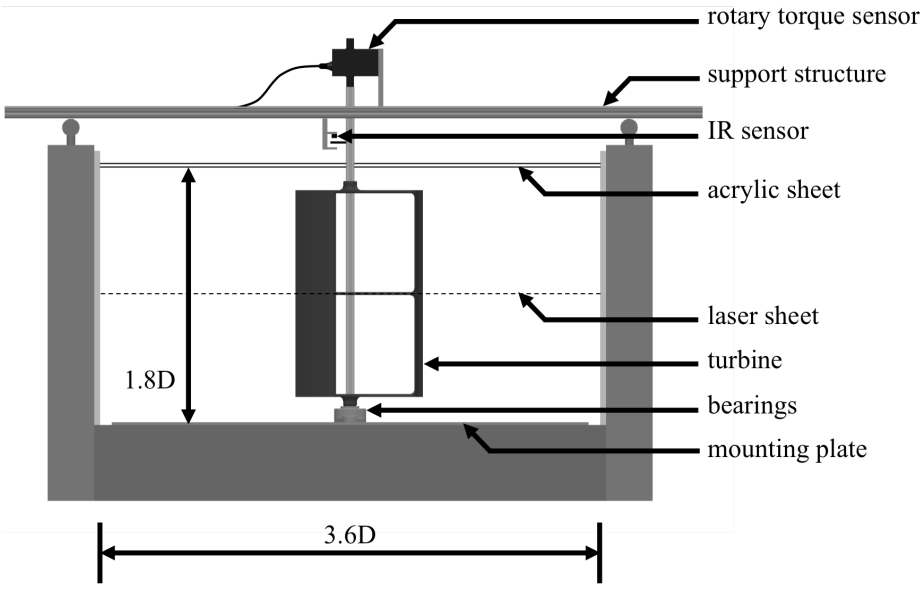

Figure 3.6: Section view schematic of the experimental setup.

3.3.3 Diagnostics

The wake was surveyed using two-dimensional particle image velocimetry (2D PIV), which is justified provided that the out of plane particle motion is minimized. This was achieved in the current setup by aligning the measurement plane with the symmetry plane of the model, parallel to the freestream, and by sampling images at a sufficiently fast frame rate. The flow was seeded with 100 μm silver-coated hollow ceramic spheres (Potters Industries LLC). To illuminate the particles, a collimated laser sheet was created in a plane parallel to the mid-height of the turbine using a continuous, 1W, 532 nm DPSS laser system (Laserglow Technologies) along with a single plano-concave cylindrical lens with a -3.9 mm focal length (Thorlabs) mounted directly in front of the laser. A custom-built infrared (IR) sensor was used to detect the starting orientation of the turbine for each data set. The voltage signal from this IR sensor as well as from the torque sensor and encoder were input into a National Instruments data acquisition (NIDAQ) device (USB-6221), which was controlled by LabView software (National Instruments). Using the TTL signal from the encoder, the NIDAQ device triggered a high-speed camera (Photron APX-RS), mounted above the channel, to capture two images of the turbine wake every 5° of shaft rotation. The camera has a resolution of 1024 $\times$ 1024 pixels, which, for the field of view of the experiment, corresponded to a scaling factor of 6.81 pixels/cm. Each pair of images was taken at either 125 or 60 Hz, depending on the flow speed. Images were captured over a total of 59 turbine revolutions per case. This resulted in a total of 4248 image pairs per case that were later processed using DaVis imaging software (LaVision) for obtaining 2D PIV measurements.

Figure 4.2 shows a top-view schematic of the PIV field of view relative to the mounting location of the turbine. The image plane was calibrated using a wire mesh with equally-spaced 2.54 cm squares. A multi-pass PIV algorithm was used with a decreasing interrogation window size and 50% window overlap. Two passes were made with 32 $\times$ 32-pixel interrogation windows, followed by another two passes made with 16 $\times$ 16-pixel windows, the latter of which corresponded to vector spacing of 1.2 cm. A median filter with universal outlier detection was used to remove spurious vectors, which were subsequently replaced by interpolation.

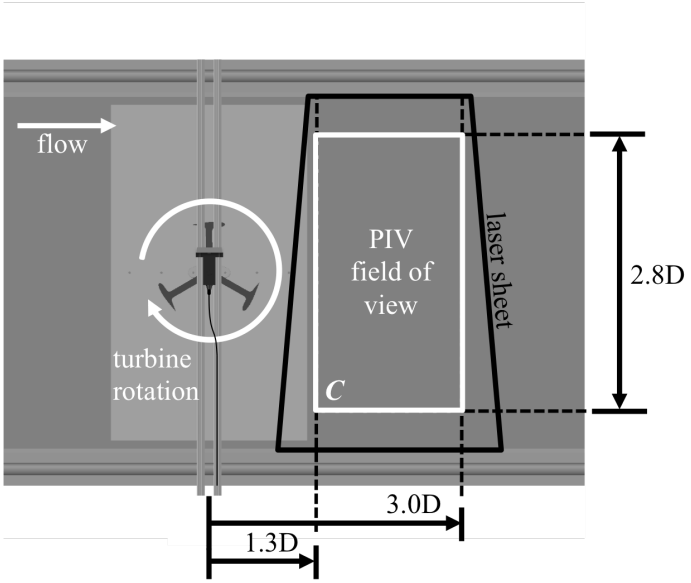

Figure 3.7: Top view schematic of the experimental setup. The contour, C, encloses the area that was used to calculate spatial averages of velocity as well as circulation. Dashed vertical lines indicate the relative position of C to the turbine center.

To measure the nominal speed of the flow at the measurement location, PIV measurements were taken as described above, but with the turbine removed. The resulting streamwise velocity field was averaged in time as well as in the spanwise and streamwise directions to give a single point measurement of the freestream flow speed. Measurements of six different flow speeds, each at a different pump speed, resulted in a linear regression with an R^2 value of 0.9993, as indicated in Figure 3.8(a). The derived linear equation from these measurements was used to calculate all of the subsequent freestream speeds. A sample of the freestream streamwise velocity profile is shown in Figure 3.8(b) corresponding to a pump speed of 15.5Hz. Boundary layers are observed to form near the walls of the channel. Their effect is partially negated by considering only velocity measurements away from the wall, i.e., within the contour, C (c.f. Figure 4.2). In addition, since these wall effects (as well as turbine blockage) are always present, their effect is negligible when comparing similar flow-driven and motor-driven cases.

As a check for consistency, the flow speed was actively monitored during each test using a current velocity meter (Swoffer model 2100) placed upstream of the turbine. This flowmeter has a measurement range of 0.03-7.5 m/s and was calibrated using a moving cart system

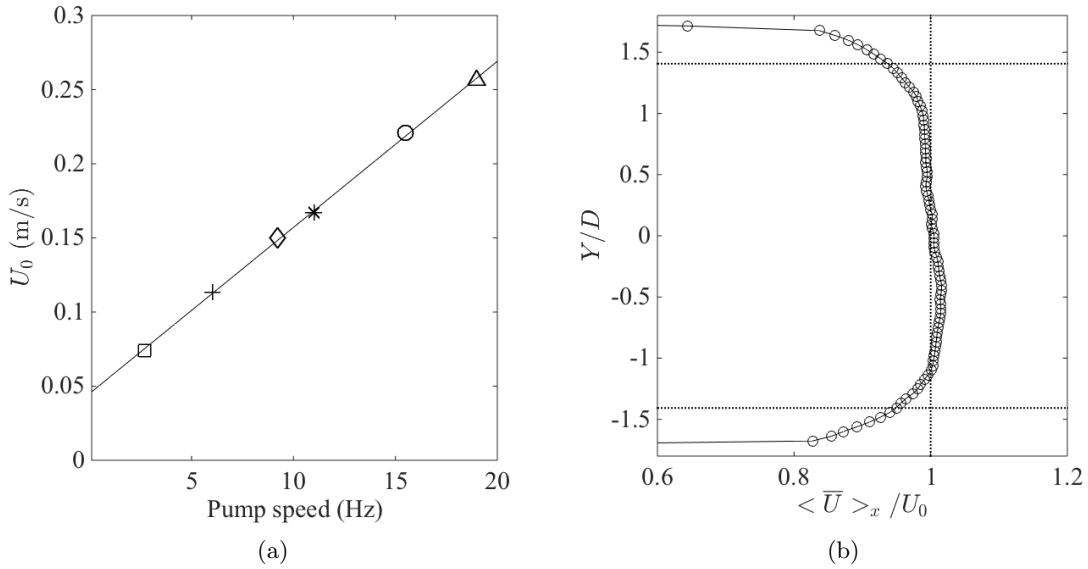

Figure 3.8: (a) Measured freestream flow speeds, U_0, for different pump speed settings (symbols). The solid line is a linear fit to the points. (b) A sample of the measured streamwise velocity (symbols) for a pump setting of 15.5Hz. The velocity has been averaged both in time and in the streamwise direction, indicated as $< \overline{U} >_x$. The spanwise coordinate, Y, is normalized by the turbine diameter, D. Dashed lines are for reference only. The upper and lower dashed lines indicate the bounds of the contour, C (c.f. Figure 4.2).

equipped with a laser distance sensor (see details in, e.g., Whittlesey & Dabiri, 2013).

In flow-driven cases, the end shaft of the torque sensor was either freely spinning or slowed by a brake, as indicated in Figure 3.9(a). Braking was achieved using a mechanical vise to adjust the amount of friction applied to the shaft and thus the average λ of the turbine. In motor-driven cases, the end shaft of the torque sensor was connected to a DC motor (Pittman GM14904S013-R1), as indicated in Figure 3.9(b), and was controlled by a constant voltage power supply (Mastech HY3005F-3) capable of providing 0-30V at 0-5A. The static load of the motor, i.e., the torque due to its internal resistance, was such that at any flow speed the turbine could not rotate unless power was supplied to the motor.

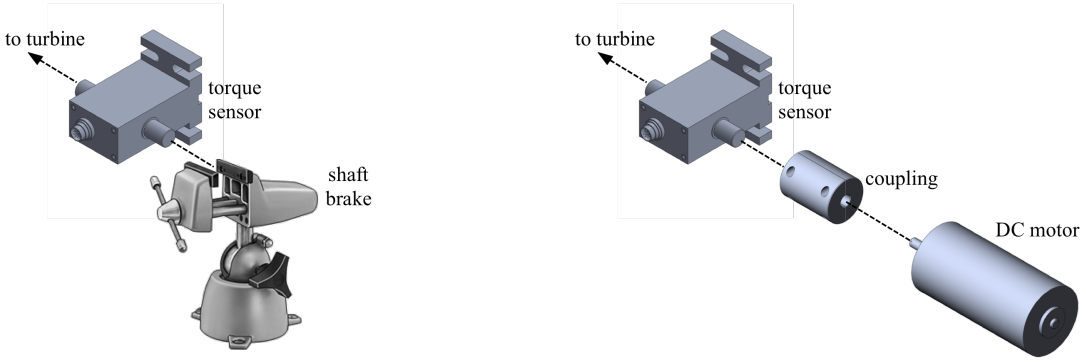

(a) (b)

Figure 3.9: Schematic of the setup used for controlling the turbine λ in (a) flow-driven and (b) motor-driven cases.

3.4 Experimental procedure

3.4.1 Turbine neutral curve

With the motor disconnected from the turbine and no additional load applied, the turbine performance was evaluated for the entire range of flow speeds of the facility. In each case, a LabView program tracked the number of turbine revolutions to compute the average λ, as well as voltage measurements from the IR sensor, encoder, camera trigger, and torque sensor. All voltage measurements were sampled at 2500 Hz and recorded over a total of 59 turbine revolutions in each case. The average λ over four trials for each flow speed is shown in Figure 3.10 versus the turbine diameter Reynolds number, Re_D. Also shown in the figure is a shaded region that bounds one standard deviation in the measurement of λ, as estimated by standard error propagation analysis. This figure is referred to throughout as the 'neutral curve' and it represents an upper bound on λ for flow-driven cases. Since the turbine system has inherent losses (e.g., due to imperfect bearings) this empirical curve is shifted lower than would be theoretically possible in the presence of only airfoil lift and drag forces. Nevertheless, it is a useful reference to distinguish between motor-driven cases that operate at a λ above and below the limits of the curve, as is done in this study and detailed in the next section.

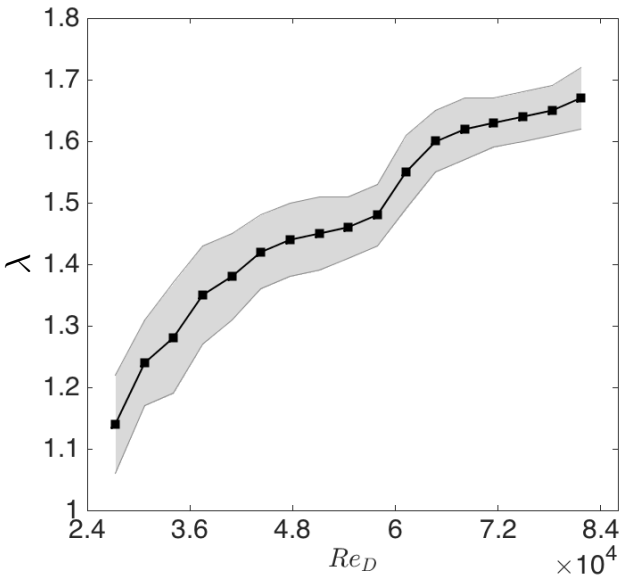

Figure 3.10: Measured values (symbols) of the turbine neutral curve. The shaded region bounds one standard deviation in the measurement of λ. The neutral curve indicates the maximum λ that the turbine could reach for a given Re_D without an external load applied to its shaft.

3.4.2 PIV measurement conditions

Figures 3.11 and 3.12 indicate the nominal turbine operating conditions below and above the neutral curve, respectively. These were the conditions that were targeted for conducting PIV measurements of the wake. The actual turbine operating conditions, measured during the PIV measurements, are indicated in Figures 3.13 and 3.14; data in these figures is summarized in Tables 3.1 and 3.2, respectively. Below the neutral curve (c.f. Figure 3.11), the selected turbine operating conditions included varying λ for a fixed Re_D (red, blue, and black points), as well as varying Re_D for a fixed λ (green and yellow points). Above the neutral curve (c.f. Figure 3.12), PIV measurements were conducted for a fixed Re_D with varying λ (red, blue, and black points), as well as two cases at a lower Re_D (green and yellow points). Of the latter two cases, the green point, which is motor-driven, was selected to match the λ of the higher Re_D, flow-driven case (red point).

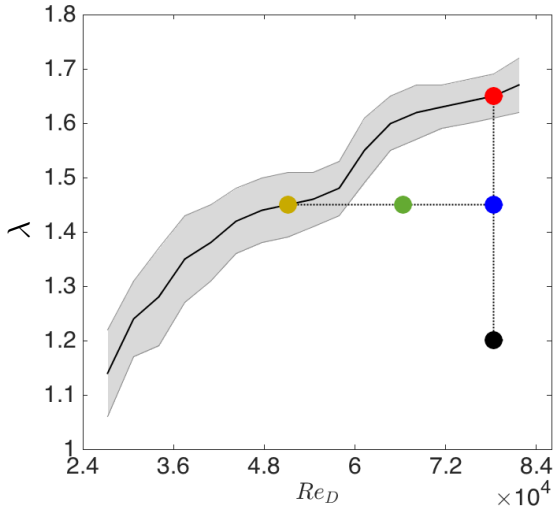

Figure 3.11: Nominal turbine operating conditions (symbols) on or below the neutral curve (solid black line) selected for PIV measurements. The yellow symbol corresponds to $Re_D = 5.1 \times 10^4$, λ=1.45; the green to $Re_D = 6.6 \times 10^4$, λ=1.45; the red, blue, and black to $Re_D = 7.8 \times 10^4$ and λ=1.65, 1.45, and 1.20, respectively. The dotted lines are for visual reference only. The shaded region bounds one standard deviation in measured λ along the neutral curve.

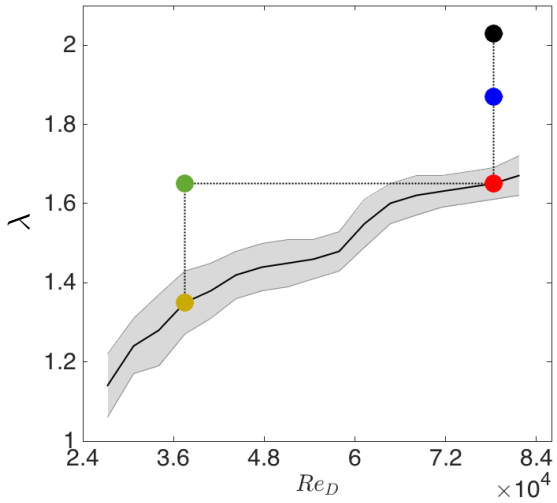

Figure 3.12: Nominal turbine operating conditions (symbols) on or above the neutral curve (solid black line) selected for PIV measurements. The yellow symbol corresponds to $Re_D = 3.7 \times 10^4$, λ=1.35; the green to $Re_D = 3.7 \times 10^4$, λ=1.65; the red, blue, and black to $Re_D = 7.8 \times 10^4$ and λ=1.65, 1.87, and 2.03, respectively. The dotted lines are for visual reference only. The shaded region bounds one standard deviation in measured λ along the neutral curve.

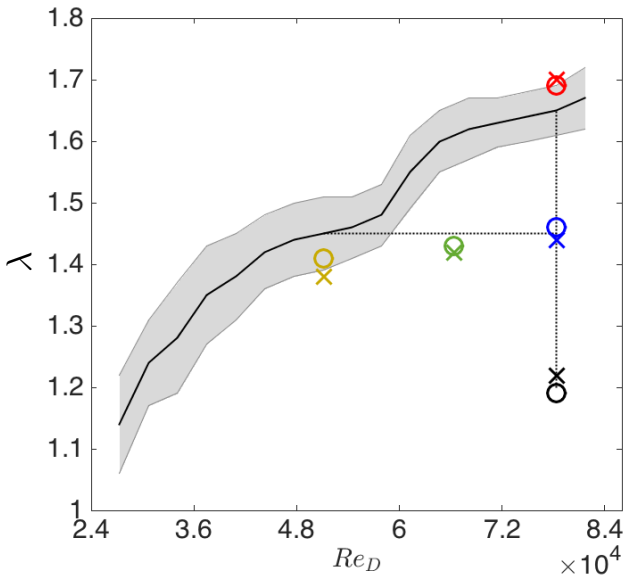

Figure 3.13: Measured turbine operating conditions (symbols) on or below the neutral curve (solid black line) during PIV measurements. Symbols correspond to either flow-driven ('O') or motor-driven ('X') cases. Values for each symbol are given in Table 3.1. Dotted lines are for visual reference only and correspond to the nominal conditions (c.f. Figure 3.11). The shaded region bounds one standard deviation in measured λ along the neutral curve.

Table 3.1: Measured turbine operating conditions on or below the neutral curve during PIV measurements. Symbols correspond to Figure 3.13; linetypes correspond to Figures 3.17, 3.18, 3.21, and 3.22. The 'driver' of the turbine rotation is indicated as either 'flow' for flow-driven or 'motor' for motor-driven.

Color	Symbol	Line	Driver	Re_D	λ
yellow	O	solid	flow	5.1×10^4	1.41
yellow	X	dashed	motor	5.1×10^4	1.38
green	O	solid	flow	6.6×10^4	1.43
green	X	dashed	motor	6.6×10^4	1.42
red	O	solid	flow	7.8×10^4	1.69
red	X	dashed	motor	7.8×10^4	1.70
blue	O	solid	flow	7.8×10^4	1.46
blue	X	dashed	motor	7.8×10^4	1.44
black	O	solid	flow	7.8×10^4	1.19
black	X	dashed	motor	7.8×10^4	1.22

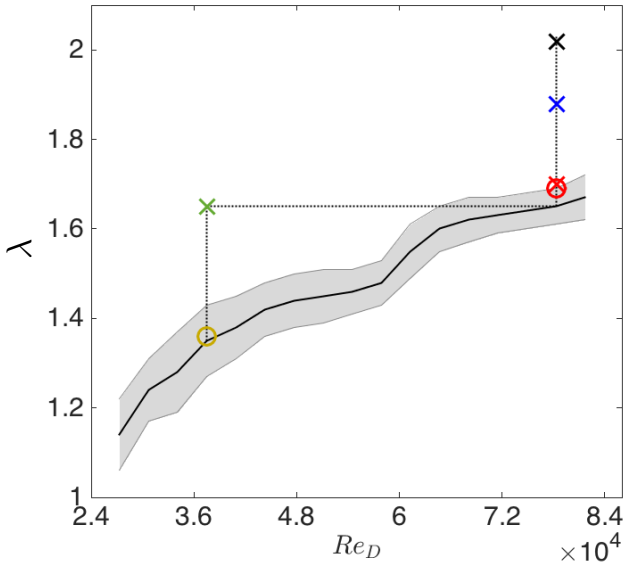

Figure 3.14: Measured turbine operating conditions (symbols) on or above the neutral curve (solid black line) during PIV measurements. Symbols correspond to either flow-driven ('O') or motor-driven ('X') cases. Values for each symbol are given in Table 3.2. Dotted lines are for visual reference only and correspond to the nominal conditions (c.f. Figure 3.12). The shaded region bounds one standard deviation in measured λ along the neutral curve.

Table 3.2: Measured turbine operating conditions on or above the neutral curve during PIV measurements. Symbols correspond to Figure 3.14; linetypes correspond to Figures 3.23 and 3.24. The 'driver' of the turbine rotation is indicated as either 'flow' for flow-driven or 'motor' for motor-driven.

Color	Symbol	Line	Driver	Re_D	λ
red	O	solid	flow	7.8×10^4	1.69
red	X	dashed	motor	7.8×10^4	1.70
blue	X	dashed	motor	7.8×10^4	1.88
black	X	dashed	motor	7.8×10^4	2.02
yellow	O	solid	flow	3.7×10^4	1.36
green	X	dashed	motor	3.7×10^4	1.65

3.4.3 Calculation of wake statistics

The PIV measurements of the wake were used to examine both its steady and dynamic characteristics. To examine the steady-state behavior, spatio-temporal averages of the streamwise component of velocity, U, were examined. For each case, U was first averaged in time over the entire measurement period. A sample of the temporally averaged streamwise ve-

locity, $\overline{U}$, is shown in Figure 3.15. This temporal average was then spatially averaged in the spanwise (y) and streamwise (x) directions, denoted as $< \overline{U} >_y$ and $< \overline{U} >_x$, respectively, over the entire measurement domain bounded by the contour, C.

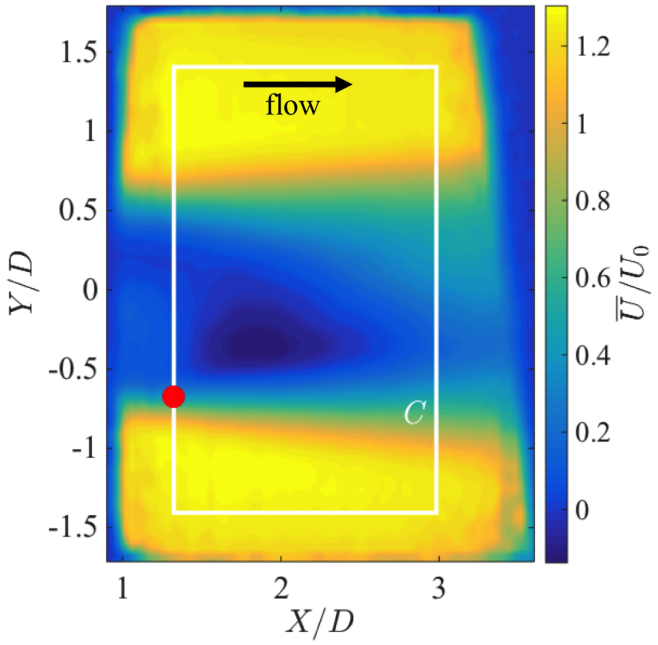

Figure 3.15: Contour plot of the temporally averaged streamwise component of velocity, $\overline{U}$, corresponding to $Re_D = 7.8 \times 10^4$ and $\lambda = 1.69$. The velocity is normalized by the freestream velocity, U_0, and X and Y are measured relative to the turbine center. The rectangular contour, C, encloses the area used to calculate spatial averages of velocity as well as circulation. At 1.3 D downstream of the turbine center, the red circle corresponds to the Y/D location where the rms of the transverse velocity fluctuations, v', was a maximum.

Wake dynamics were evaluated by computing the power spectra for the spanwise fluctuating velocity component, v', using the standard method of Welch (1967). The spectra for the flow-driven cases were computed at a single point 1.3 turbine diameters (D) downstream of the turbine center and along the span where the rms of the velocity fluctuations was a maximum. This was typically near the edge of the wake, as indicated by the red circle in Figure 3.15, where periodic blade vortex shedding would occur. The spectrum for a given motor-driven case was computed at the same point in the flow as in the corresponding flow-driven case. Since the turbine rotation rate fluctuated due to the unsteady hydrodynamic torque, the PIV data was not equally distributed in time, which is a necessary condition for

spectral analysis. To account for this, the single point velocity measurement was interpolated into an equally-spaced vector in time before computing the spectra. Specifically, the time stamps for the 4248 velocity fields were determined using the camera trigger signal, which had a known sample rate of 2500 Hz. Each TTL pulse to the camera corresponded to one velocity field time stamp. This temporal data was used to perform a spline interpolation of the measured velocity fields to obtain 4500 interpolated velocity fields that were uniformly-spaced in time and were used for computing the spectra. Figure 3.16 shows a sample of the measured (black line) and interpolated (red line) velocity data that corresponds to the point in the flow indicated by the red circle in Figure 3.15. It is worth noting

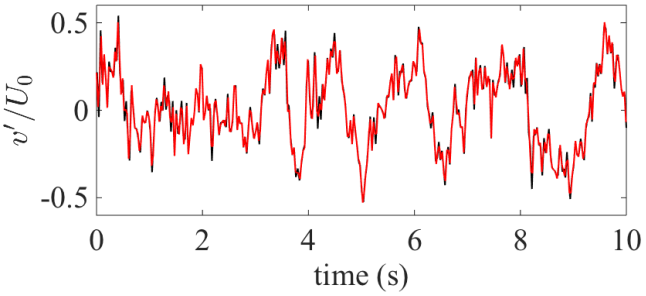

Figure 3.16: Sample of the measured spanwise fluctuating velocity component, v', normalized by the freestream velocity, U_0. The velocity sample corresponds to the point in the flow indicated by the red circle in Figure 3.15. The black line indicates the velocity as measured from PIV and the red line is the interpolated velocity used to compute the spectra.

that the computed spectra from this velocity data are limited by both the sample size and Nyquist frequency (i.e., half of the sample rate), which were both taken into consideration when plotting the spectra.

The circulation, Γ, in the wake of the turbine was evaluated by numerically integrating the vorticity within a rectangular area bounded by the contour, C (c.f. Figure 3.15). By definition,

$$\Gamma \equiv \iint_A \overline{\omega} \cdot d\mathbf{A}, \tag{3.1}$$

where $\overline{\omega}$ is the vorticity derived from the temporally averaged velocity and d$\mathbf{A}$ is a differential area element.

3.4.4 PIV error analysis

Confidence bounds on the PIV measurements were estimated using a statistical technique called dependent circular block bootstrapping. Details of the method are given by Theunissen *et al.* (2008). To summarize, at each point in the flow, the 4500 velocity samples were divided into overlapping blocks, where the block length for a given case was specified by the degree of autocorrelation among the samples. The blocks were then randomly sampled with replacement to construct a new series of 4500 velocities, called the bootstrap series. It is with this bootstrap series that any desired statistic, e.g., the mean, can be calculated. Repeating this a number of times gives an estimate of the confidence bounds for a given statistic. For normally distributed data, the bootstrap estimate of a given statistic tends to converge toward its 'true' value by increasing the number of bootstrap series used to calculate this statistic. Note that this error estimate does not account for any systematic error in the experimental method itself, but is sufficient for a comparative analysis, as in the case of this study. For the current PIV data set, a total of 5000 bootstrap series were created for each point in the flow. From these, the temporal mean and standard deviation were calculated and then averaged in space corresponding to either the spanwise or streamwise averages of velocity. For all cases examined, the bootstrap estimate of error in each calculated spatio-temporal average of the measured velocity was approximately 2% of the freestream velocity with 95% confidence.

3.5 Results

3.5.1 PIV measurements on or below the neutral curve

The spatio-temporal average velocity measurements corresponding to the operating conditions given in Table 3.1 are shown in Figures 3.17 and 3.18, where solid lines indicate flow-driven conditions and dashed lines indicate motor-driven conditions. Representative error bars are only drawn at the beginning and end of each curve in the figures so as not to obscure the data. In all instances, there appears to be close agreement among the flow-driven and motor-driven cases. There also appears to be a strong dependence of the wake

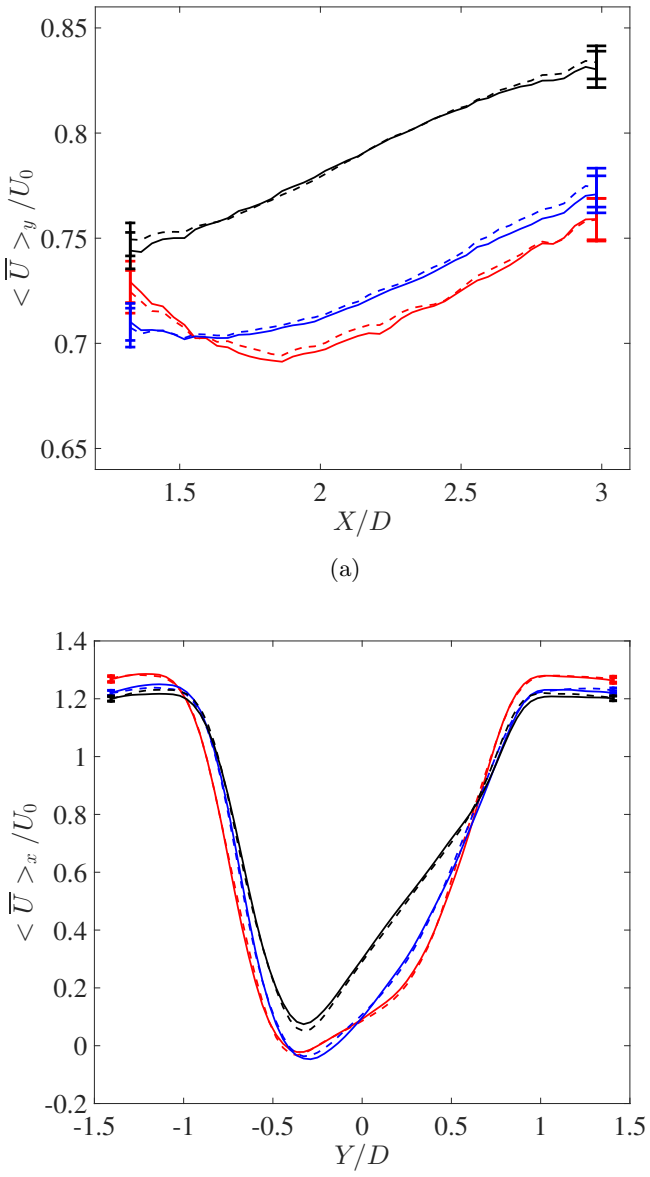

Figure 3.17: Spatio-temporal average velocity in the (a) spanwise and (b) streamwise direction when Re_D is fixed and λ is varied. Solid lines indicate flow-driven conditions and dashed lines indicate motor-driven conditions. Colors correspond to the nominal operating conditions on or below the neutral curve, i.e., $Re_D = 7.8 \times 10^4$ and λ=1.65 (red), 1.45 (blue), and 1.20 (black). The measured conditions for each line are given in Table 3.1. Error bars indicate one standard deviation.

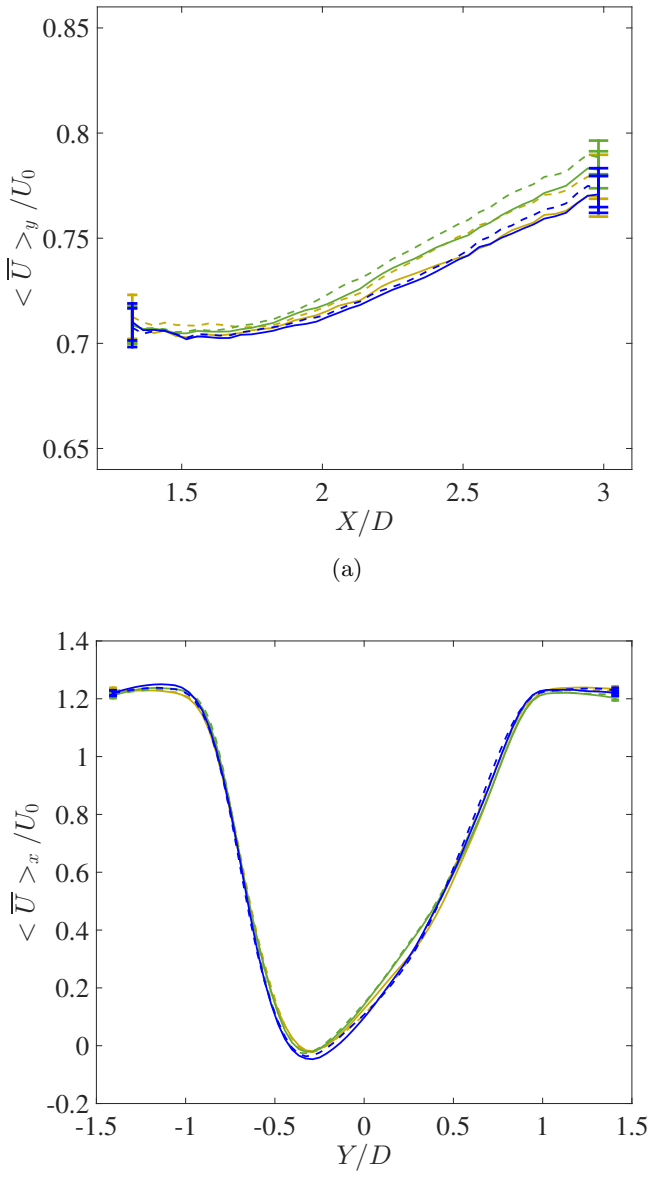

Figure 3.18: Spatio-temporal average in the (a) spanwise and (b) streamwise direction when Re_D is varied and λ is fixed. Solid lines indicate flow-driven conditions and dashed lines indicate motor-driven conditions. Colors correspond to the nominal operating conditions on or below the neutral curve, i.e., $\lambda = 1.45$, $Re_D = 5.1 \times 10^4$ (yellow), $Re_D = 6.6 \times 10^4$ (green), $Re_D = 7.8 \times 10^4$ (blue). The measured conditions for each line are given in Table 3.1. Error bars indicate one standard deviation.

velocity on λ, while relatively little dependence on Reynolds number, as indicated by the overlapping velocity profiles in Figure 3.18. This weak Reynolds number dependence is consistent with the previous results of Bachant & Wosnik (2014). It is interesting to note in Figure 3.17(a) a change in the trend of the velocity recovery as λ increases. Just behind the turbine (i.e., $X/D < 1.5$) as λ is increased from approximately 1.2 (black curve) to 1.5 (blue curve), the velocity decreases. However, as λ is increased further from approximately 1.5 (blue curve) to 1.7 (red curve), the velocity increases in this region. It is speculated that this change in the velocity recovery could be due to the influence of λ on the vortices shed from the turbine, similar to the suppression of vortices observed by Chan *et al.* (2011) in the wake of spinning cylinders. This is explored further in Chapter 4.

To more closely inspect the spatial development of the velocity profile, spanwise sections of the time-averaged velocity are shown in Figure 3.19 for a fixed Re_D and λ. Additionally, the corresponding Reynolds stresses are shown in Figure 3.20 for the same conditions as in Figure 3.19. In both Figures 3.19 and 3.20, there is reasonable agreement observed between

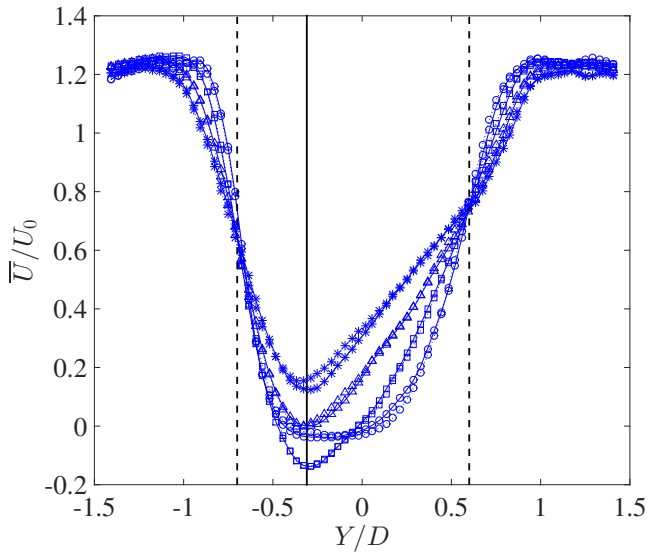

Figure 3.19: Time-averaged streamwise velocity, $\overline{U}$, at ($\circ$) $X/D = 1.3$; ($\square$) $X/D = 1.9$; ($\triangle$) $X/D = 2.5$; and ($*$) $X/D = 3.0$. Symbols connected by a solid line correspond to flow-driven conditions and those connected by a dotted line correspond to motor-driven conditions; both are nominally $Re_D = 7.8 \times 10^4$ and $\lambda = 1.45$. Dashed vertical lines correspond to dominant peaks in the Reynolds stress distributions (c.f. Figure 3.20), i.e., at $Y/D = -0.7$ and $Y/D = 0.6$. The solid vertical line corresponds to the minimum velocity at $Y/D = -0.3$.

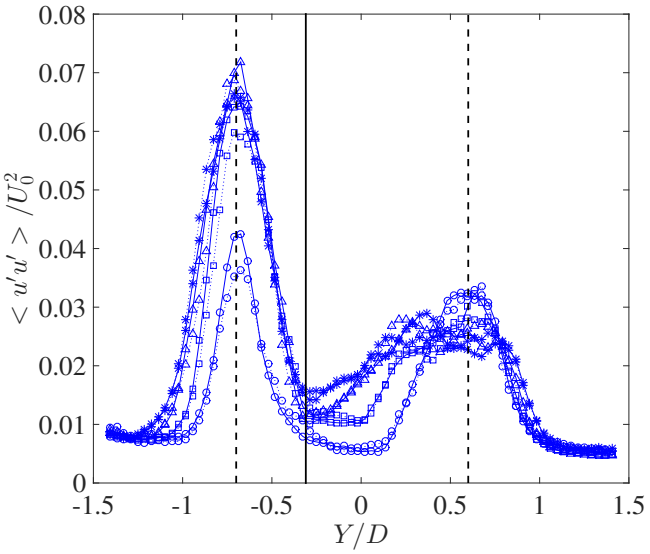

(a)

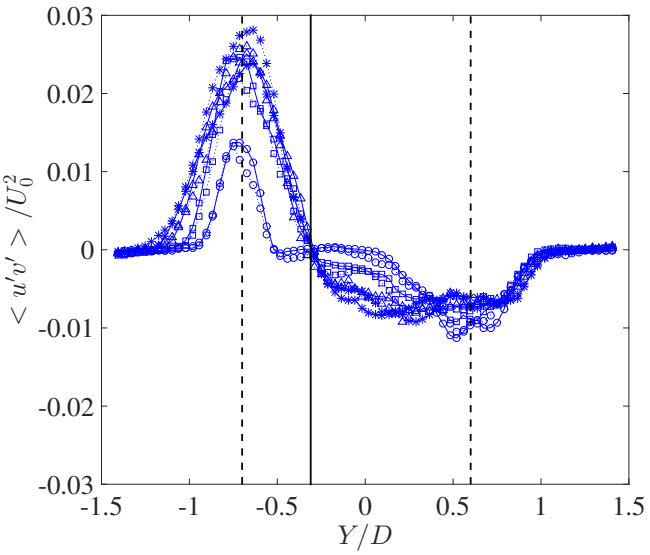

(b)

Figure 3.20: (a) Longitudinal and (b) shear Reynolds stress. All symbols correspond to those of Figure 3.19. Dashed vertical lines correspond to dominant peaks in the Reynolds stress distributions, i.e., at $Y/D = -0.7$ and $Y/D = 0.6$. The solid vertical line corresponds to the minimum velocity at $Y/D = -0.3$

flow-driven and motor-driven conditions, indicated by overlapping symbols that are connected by either solid (flow-driven) or dotted (motor-driven) lines. Comparing Figures 3.17 and 3.19, it is interesting to observe the similarity between the trend in the streamwise development of the velocity profile to the λ dependance of the spatial averages. Specifically, it appears that increasing λ leads to a greater velocity deficit that occurs further downstream, thus delaying the onset of its recovery. Examining Figures 3.19 and 3.20, it is evident that the spanwise asymmetry in the velocity profile is reflected in the asymmetry of the spanwise Reynolds stress distributions. There are two peaks in both the longitudinal and shear Reynolds stresses (i.e., $< u'u' >$ and $< u'v' >$, respectively) that differ in magnitude and occur on either side of the minimum wake velocity. This minimum velocity is shifted away from the centerline of the channel in the direction of the maximum Reynolds stress (i.e., at $Y/D = -0.3$). It is thought that this asymmetry in the wake is initiated by a stronger shear layer that forms on the side of the turbine where the blades advance upstream.

The velocity power spectra for the same cases as discussed above are shown in Figures 3.21 and 3.22. There is again reasonable agreement among the flow-driven and motor-driven cases, indicated by the overlap of the solid and dashed spectral distribution curves. This implies that the underlying vortex dynamics in the wake are virtually unaffected by the use of the motor to mimic the flow-driven turbine kinematics. It is also of interest to note the effect of λ on the distribution of the spectra. Specifically, there appears to be both a broadening and a shift of the largest spectral peak toward lower frequencies with increasing λ, as can be observed between Figures 3.21(a) and 3.21(b). The broader peak suggests more diffuse vortex structures, which is consistent with an earlier decay of shed vortices. Also, since the spectra were sampled at the same X/D location, it further indicates that λ plays a role in the spatial development of these structures, as noted earlier when examining the spatially and temporally averaged velocity profiles. In contrast, the spectral distributions look qualitatively similar between Figures 3.22(a), 3.22(b), and 3.22(c), in which the λ is close to being the same but Re_D differs.

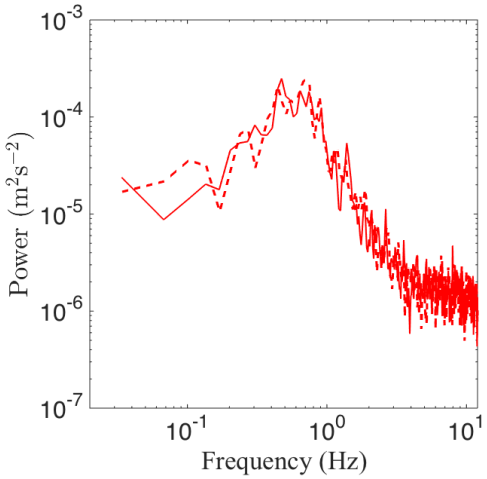

(a)

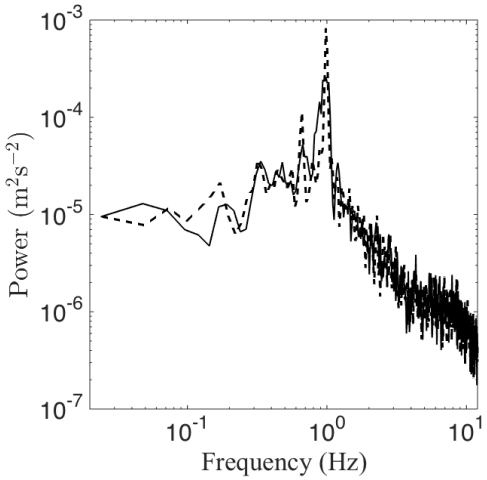

(b)

Figure 3.21: Power spectra for the spanwise fluctuating velocity component, v', in flow-driven (solid lines) and motor-driven (dashed lines) cases. Colors correspond to the nominal operating conditions on or below the neutral curve, i.e., $Re_D = 7.8 \times 10^4$, λ=1.65 (red) and 1.20 (black). The measured conditions for each line are given in Table 3.1.

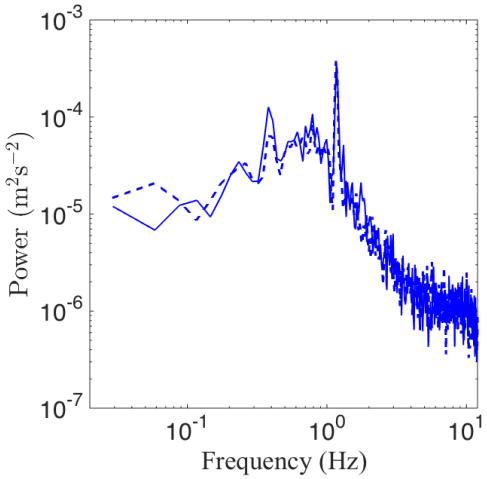

(a)

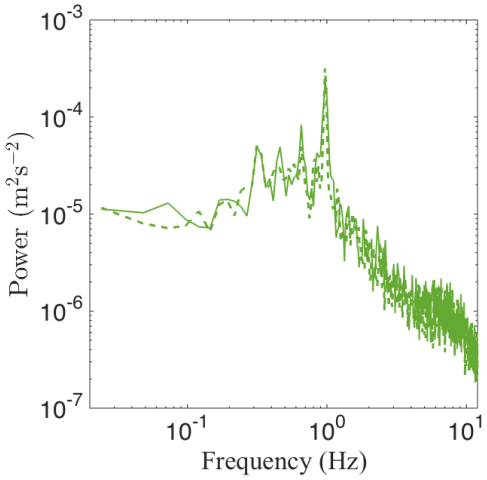

(b)

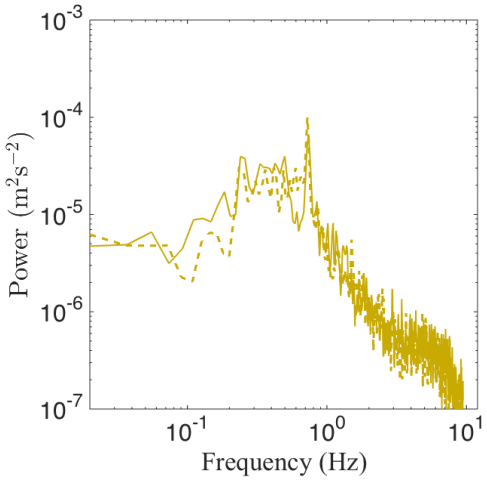

(c)

Figure 3.22: Power spectra for the spanwise fluctuating velocity component, v', in flow-driven (solid lines) and motor-driven (dashed lines) cases. Colors correspond to the nominal operating conditions on or below the neutral curve, i.e., $\lambda = 1.45$, $Re_D = 7.8 \times 10^4$ (blue), 6.6×10^4 (green), and 5.1×10^4 (yellow). The measured conditions are given in Table 3.1.

3.5.2 Measurements on or above the neutral curve

The spatio-temporal average velocity measurements corresponding to the operating conditions given in Table 3.2 are shown in Figures 3.23 and 3.24. Above the neutral curve, it is

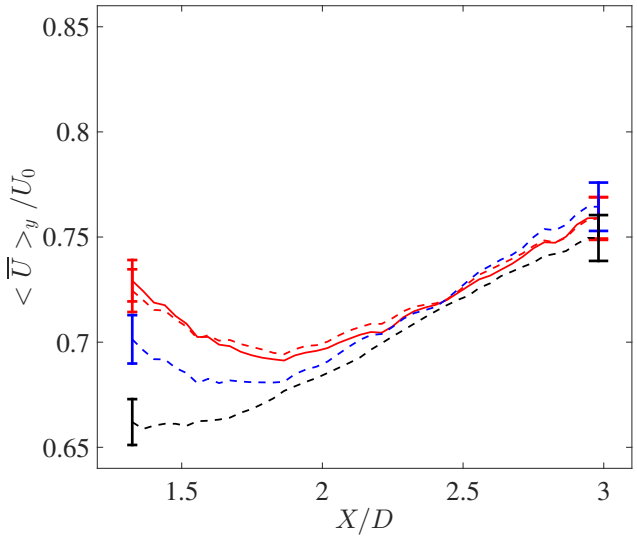

(a)

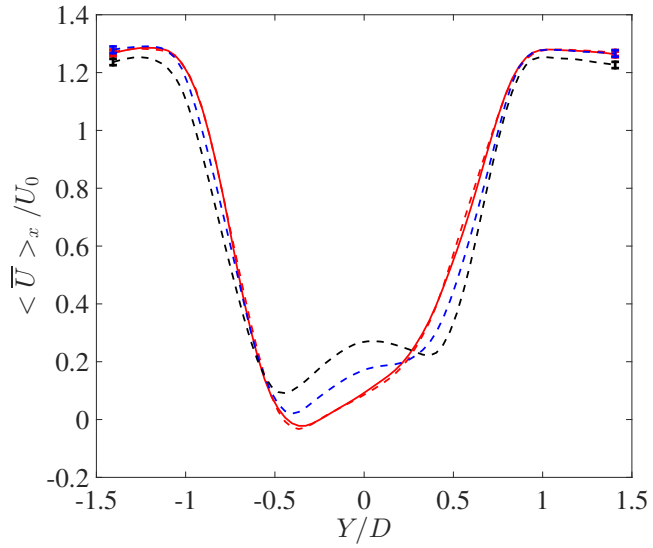

(b)

Figure 3.23: Spatio-temporal average velocity in the (a) spanwise and (b) streamwise direction when Re_D is fixed and λ is varied. Solid lines indicate flow-driven conditions and dashed lines indicate motor-driven conditions. Colors correspond to the nominal operating conditions on or above the neutral curve, i.e., $Re_D = 7.8 \times 10^4$ and λ=1.65 (red), 1.88 (blue), and 2.02 (black). The measured conditions for each line are given in Table 3.2.

not possible to directly compare motor-driven with flow-driven cases as was done previously. However, it is still interesting to note from Figure 3.23 that the shape of the velocity profile continues to be a strong function of λ in this regime.

Figure 3.24 shows a comparison of the velocity profiles between two flow-driven cases along the neutral curve, but at different Reynolds numbers, and one motor-driven case above the neutral curve that attempts to match the λ of the higher Reynolds number, flow-driven case. A somewhat surprising result is that the velocity profile for the motor-driven turbine (dashed green line), operating above the neutral curve, is close to matching the profile of the flow-driven turbine (solid red line) at nearly the same λ but higher Reynolds number. The implications of this result are discussed in the next subsection.

3.5.3 Circulation and torque measurements

Figure 3.25 presents wake circulation measurements for a fixed $Re_D = 7.8 \times 10^4$ and λ ranging from approximately 0.9 - 2.8. There is qualitative agreement in the trend of the net circulation for similar flow-driven and motor-driven cases, though there are slight magnitude differences observed that could not be established conclusively at the precision level of the experiment. Interestingly, there is a change of sign in the circulation near $\lambda \approx 2$, which is above the empirically measured free-spin limit of the turbine at this Reynolds number, which was $\lambda \approx 1.7$. This suggests that just beyond the empirical λ limit, the motor acts to overcome losses in the turbine system while the turbine blades continue to produce net torque due to lift. Beyond the zero crossing in circulation, the turbine blades produce net torque due to drag, which results in wake measurements that are qualitatively different from a flow-driven turbine. Therefore, the zero crossing in circulation represents a measure of the theoretical maximum λ for a motor-driven turbine, below which wake measurements will agree with that of a corresponding flow-driven turbine.

An interesting consequence of this result is that the motor-driven case at $\lambda = 1.88$ (blue curve) in Figure 3.23, which had no corresponding flow-driven case for comparison, can now be considered as a legitimate representation of the flow-driven turbine wake, assuming it could overcome the losses inherent to its system. Additionally, though it is not shown in

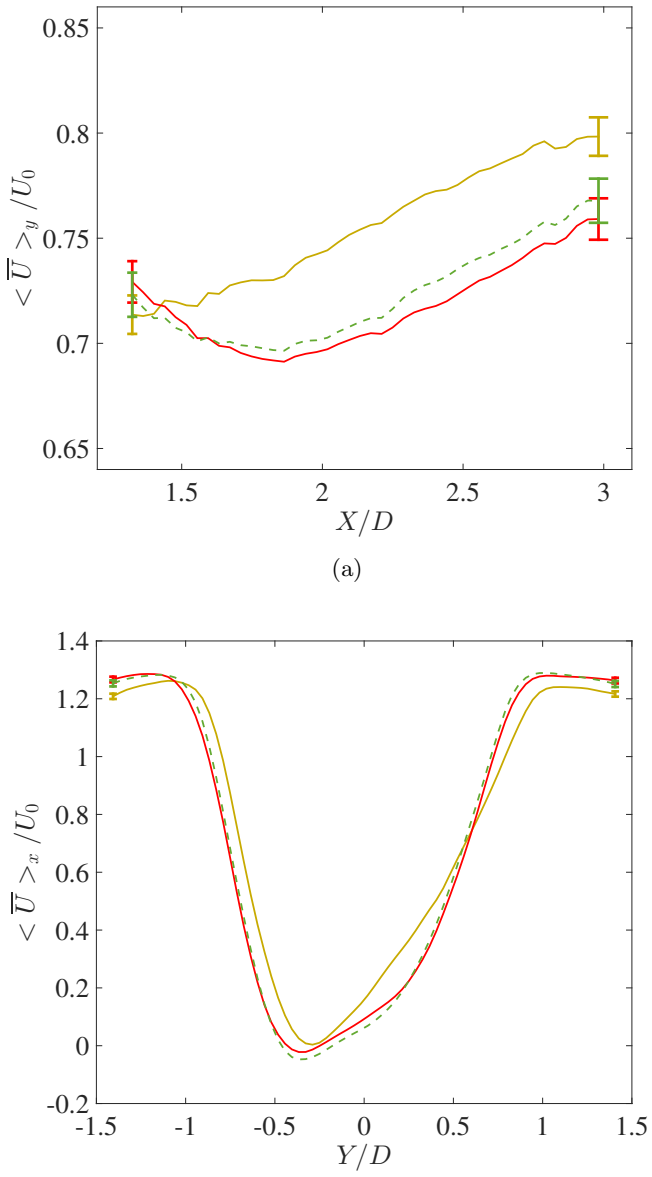

Figure 3.24: Spatio-temporal average in the (a) spanwise and (b) streamwise direction when both Re_D and λ are varied. Solid lines indicate flow-driven conditions and dashed lines indicate motor-driven conditions. Colors correspond to the nominal operating conditions on or above the neutral curve, i.e., $Re_D = 7.8 \times 10^4$ and λ=1.65 (red), $Re_D = 3.7 \times 10^4$ and λ=1.36 (yellow), $Re_D = 3.7 \times 10^4$ and λ=1.65 (green). The measured conditions are given in Table 3.2.

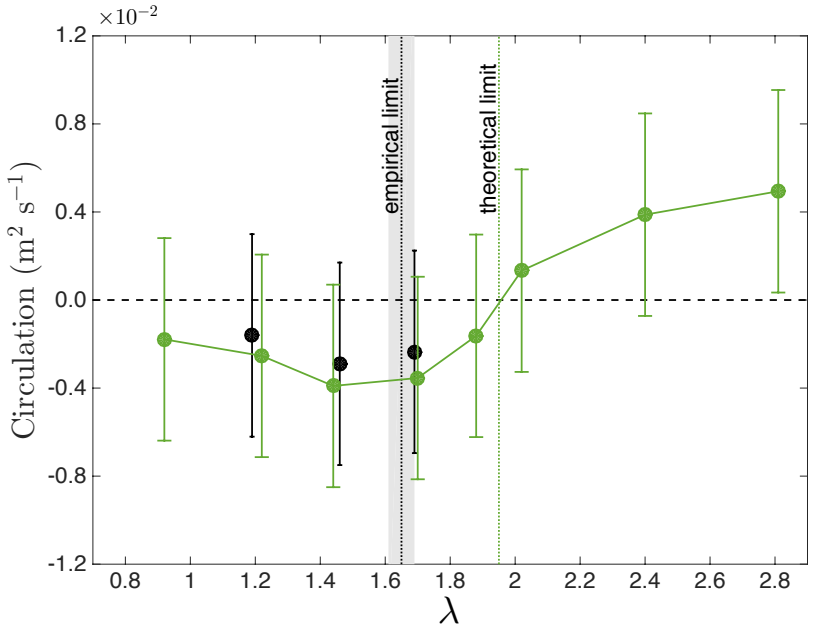

Figure 3.25: Measured circulation for flow-driven (black) and motor-driven (green) cases. Error bars represent an estimate of one standard deviation in measurement error. Motor-driven points are connected with straight line segments.

Figure 3.25, a check of the circulation for the motor-driven case above the neutral curve (green dashed line) in Figure 3.24 gives a value of approximately $-0.2 \times 10^{-2}\ m^2 s^{-1}$. This negative value indicates that the turbine blades are still producing net lift for this case, which is consistent with the observed agreement between the flow-driven (solid red line) and motor-driven (dashed green line) velocity profiles. However, the wake corresponding to the motor-driven case at $\lambda = 2.02$ is unphysical as a representation of a flow-driven turbine.

Turbine shaft torque measurements are shown in Figure 3.26 for the same flow conditions as the circulation in Figure 3.25. There is again good agreement between flow-driven and motor-driven torque measurements. However, the change of sign in torque occurs at an earlier λ than that which was indicated by circulation. This is not surprising given that no effort was made to quantify the torque due to losses in the turbine system. Howell *et al.* (2010) note that in small-scale VAWT experiments the power loss due to bearing friction and windage can be very significant and is a complex function of λ. For low λ, they report that nearly 50% of the total torque produced by the turbine is lost to the bearings, support

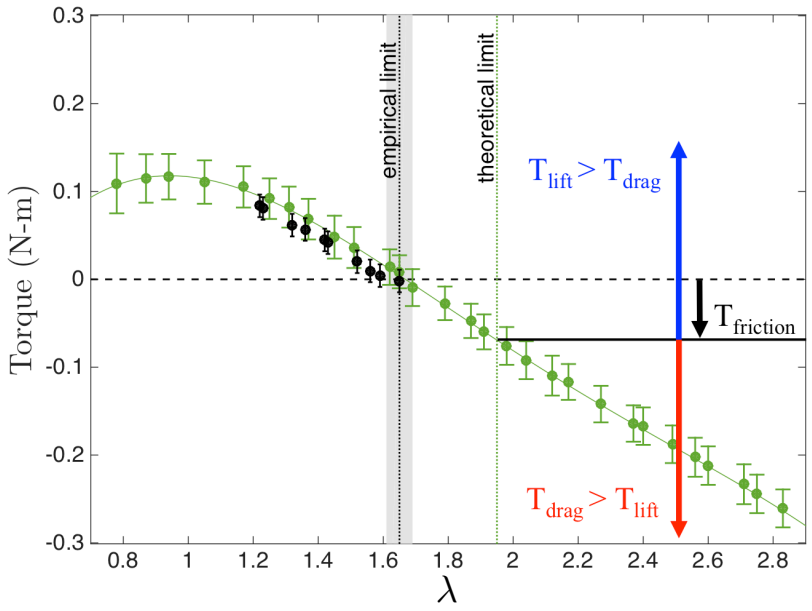

Figure 3.26: Measured torque for flow-driven (black) and motor-driven (green) cases. Error bars represent an estimate of one standard deviation in measurement error. A fourth-order polynomial is fit to the motor-driven points.

arms, and windage in the system; for high λ, these losses were nearly double the torque produced by the turbine. For this reason, the zero crossing in torque provides a conservative estimate of the theoretical maximum λ for a motor-driven turbine to still give reliable wake measurements.

3.6 Conclusion

These results demonstrate the existence of a finite region in λ versus Re number space where a motor-driven turbine can reproduce the physics of a flow-driven turbine. That region extends beyond the free-spin limit of the flow-driven turbine, which is hindered by frictional losses. It was shown that this region is bounded by a sign change in the net circulation of the wake above a given λ threshold, indicating a transition from net torque due to lift to net torque due to drag produced by the turbine blades. Shaft torque measurements support this conclusion by also showing a sign change above the λ threshold set by circulation. However, not accounting for torque losses due to bearing friction and

windage leads to a zero crossing in the torque measurement at a lower λ than is thought to be theoretically possible, making this a more conservative estimate of the λ limit (see '$T_{friction}$' in Figure 3.26). At or below this λ limit, wake measurements agree between a motor-driven turbine and that of a corresponding flow-driven turbine. Further increasing λ beyond this limit, however, leads to the turbine operating in a drag-dominated regime, which gives wake measurements that are inconsistent with a flow-driven turbine.

A notable feature of the wake evaluated in this study is a spanwise (y) asymmetric velocity profile. This is attributed to a stronger shear layer that develops on the side of the turbine where the blades advance upstream and is reflected in an asymmetric Reynolds stress distribution across the span. The velocity in the wake, both averaged and time-varying, was found to be strongly dependent on λ and only weakly dependent on Reynolds number. Increasing λ was found to create a larger velocity deficit with the minimum velocity shifted downstream.

The conclusions of this chapter suggest that the turbine kinematics and aerodynamic properties are the sole factors that govern the dynamics of its wake, irrespective of the means to move the turbine blades. This implies that investigations where turbine blade kinematics are prescribed are justified, and may even allow greater flexibility in experiments where inherent system losses hinder the operational conditions of interest. However, future studies in which turbine rotation is prescribed (either in experiments or numerically) should examine the behavior of the net torque and or wake circulation to confirm that the results are physically meaningful for studies of turbine fluid mechanics.

Chapter 4

Transition to bluff body dynamics in the wake of vertical-axis wind turbines

The material presented in this chapter has been submitted for peer-review and was authored by Araya *et al.* (2015). The author contributions include the following: D.B.A. and J.O.D. designed the experiment; D.B.A. built the experimental setup, collected and analyzed the data, and prepared the manuscript; T.C. aided in the data analysis with conceptual advice and MATLAB scripts for the POD analysis; T.C. and J.O.D. suggested edits to the manuscript, which D.B.A. incorporated into the final submission. Some changes to the text have been made here in order to align it with the rest of the work presented in this thesis.

4.1 Introduction

A unifying characteristic among bluff bodies is a similar far-wake structure independent of the shape of the body. While it is intuitive to consider the flow around an isolated turbine blade in terms of bluff body dynamics, the composite wake of multiple blades originating from a single turbine introduces significant complexity to this analogy. A VAWT proves an interesting example. During its rotation, a straight-bladed VAWT sweeps the surface of a right circular cylinder; thus it is reasonable to postulate that the wake dynamics of the two can be related. This rotation, however, is also one of the complicating factors in drawing an equivalence between the wake of a cylinder and that of a VAWT.

A prominent feature of bluff body flows is the periodic shedding of vorticity into the

wake, which a number of investigators have explored, along with techniques to control it (see, e.g., the review by Choi *et al.*, 2008). One approach relevant to VAWTs is the forced rotation of a cylinder (see, e.g., Mittal & Kumar, 2003), which can lead to vortex suppression when the tip-speed ratio (λ) is greater than unity; this phenomenon has also been observed in pairs of cylinders (Chan *et al.*, 2011). A consequence of vortex suppression is reduced drag, which implies less axial momentum lost in the wake. VAWTs regularly operate at $\lambda > 1$, with some operating potentially as high as $\lambda = 10$ (Sutherland *et al.*, 2012). Furthermore, since the power extracted by a wind turbine scales as the cube of the incoming wind speed, if the rotation of a VAWT causes similar modification of wake vorticity as it does for cylinders, even a modest effect on the mean flow recovery could have substantial implications for controlling power output within a wind farm.

The critical difference between VAWTs and cylinders is that a cylinder rotation must be externally forced, implicitly adding energy to the flow, while a wind turbine extracts energy from the incident flow. As was shown in Chapter 3, the wake dynamics of a VAWT are solely determined by the kinematics and aerodynamic properties of the turbine, irrespective of whether the flow or a motor drives the rotation; this is true provided that the net torque (i.e., time-averaged) due to drag, produced by the blades, does not exceed the net torque due to lift. However, it still remains an open question as to how the difference in energy exchange manifests itself in the wake of a rotating cylinder as compared to that of a VAWT, since their aerodynamic characteristics are significantly different. Additionally, a VAWT typically operates at $Re \approx 10^6$, whereas rotating cylinder experiments where vorticity suppression has been observed were at $Re \approx 10^2$ (Kumar *et al.*, 2011; Chan *et al.*, 2011).

Most experimental investigations of the VAWT wake have focused on either the blade-scale or near-wake aerodynamics. As a VAWT rotates, each turbine blade is subject to dynamic stall as well as blade-wake interactions, both of which are functions of the rotation rate (Laneville & Vittecoq, 1986; Fujisawa & Shibuya, 2001; Ferreira *et al.*, 2009; Edwards *et al.*, 2015). Recent experiments by Dunne & McKeon (2015) demonstrated that the essential physics of the dynamic stall process on a VAWT airfoil can be captured using a low-order model identified by dynamic mode decomposition. In the near-wake of a VAWT, it has

been shown that the flow is characterized by an asymmetrical and three-dimensional mean velocity field, with the dynamics dominated by the vorticity shed from the blades (Battisti *et al.*, 2011; Tescione *et al.*, 2014; Bachant & Wosnik, 2015). Despite these advances, what appears to be lacking is a detailed study of the spatio-temporal evolution of the VAWT wake that extends to the far field.

Recent work by Rolin & Porté-Agel (2015) has examined the far wake of a VAWT, up to approximately 7 rotor diameters downstream of the turbine. They noted that the effect of the boundary layer in the core of the wake was to re-energize the region with downward-entrained momentum. Such characterizations of the far wake are necessary in order to identify its dominant features, which has added significance when turbines are to be placed in close proximity to one another, as in a wind farm. For example, work by Iungo *et al.* (2013) has shown the presence of a hub vortex instability in horizontal-axis wind turbine wakes, which the authors suggest could be excited by the vortex shedding from the rotor disc acting as a bluff body. They also noted that the characterization of the far wake is fundamental for wind farm design due to its practical implications, such as fatigue loads on downstream turbines.

The focus of this chapter is to present new experimental data that explores the spatio-temporal dynamics of the VAWT wake. Specifically, we examine how the dynamics change as the turbine geometry approaches that of a circular cylinder, either statically, by increasing the number of blades, or dynamically, by increasing the tip-speed ratio (λ). Particle image velocimetry is used to measure the velocity in the wake of three different laboratory-scale turbines: a 2-bladed, 3-bladed, and 5-bladed VAWT, as well as a circular cylinder of the same diameter and height as the turbines. The dynamic characteristics of the wake velocity are analyzed using spectral analysis and proper orthogonal decomposition. The time-averaged velocity is also examined and the wake recovery is compared with theoretical approximations for turbulent free-shear flows.

4.2 Experimental methods

4.2.1 Turbine rotor and cylinder geometry

In addition to the 3-bladed turbine model of Chapter 3, two additional model turbine rotors were 3D printed for the experiment using the same material, blade geometry, and rotor diameter as before. A circular cylinder was also constructed with the same height and diameter as the turbines. Acrylic tubing was used for the cylinder body and laser-cut acrylic sheets were used for the cylinder end caps. Together, the cylinder and turbine models accounted for four different values of model solidity, σ, which is defined as

$$\sigma = \frac{nc}{\pi D},$$

where n is the number of blades, c is the chord length, and D is the diameter of the rotor. The model solidity quantifies how the rotor geometry approximates a cylinder of equivalent diameter. Thus it is implicitly assumed that $\sigma \leq 1$, where $\sigma \equiv 1$ for the cylinder model. For the 2-, 3-, and 5-bladed turbine rotor, $\sigma = 0.21, 0.32$, and 0.53, respectively. Figure 4.1 shows drawings of the cylinder and turbine models along with relevant dimensions. The cylinder model had a blockage ratio of approximately 23%, based on its frontal projected area and the cross-section of the channel. The blockage ratio of the 2-bladed turbine rotor varied between approximately 3-8% over one revolution. Similarly, the blockage ratio of the 3- and 5-bladed rotors varied between appriximately 8-16% and 13-25%, respectively. All of the models were mounted using identical hardware in a recirculating water channel facility, as was described in section 3.3.2. A cross-section view of the 3-bladed turbine mounted in the water channel is shown in Figure 4.2, which is reproduced here from section 3.3.2 with the addition of labeling the two PIV planes used in the current set of experiments; this is discussed further in the next section.

4.2.2 PIV setup

Just as described in section 3.3.3, the wake was surveyed using 2D PIV. The majority of the velocity measurements were taken in a plane parallel to the mid-height of each model,

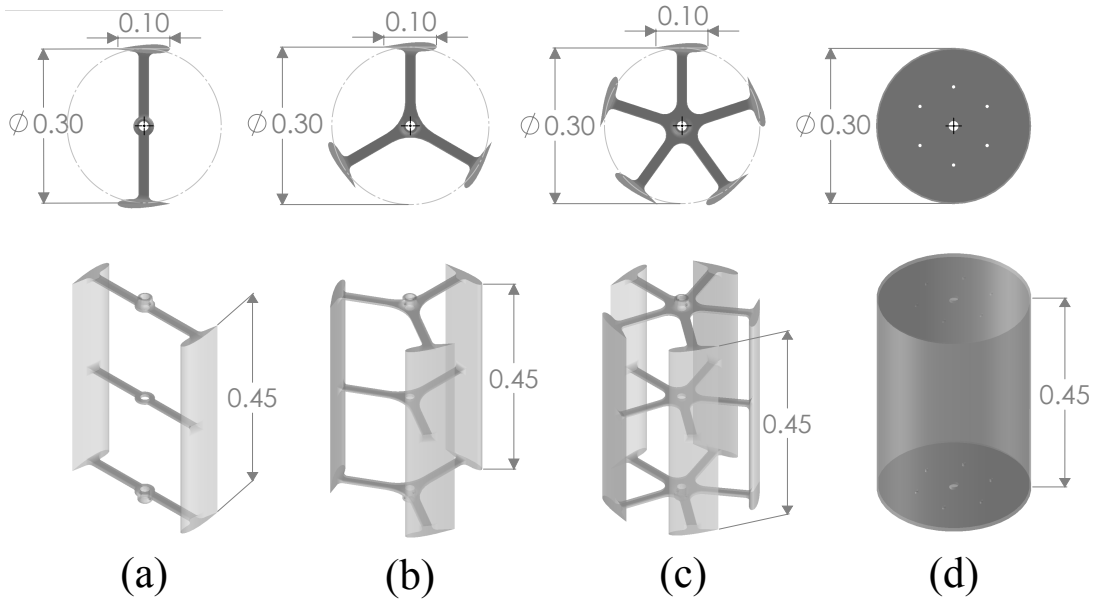

Figure 4.1: Drawings of the (a) 2-bladed VAWT, (b) 3-bladed VAWT, (c) 5-bladed VAWT, and (d) cylinder used for the experiment. Dimensions are in meters.

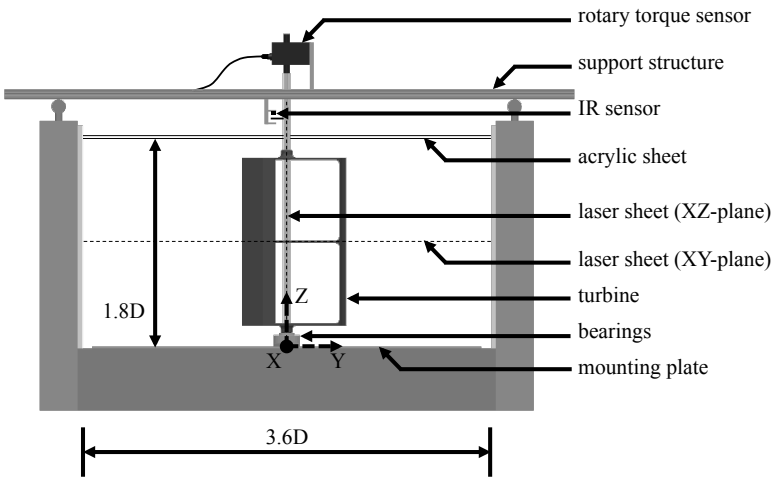

Figure 4.2: Section-view schematic of the experimental setup; $D = 0.3$ m.

indicated in Figure 4.2 as the 'XY-plane'. A plano-concave cylindrical lens with a -3.9 mm focal length was mounted directly in front of the laser to create a collimated laser sheet in this plane. End plates, typically used to minimize three-dimensional effects, were not used in the present study. Instead, the three-dimensionality of the flow was assessed using PIV measurements in a vertical plane parallel to the central shaft of each model, labeled in Figure 3.6 as the 'XZ-plane'. The procedure for the PIV measurements is described in the next section.

4.2.3 Experimental procedure

In all of the experimental runs presented in this chapter, the nominal freestream flow speed was $U_0 = 0.253$ ms^{-1}, i.e., a Reynolds number based on diameter of $Re_D \approx 0.8 \times 10^5$ (see details of the flow speed calibration in section 3.3.3). This value of U_0 is used throughout for normalization purposes. As a check for consistency, the flow speed was actively monitored during each test using a current velocity meter (Swoffer model 2100) placed upstream of the model.

A custom-built infrared (IR) sensor was used to detect the starting orientation of the model in each data set. The voltage signal from the IR sensor, torque sensor, and encoder were input into a National Instruments data acquisition (NIDAQ) device (USB-6221), which was controlled by LabView (National Instruments). Using the TTL signal from the encoder, the NIDAQ device triggered a high-speed camera (Photron APS-RS) with 1024 $\times$1024 pixel resolution to capture two images of the flow every 5° of shaft rotation. Each image sequence was taken at 125 Hz. In the case of the stationary cylinder, pairs of images were captured at a fixed sample rate of 17.7 Hz. A total of 4248 image pairs were captured in a single experimental run, which corresponded to a total of 59 turbine revolutions and approximately 40 cylinder shedding cycles. Additionally, each turbine data set was repeated, yielding a total of 8496 image pairs (118 turbine revolutions) per case. The conditions of each experimental test case are described in Section 4.2.5.

The images were processed using DaVis imaging software (LaVision) to obtain the 2D PIV measurements. The image planes were calibrated using a ruler and a wire mesh with

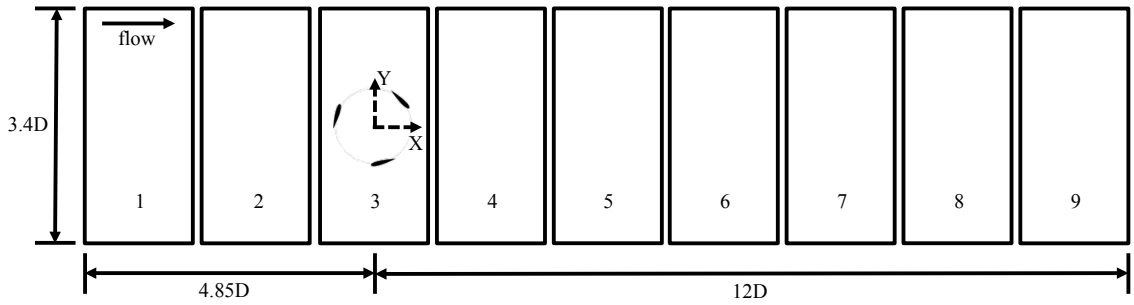

Figure 4.3: Top-view schematic of the nominal turbine position and corresponding PIV windows (1-9) in the XY-plane; $D = 0.3$ m.

equally spaced 2.54 cm squares. A multi-pass PIV algorithm was used with a decreasing interrogation window size and 50% window overlap. Two passes were made with 32 $\times$ 32-pixel interrogation windows, followed by another two passes made with 16 $\times$ 16-pixel windows, the latter of which corresponded to a vector spacing of 1.2 cm in the XY-plane and 0.7 cm in the XZ-plane. A median filter with universal outlier detection was used to remove spurious vectors output by the PIV algorithm; these were subsequently replaced by interpolation.

Figure 4.3 shows a top-view schematic of the nominal position of the 3-bladed turbine along with the corresponding PIV measurement windows in the XY-plane, labeled 1-9. For all PIV measurements, the camera remained fixed and the model was moved to take measurements at different streamwise locations. This was justified given the dimensions of the facility, which had a hydraulic diameter, D_H, of approximately 1 m. The furthest upstream turbine position was approximately 17 D_H from the inlet, giving the freestream flow a reasonable adjustment length in all cases. Figure 4.4 shows a schematic of the 3-bladed turbine model relative to the PIV measurements in the XZ-plane. Only one streamwise location was assessed in this plane.

During PIV measurements, the turbine rotation was either freely spinning or slowed by a DC motor (Pittman GM14904S013-R1) connected to its central shaft. The use of the motor in this manner, as opposed to a purpose-built generator to apply a load to the turbine shaft, was shown in Chapter 3 to not have any adverse effect on the wake velocity measurements. The motor was controlled by a constant voltage power supply (Mastech

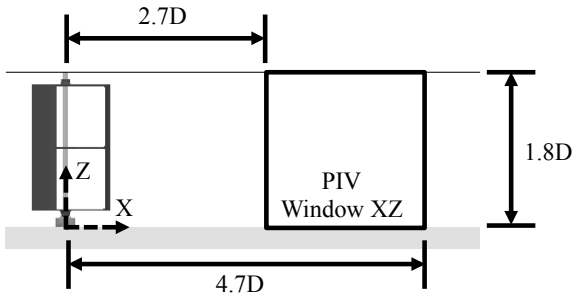

Figure 4.4: Side-view schematic of the PIV measurement window in the XZ-plane; $D = 0.3$ m.

HY3005F-3) capable of providing 0-30 V at 0-5 A. The same motor and setup was also used to drive the cylinder rotation.

4.2.4 Turbine and cylinder power coefficient, C_p

The conditions for the PIV measurements were varied according to the rotation rate of the model, and thus the load applied to its central shaft. Figure 4.5 shows measurements of the average power coefficient, C_p, for all three turbines and cylinder as the tip-speed ratio (λ) was varied. This power coefficient is a measure of the efficiency of power conversion, i.e., the relative rate of kinetic energy extracted from the flow. It is defined as

$$C_p = \frac{\overline{P}}{\frac{1}{2}\rho U_0^3 A},$$

where $\overline{P}$ is the average power (W), or rate of shaft work done by the fluid on the model, A is the projected swept area (m^2) of the model, ρ is the fluid density (kg m^{-3}), and U_0 is the freestream flow speed (m s^{-1}). The average power was estimated from the torque and encoder measurements as $\overline{P} = \overline{T\omega}$, where T and ω are the instantaneous torque (Nm) and angular velocity (rad s^{-1}), respectively. The trends in the measured power curves for the turbines are consistent with numerical predictions by Roh & Kang (2013) for a straight-bladed VAWT with varying solidity; e.g., decreasing solidity yields a zero-crossing in C_p at a higher λ. Additionally, the relatively large standard deviation of C_p among the turbines, indicated by the error bars, is characteristic of the fluctuating torque produced by VAWTs, which is more pronounced in 2-bladed VAWTs due to the alignment of the torque produced

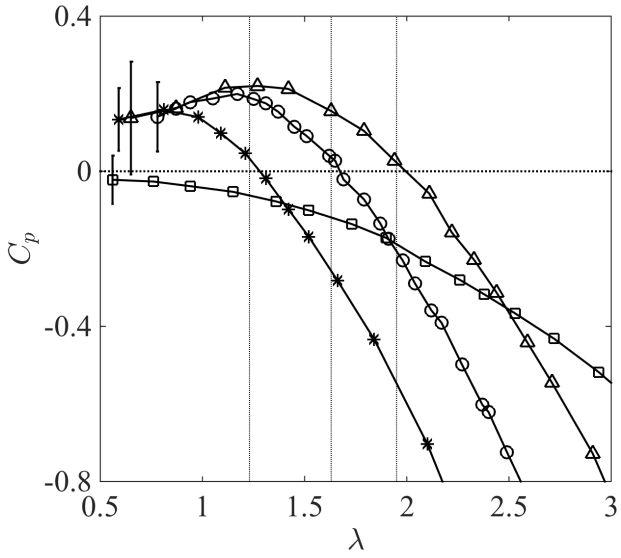

Figure 4.5: Measured values of C_p for the 2-bladed VAWT ($\triangle$), 3-bladed VAWT ($\circ$), 5-bladed VAWT ($*$), and cylinder ($\square$). Error bars indicate one standard deviation in the measured value of C_p. Dashed vertical lines indicate the 'load-free' PIV measurement conditions for the turbines.

by the blades (Sutherland *et al.*, 2012).

For $C_p > 0$, energy is extracted from the flow on average, as in the case of an operational VAWT. Conversely, $C_p < 0$ suggests that on average energy is added to the flow. This is clearly indicated by the C_p measurements for the rotating cylinder, which are always negative since torque must be continuously supplied to sustain its rotation. For the turbines, however, this interpretation is convoluted by torque losses not accounted for in the measured values of C_p, as was discussed in Chapter 3. It can be said, however, that when the value of $C_p = 0$, the turbine is free to rotate, limited only by the net balance of torque inherent to the system, e.g., due to the lift and drag produced by the blades. In all turbine cases, the translational kinetic energy of the incident flow is stored as rotational kinetic energy by the turbine. Assuming viscous losses are negligible, once the turbine rotation reaches an equilibrium, the influx of kinetic energy due to the incident flow is either partially extracted by the turbine ($C_p > 0$), or simply passes through to the wake ($C_p = 0$). In either case, vorticity is shed in the wake due to the interaction of the flow with the turbine blades; it is later shown how this vorticity varies and evolves as the turbine geometry and λ are changed.

Table 4.1: PIV measurement conditions.

Model	Solidity, σ	Loaded/Load-free	λ
5-bladed turbine	0.53	Load-free	1.23
5-bladed turbine	0.53	Loaded	1.01
3-bladed turbine	0.32	Load-free	1.63
3-bladed turbine	0.32	Loaded	1.41
3-bladed turbine	0.32	Loaded	1.20
2-bladed turbine	0.21	Load-free	1.95
2-bladed turbine	0.21	Loaded	1.61
2-bladed turbine	0.21	Loaded	1.22
cylinder	1	Load-free	0
cylinder	1	Loaded	1.69

4.2.5 PIV measurement conditions

PIV measurements were conducted for the conditions shown in table 4.1. These conditions corresponded to both load-free (i.e., $C_p \approx 0$) and loaded-shaft conditions (i.e., $C_p \neq 0$). For the load-free conditions, a comparison was made among the wakes of the four models corresponding to the four model solidities, σ. For the loaded conditions, a comparison was made among the wakes of the three turbines while the average rotation rate was held fixed at $\lambda = 1.2$, and for each turbine while λ was varied; additional measurements were taken for the rotating cylinder at $\lambda = 1.7$.

4.2.6 Calculation of wake statistics

The steady characteristics of the wake were evaluated using the time average of the streamwise component of velocity from the PIV measurements, denoted as $\overline{U}$. Wake dynamics were evaluated using spectral analysis and proper orthogonal decomposition (POD) of both the streamwise (x) and spanwise (y) fluctuating components of the measured velocity, i.e., u' and v', respectively. Phase-averaged vorticity, ω_z, was also calculated from the phase-locked velocity measurements.

A sample of the PIV measurement of $\overline{U}$ is shown in Figure 4.6. Additionally, a segment of the time series of v', the velocity component used in the spectral analysis, is shown in Figure 4.7. This time series was taken from a single point in the flow, indicated in Figure 4.6 by a solid black circle. Also shown in Figure 4.7 is a dotted line, which is a temporal

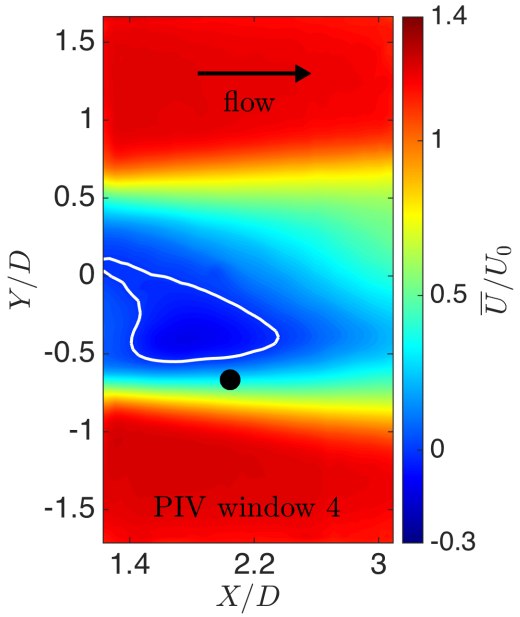

Figure 4.6: Contours of $\overline{U}/U_0$ for the 3-bladed turbine under load-free conditions ($\lambda = 1.63$); the zero-level contour is drawn in white. Measurements correspond to PIV window 4 (c.f. Figure 4.3). The black circle corresponds to the location of the sample time-series in Figure 4.7. Coordinate axes are normalized by the rotor diameter, D.

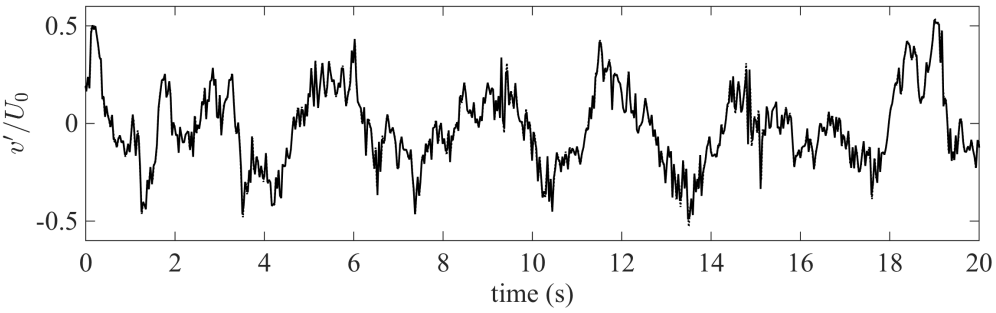

Figure 4.7: Time-series segment of the measured (—) and interpolated (. . .) values of v'/U_0 corresponding to the sample point in figure 4.6.

(spline) interpolation of the measured velocity with a uniform vector spacing in time. This interpolation was a necessary step for the spectral and POD analyses, which are more straightforward to implement with a constant sampling rate. The PIV measurements were not equally distributed in time because they were phase-locked to the turbine rotation, which fluctuated due to the unsteady hydrodynamic torque. However, a temporal interpolation was possible because the camera trigger signal had a known sample rate of 2500 Hz. Thus, each TTL pulse to the camera indicated the time stamp for the corresponding velocity field.

The power spectra for the spanwise component of the velocity fluctuations (v') were computed via the method of Welch (1967). For a given streamwise location (x), the spanwise point (y) was selected based on where the rms of the velocity fluctuations was a maximum, thus indicating the most energetic point along the span. In computing the spectra, a rectangular window function was used with 50% overlap between windows; the frequency resolution was approximately 0.04 Hz.

POD was used to identify the dominant spatial features of the spatio-temporally evolving wake. A thorough review of the method within the context of the analysis and modeling of turbulent flows is given by Berkooz *et al.* (1993). The basic concept of POD is to extract from a dataset an optimal basis for a modal decomposition, in the sense that the error in projecting the data onto a finite number of modes is minimized. In POD, often a small number of modes suffice to describe a large portion of the "energy" (or variance) in the data. For spatio-temporal data, we write

$$v'(\mathbf{x},t) = \sum_{k=1}^{N} a_k(t)\phi_k(\mathbf{x}), \tag{4.1}$$

where the POD modes, ϕ_k, are solutions of the eigenvalue problem

$$R\phi = \lambda\phi,$$

where R is the averaged autocorrelation function $R(\mathbf{x},\mathbf{x}') = \langle v'(\mathbf{x})v'(\mathbf{x}')\rangle$. For data discretely sampled in space and time, the POD modes can be approximated using the method of snapshots (Sirovich, 1987). Snapshots can be associated with instants in time and/or

realizations of the process, and, for stationary processes, can be equivalently represented in the frequency domain via application of the Welch periodogram method to equation (4.1). In this case, the POD modes become the eigenvectors of the cross-spectral-density matrix (for the different observation points). We note that the equivalence between the modes found in the time and frequency domains requires a sufficient number of snapshots for statistical convergence, which was checked by comparing results obtained using the full dataset (e.g., 9000 snapshots for the turbines) and a reduced dataset with half as many snapshots.

In what follows, we refer to the dominant POD mode at a given frequency, which, by definition, contains more energy than the other modes at *that* frequency. We do this for the velocity fluctuations (i.e., neglecting the mean) to be able to compare the dominant near-wake modes oscillating at the blade-passing frequency with the dominant far-wake modes oscillating at the characteristic bluff-body Strouhal number, regardless of their relative global energies. By this approach, the amplitude of the dominant POD mode at a given frequency evolves in time as a traveling wave with fixed frequency and phase. When plotting the spatial contours of this mode across different PIV windows, the relative phase of the mode in each PIV window was manually adjusted in order to visually align the contours. This was necessary since the data collected in each PIV window was a different realization of the same experiment, with the relative phase unknown *a priori* among the realizations.

4.3 Results & discussion

4.3.1 PIV measurements for load-free shaft conditions

Time-averaged PIV measurements of the streamwise component of velocity are shown in Figure 4.8 for the load-free conditions (c.f. table 4.1). The velocity measurements have been normalized by the freestream speed, U_0, and the coordinate axes by the diameter, D. The contour levels are the same in each plot and range in values of $\overline{U}/U_0$ from -0.3 to 1.4. The zero-level contour is shown in white. Within the immediate vicinity of the cylinder and turbine, the large white region in the contour plot is an artifact of shadows created by the model and support structure. However, downstream of the model, this zero-level contour indicates a region of flow recirculation present in each of the four cases shown.

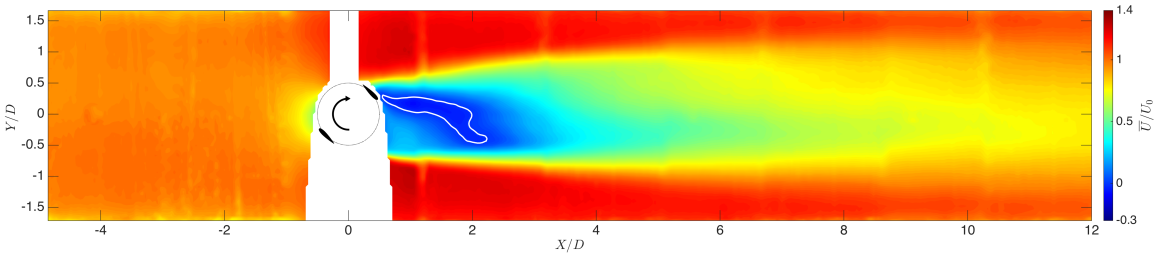

(a)

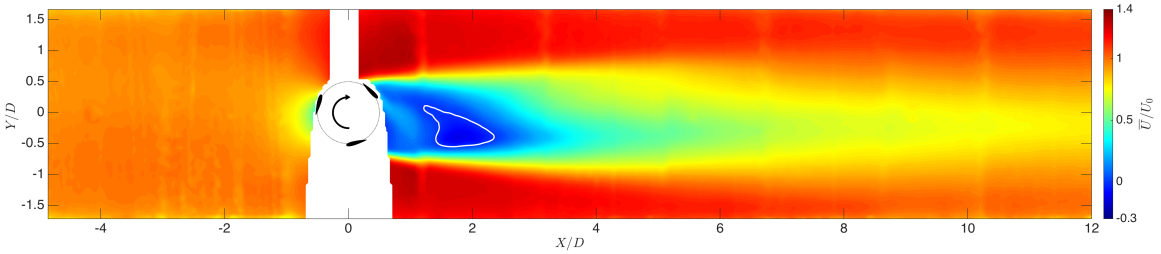

(b)

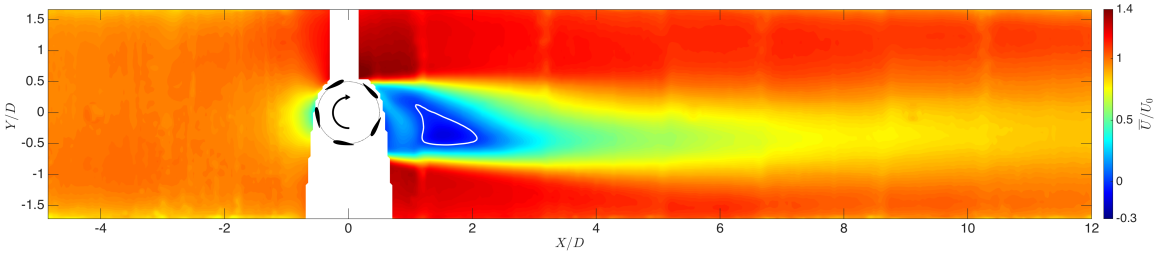

(c)

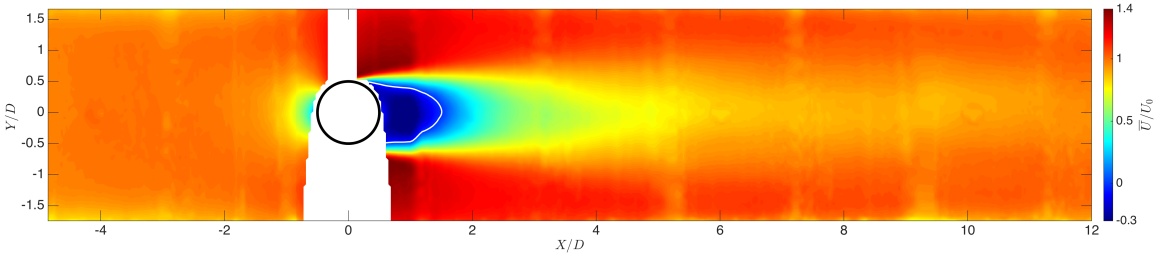

(d)

Figure 4.8: Contours of $\overline{U}/U_0$ measured under load-free conditions for the (a) 2-bladed VAWT, (b) 3-bladed VAWT, (c) 5-bladed VAWT, and (d) cylinder. Airfoil cross-sections for the turbines are drawn to scale.

For the cylinder, this recirculation region is attached to the points of separation from the surface of the model. For the 3- and 5-bladed turbine, the recirculation region is qualitatively similar to that of the cylinder, but is detached from the model and is angled toward the negative y-axis due to the turbine rotation. There is also a recirculation region present in the wake of the 2-bladed turbine, but it is distinct in form to that of the other models, extending from approximately tangent to the blade path to just beyond 2D downstream of the turbine center. The presence of a recirculation region in the wake of each of the turbine models was found to be a function of λ, with decreasing λ causing the region to change in size and in some cases disappear completely. This trend can be readily observed in comparing the contour plots of the current section with those of the remaining cases given in appendix C. In all cases, there is a notable asymmetry of the VAWT wake. This is attributed to the stronger shear layer that forms on the side of the turbine where the blades are advancing upstream. A surprising result, however, is that the deficit in the wake velocity recovers faster with increasing model solidity (σ), with the fastest recovery achieved by the stationary cylinder; there is also a broader wake with decreasing solidity.

Figure 4.9 shows the velocity power spectra computed at five different streamwise locations for each of the cases shown in Figure 4.8. The frequency along the abscissa in these plots has been normalized to give the standard definition of the Strouhal number for cylinder vortex shedding, i.e., $St = fD/U_0$. In the case of the cylinder (c.f. Figure 4.9(d)), the streamwise evolution of the spectra shows a dominant peak near $St \approx 0.2$ that forms and eventually decays with downstream distance, in agreement with existing literature (e.g., Roshko, 1961). For the turbines, however, there is a bi-modal behavior in the evolution of the velocity spectra with downstream distance. In the near-wake region of the turbine, there is a sharp spectral peak that corresponds to the blade-passing frequency. This is consistent with previous investigations of the near-wake region of a VAWT, which has been shown to be dominated by blade-vortex dynamics (see, e.g., Tescione *et al.*, 2014; Bachant & Wosnik, 2015). Further downstream, however, the spectra reveal a transition that occurs in the wake, where the dominant velocity fluctuations shift to a lower frequency of $St \approx 0.26$, roughly independent of the blade-passing frequency. Additionally, at its maxi-

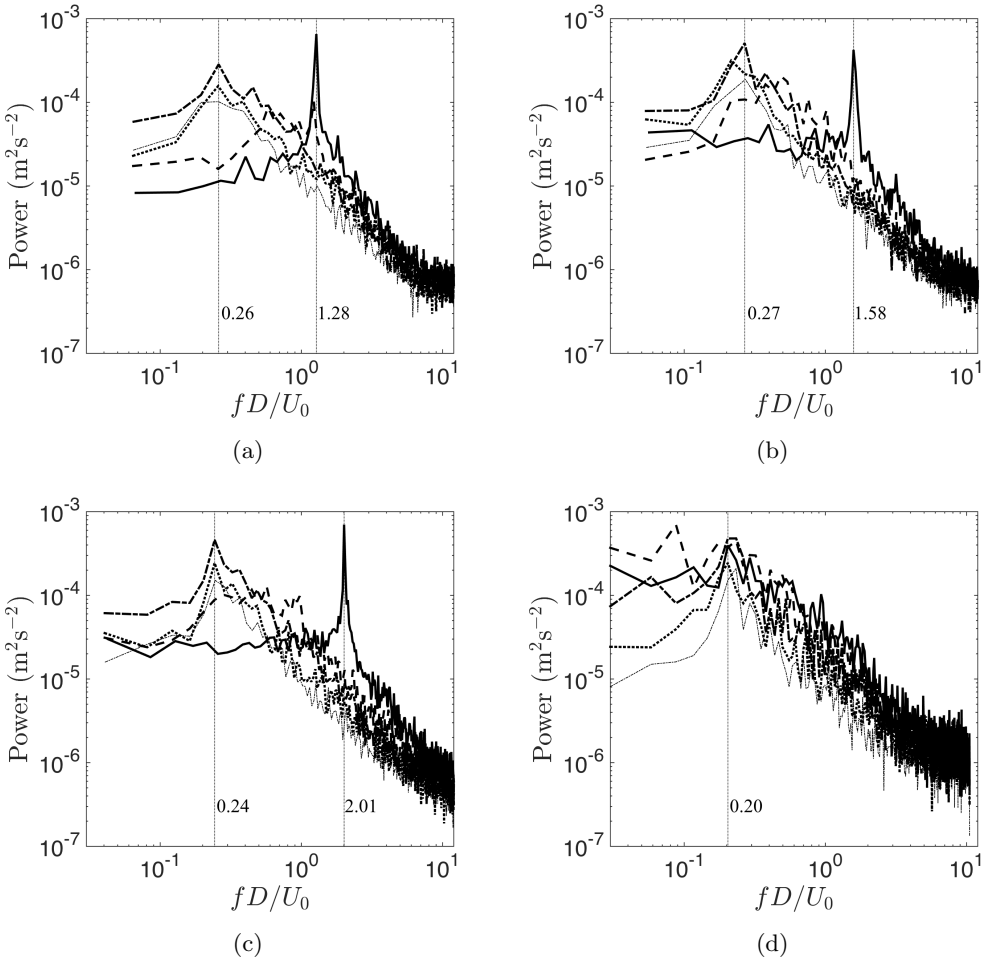

Figure 4.9: Single-point spectra of the velocity fluctuations (v') taken at $X/D = 0.9$ (——), $X/D = 1.7$ (- - -), $X/D = 3.3$ (----), $X/D = 7.3$ (·····), and $X/D = 10.0$ (·····). The spectra correspond to load-free conditions for the (a) 2-bladed VAWT, (b) 3-bladed VAWT, (c) 5-bladed VAWT, and (d) cylinder. Dotted vertical lines correspond to the selected near- and far-wake frequencies of the maximum amplitude in the spectra.

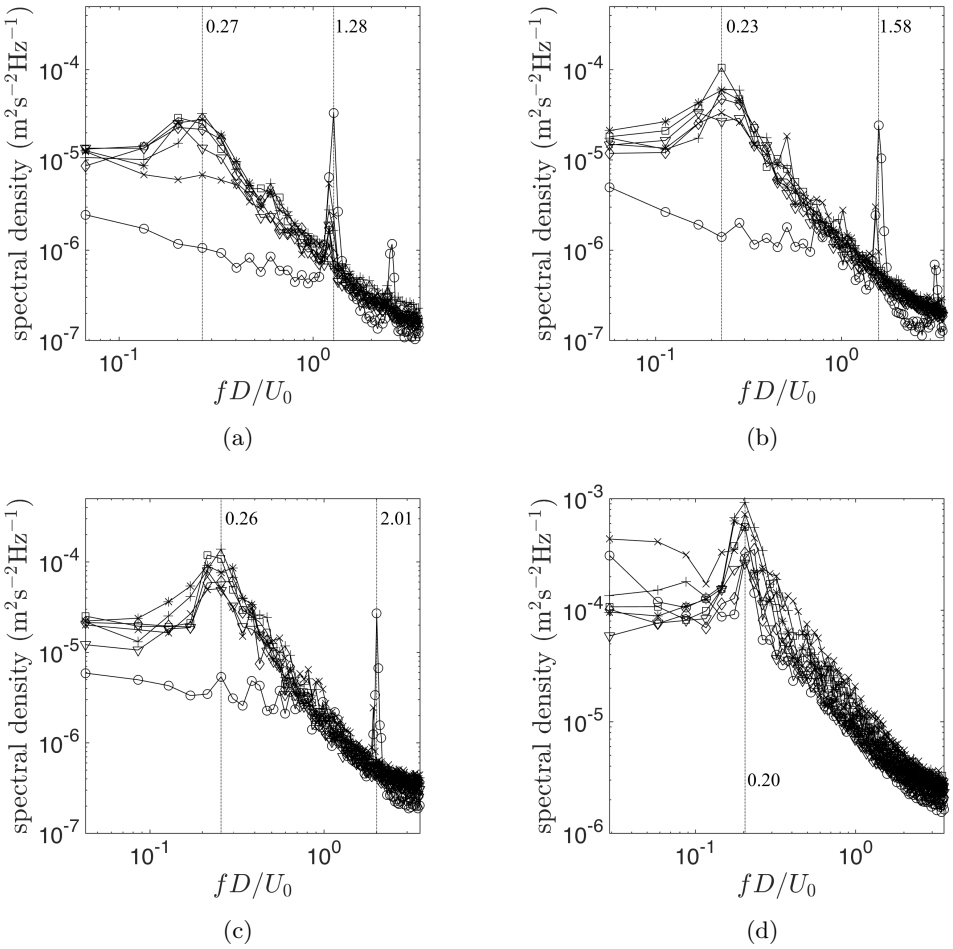

Figure 4.10: Spectra of the time-varying amplitude of the dominant POD mode for the velocity fluctuations under load-free conditions for the (a) 2-bladed VAWT, (b) 3-bladed VAWT, (c) 5-bladed VAWT, and (d) cylinder. The spectra correspond to PIV window 3 ($\circ$), 4 ($\times$), 5 ($+$), 6 ($*$), 7 ($\square$), 8 ($\diamond$) and 9 ($\triangledown$). Dotted vertical lines correspond to the selected near- and far-wake frequencies of the maximum amplitude in the spectra.

mum, the amplitude of the far-wake peak reaches very near to that of the near-wake peak, which suggests that there is a dynamic shift in the energy content of the flow before much of it can be lost to viscous dissipation.

An analysis of the dominant POD mode illustrates the spatio-temporal variation of the velocity fluctuations in the wake. Figure 4.10 shows the power spectral density of the amplitude of the dominant POD mode for the cases shown in Figure 4.8. Each spectrum corresponds to one of the PIV windows. In comparing the local and global spectra of Figures 4.9 and 4.10, respectively, it appears that the dominant POD mode captures the bluff-body

oscillations of the cylinder wake and the bi-modal oscillations present in the VAWT wake. Figure 4.11 shows a comparison of the phase-averaged vorticity field with contours of the dominant POD mode at the blade-passing frequency for each of the three turbines. Since the angular position of the turbine blades in each case is accurately represented in the figure, the vortex structures that are clearly present in the phase-averaged vorticity contours offer a direct interpretation of the structures present in the contours of the spatial mode. More specifically, a pair of positive (red) and negative (blue) structures in the spatial mode contour is representative of the spatial extent of a coherent vortex structure in the turbine wake.

Figures 4.12 and 4.13 show contours of the spanwise (v') and streamwise (u') components of the dominant POD mode at the far-wake peak frequency (c.f. Figure 4.10), respectively, for the same flow conditions as before. There is a strong resemblance between the spatial mode structure in far wake of the VAWT to that of the cylinder, especially as the turbine solidity (σ) is increased. The structure of the cylinder mode is consistent with what has been previously reported (see, e.g., Feng *et al.*, 2011), and the alternating pattern of vortices shed from the cylinder can again be inferred by the pairs of structures within the spatial mode contour, i.e., a single vortex structure is represented by two spatial mode structures with alternating sign. This implies that the far wake of the VAWT is characterized by large-scale structures that are typically periodic in both space and time and alternate in sign, akin to a bluff body. This bluff body mode tends to be stronger in amplitude on the windward side of the turbine, i.e., where the stronger shear layer is formed, indicating that it is likely caused by an underlying shear-layer instability. It also appears as though the development of these far-wake structures in the VAWT wake is delayed downstream as the turbine solidity is reduced. However, in these load-free conditions, the rotation rate of the turbine was uncontrolled, which adds an additional variable to consider in the analysis. These variables are decoupled in the following section.

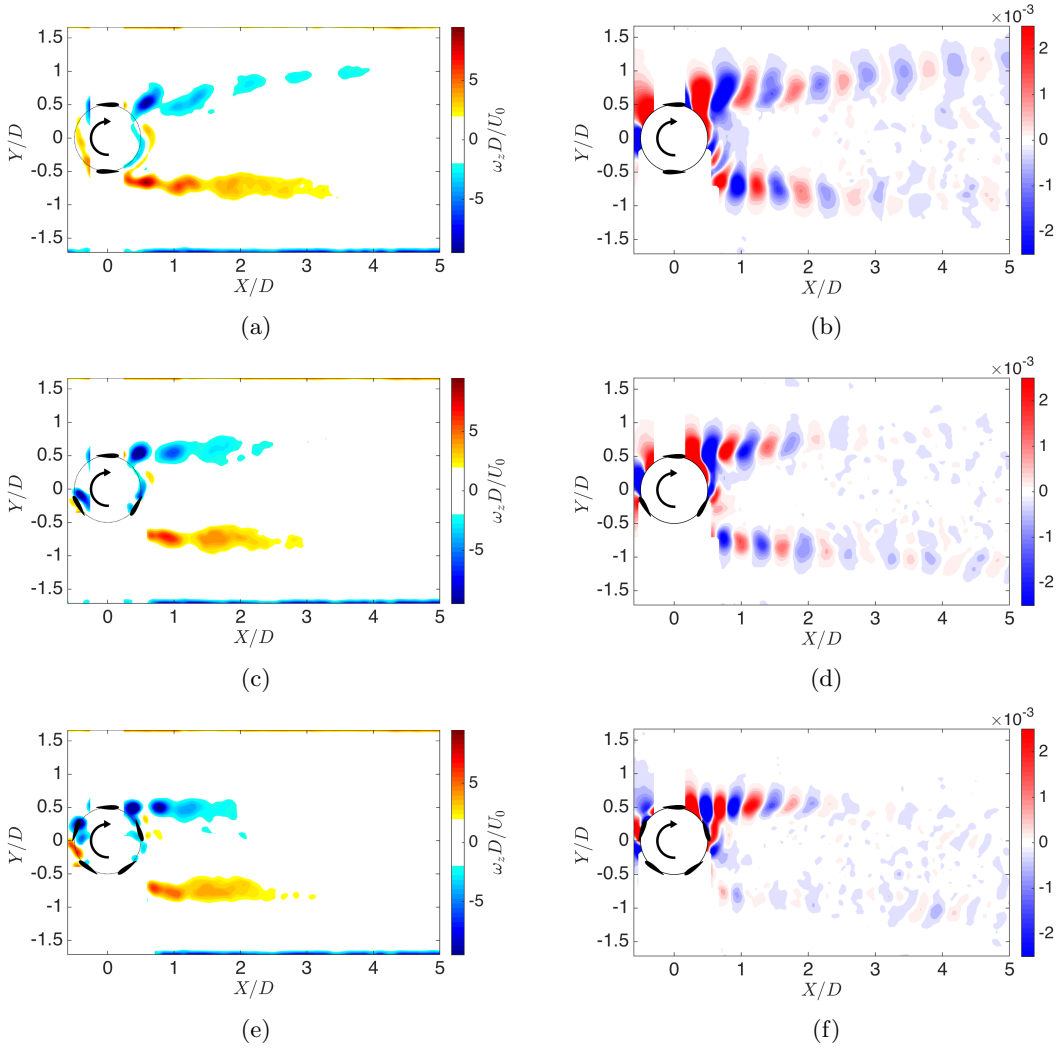

Figure 4.11: Left half: Contours of the phase-averaged vorticity for the (a) 2-bladed VAWT, (c) 3-bladed VAWT, and (e) 5-bladed VAWT. Right half: Contours of the spanwise component (v') of the dominant POD mode for the velocity fluctuations at the blade-passing frequency for the (b) 2-bladed VAWT, (d) 3-bladed VAWT, and (f) 5-bladed VAWT. Airfoil cross-sections and angular positions are accurately represented in the figure. The dashed circle in each plot is for reference and corresponds to the turbine diameter.

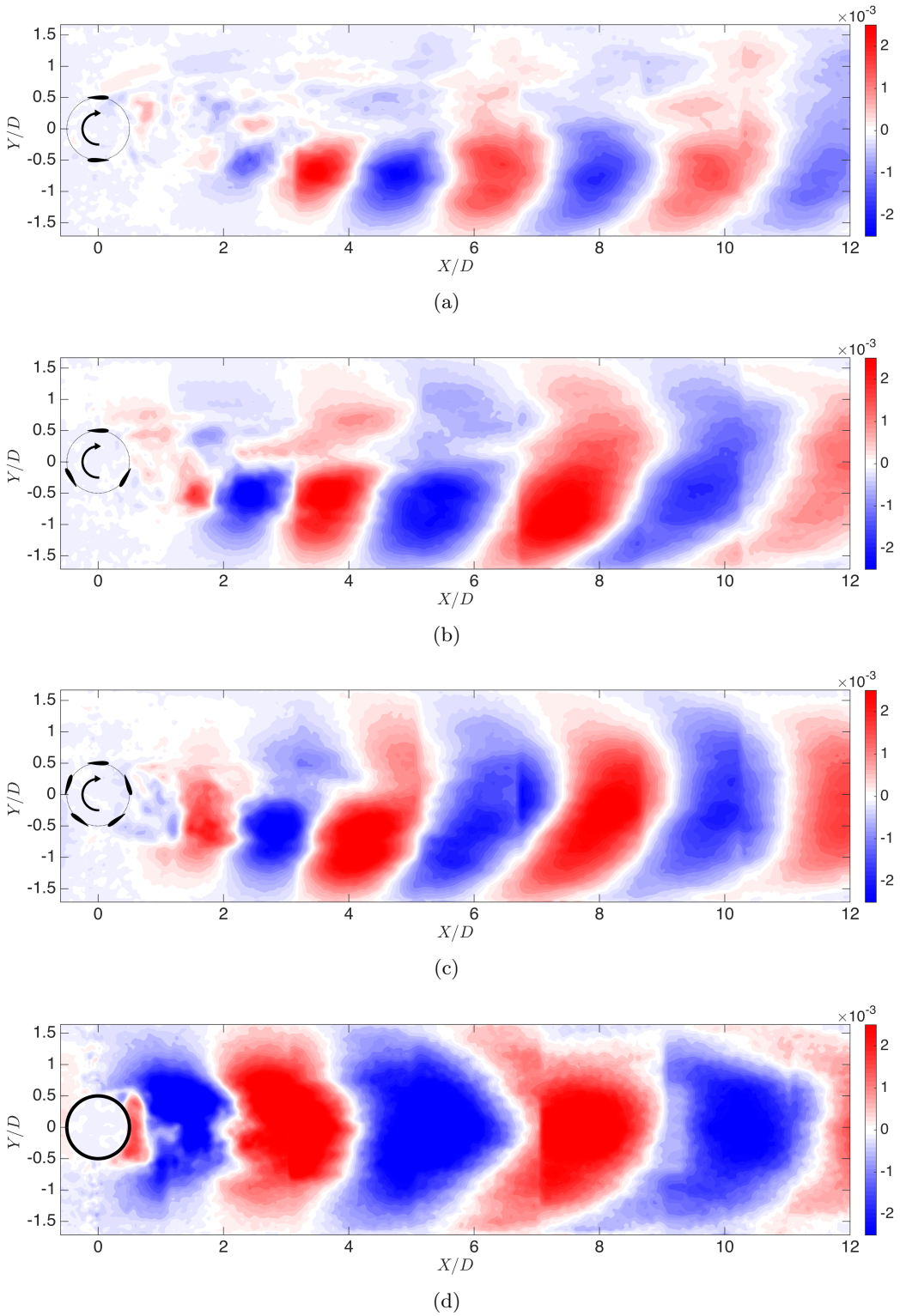

Figure 4.12: Contours of the spanwise component (v') of the dominant POD mode for the velocity fluctuations at the far-wake peak frequency (c.f. Figure 4.10) for the (a) 2-bladed VAWT, (b) 3-bladed VAWT, (c) 5-bladed VAWT, (d) and cylinder. Airfoil cross-sections and angular positions are accurately represented in the figure. The dashed circle in the turbine plots is for reference only and corresponds to the turbine diameter. The solid circle represents the cylinder diameter, D.

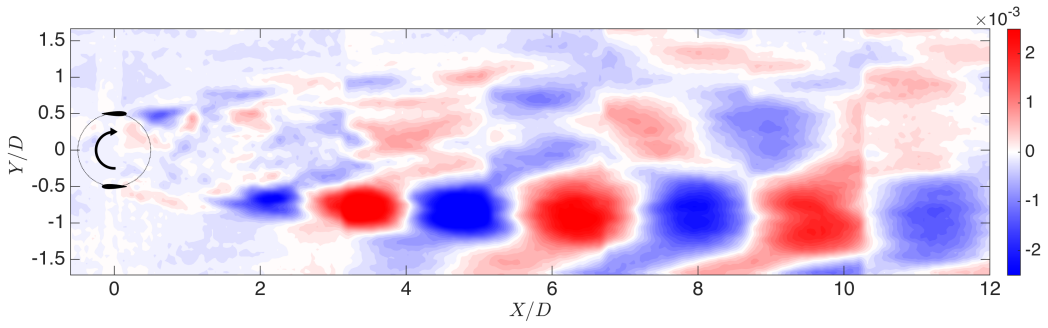

(a)

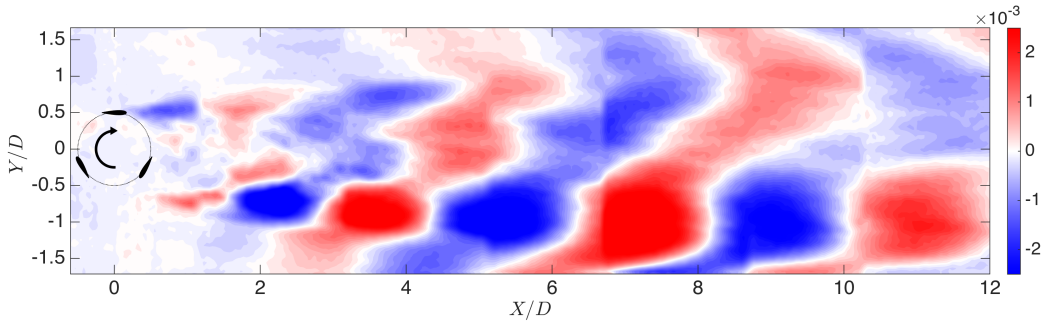

(b)

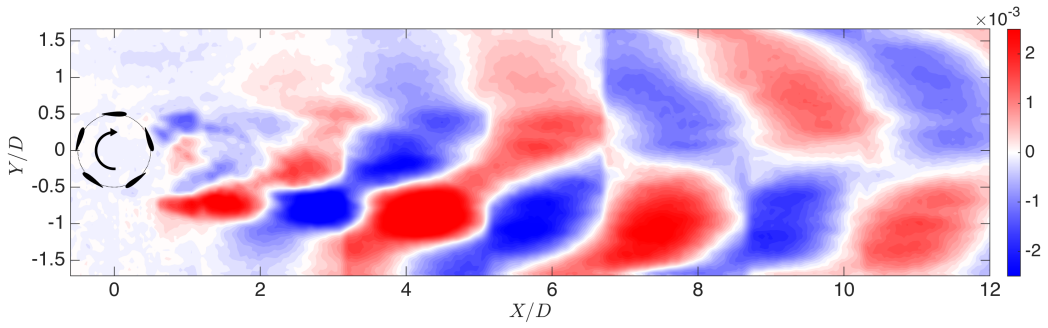

(c)

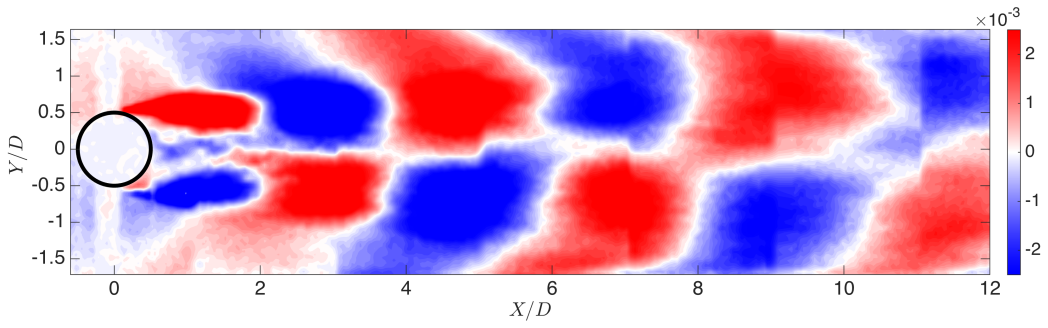

(d)

Figure 4.13: Contours of the streamwise component (u') of the dominant POD mode for the velocity fluctuations at the far-wake peak frequency (c.f. Figure 4.10) for the (a) 2-bladed VAWT, (b) 3-bladed VAWT, (c) 5-bladed VAWT, (d) and cylinder. Airfoil cross-sections and angular positions are accurately represented in the figure. The dashed circle in the turbine plots is for reference only and corresponds to the turbine diameter. The solid circle represents the cylinder diameter, D.

4.3.2 PIV measurements for loaded-shaft conditions

To separate the effects of increasing the turbine solidity from varying its rotation, both were evaluated independently. The same procedure was followed as before, but only the results of the POD mode analysis are presented here; the corresponding spectra are given in appendix C. Figure 4.14 shows contours of the spanwise velocity component of the dominant POD mode while λ was held fixed and σ was varied. Note that in this figure the dominant mode at two distinct frequencies have been superposed together, i.e., the dominant frequency in the near and far wake. The combination of these two temporal frequencies gives a broad look at the dominant spatial structure of the evolving wake. Immediately apparent from Figure 4.14 is that increasing σ leads to an earlier transition to bluff-body oscillations in the VAWT wake. Also apparent is that, as σ is decreased, there is a sharp increase in the strength of the vortices that are shed from the blades, which can be deduced from the larger amplitude and spatial extent of the mode structure.

Figure 4.15 shows contours of the spanwise velocity component of the dominant POD mode for the 3-bladed turbine while its rotation rate was varied from $\lambda \approx$ 1.2-1.6. As before, the dominant mode at the near- and far-wake peak frequency have been superposed together. Despite the small range of λ, a similar shift in transition is observed among these cases as was when varying the solidity, with the transition occurring closer to the turbine with increasing λ. This suggests the concept of an apparent solidity for the turbine due to both its geometric solidity as well as its rotation rate, which we derive in the following section.

4.3.3 Dynamic solidity of a VAWT

The effects of geometric solidity and rotation rate can be combined using the concept of a 'dynamic solidity'. In the limit of $\lambda >> 1$, there is little time for the incident flow to react to the passage of the turbine blades, resulting in the turbine rotor appearing to the flow as like a solid cylinder. Conversely, when $\lambda = 0$, the interaction of the incident flow with the turbine blades is indeterminate, since it depends on the orientation of the rotor. However, for a given orientation, a larger geometric solidity (σ) means that the turbine rotor

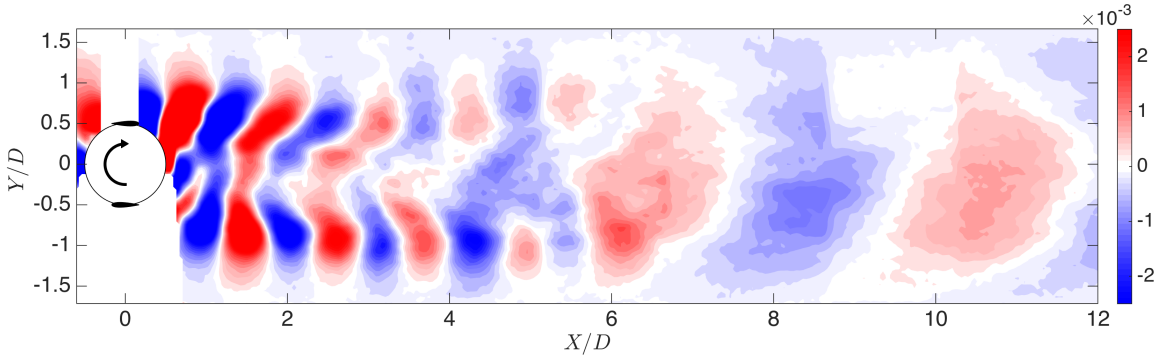

(a)

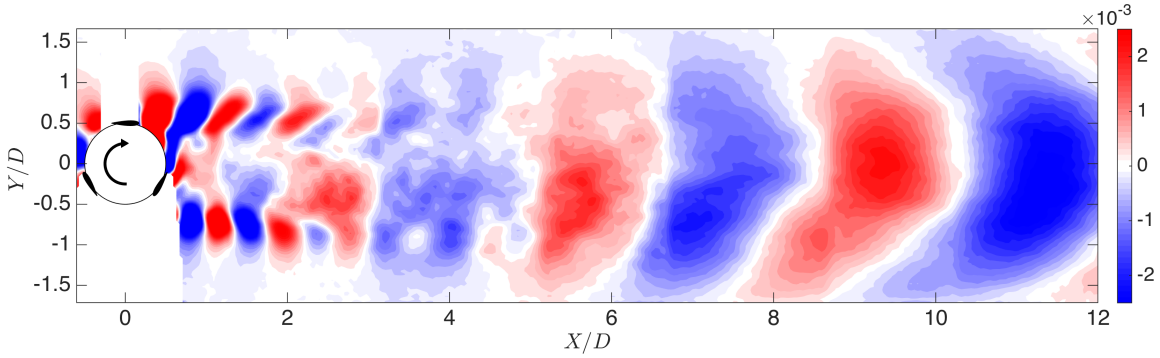

(b)

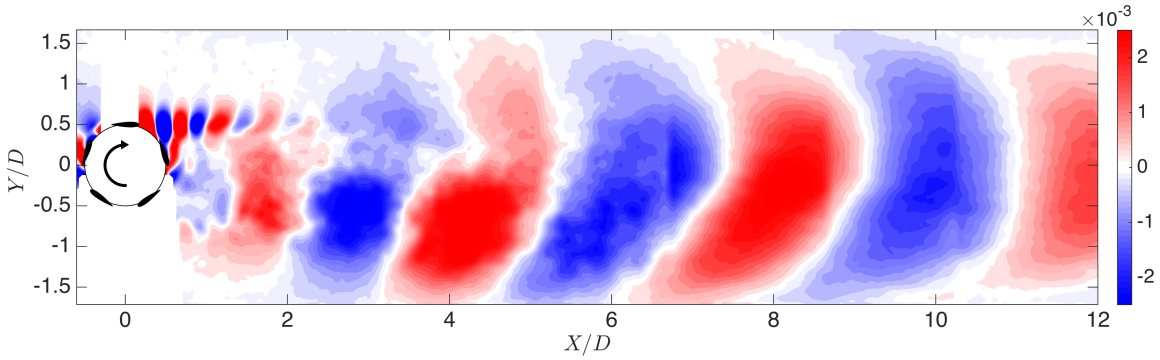

(c)

Figure 4.14: Contours of the spanwise component (v') of the dominant POD mode for the velocity fluctuations at both the near and far-wake peak frequencies (c.f. Figure 4.10) for the (a) 2-bladed VAWT, (b) 3-bladed VAWT, and (c) 5-bladed VAWT. In each case, $\lambda \approx 1.2$. Airfoil cross-sections and angular positions are accurately represented in the figure. The dashed circle in the turbine plots is for reference only and corresponds to the turbine diameter.

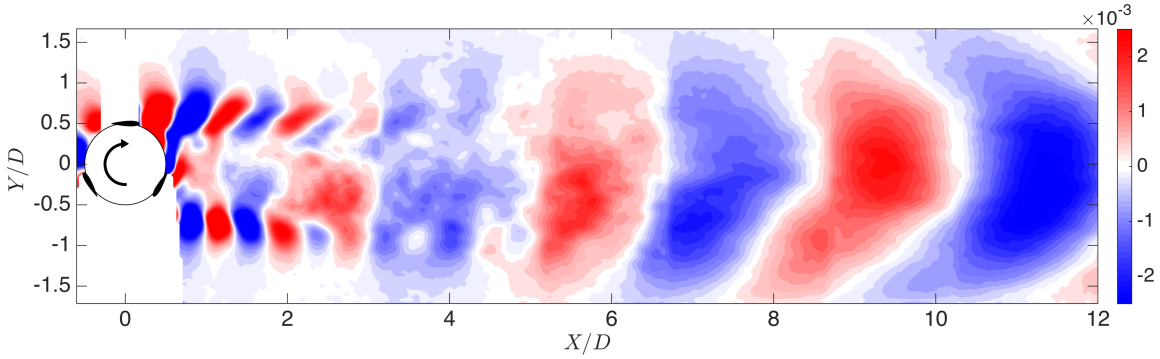

(a)

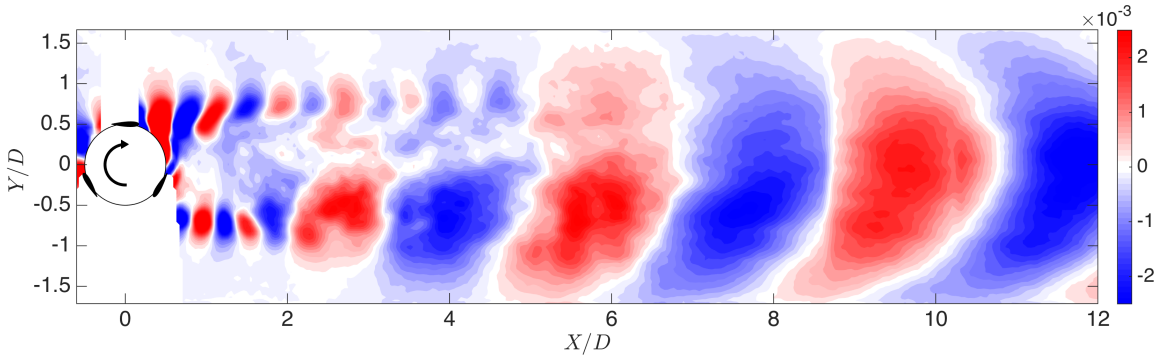

(b)

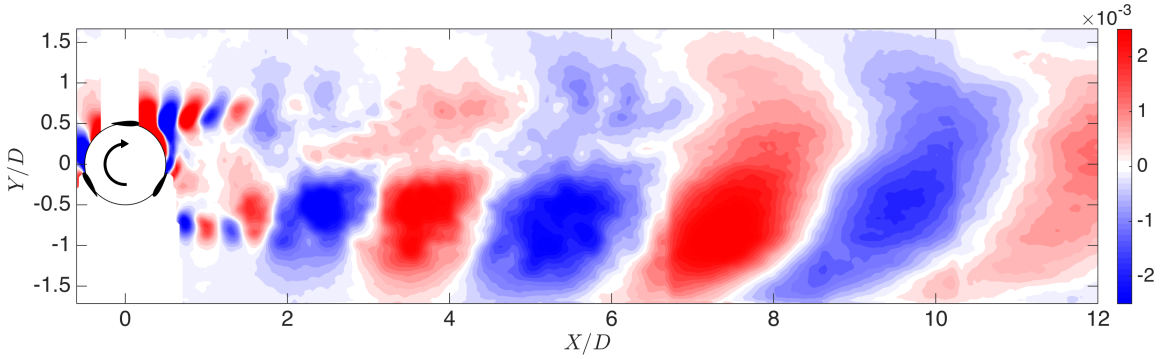

(c)

Figure 4.15: Contours of the spanwise component (v') of the dominant POD mode for the velocity fluctuations at both the near and far-wake peak frequencies (c.f. Figure 4.10). The contours plots correspond to the 3-bladed VAWT with an average rotation rate of (a) λ = 1.20, (b) λ = 1.41, and (c) λ = 1.63. Airfoil cross-sections and angular positions are accurately represented in the figure. The dashed circle in the turbine plots is for reference only and corresponds to the turbine diameter.

approaches the geometry of a cylinder, and thus would interact with the flow accordingly.

One way to quantify these limits is to formulate a dynamic solidity parameter, σ_D, using the characteristic scales of the flow. We first define a characteristic length scale, l, as the sum of the gaps in the circumference of the turbine rotor, i.e., $l = \pi D(1 - \sigma)$. Using this, we define a VAWT time scale, t_V, as

$$t_V = \frac{l}{nU_0\lambda},$$

where n is the number of blades. This represents the time required for the turbine blades to collectively sweep through the distance to close the gaps between the blades. Next, we define a convective time scale, $t_{conv} = l/U_0$, which represents the amount of time required for a freestream fluid particle to travel the same distance. The ratio t_V/t_{conv} represents the percentage of convection time required to close the gaps between the blades, with a smaller percentage resulting in the turbine appearing more solid to the incident flow. We multiply this ratio of time scales by a geometric factor, R/c, where R is the turbine radius, and c is the chord length, to incorporate the rotor geometry, and subtract this quantity from unity to give the definition of dynamic solidity as

$$\sigma_D = 1 - \frac{R}{c}\frac{t_V}{t_{conv}} = 1 - \frac{1}{2\pi\sigma\lambda}.$$

Note that this definition follows the aforementioned limiting behaviors. For a given rotor geometry and $\lambda >> 1$, $\sigma_D \approx 1$, corresponding to the geometric solidity of a solid cylinder ($\sigma = 1$). When $\lambda = 0$, σ_D is indeterminate. Similarly, if $\lambda < 1/2\pi\sigma$, which is practically insignificant, then $\sigma_D < 0$, which loses physical meaning. However, for $\lambda > 1/2\pi\sigma$, σ_D increases monotonically with increasing either σ or λ. Figure 4.16 shows how σ_D varies with λ and σ for a turbine with fixed chord length ($c = 0.1$ m) and rotor diameter ($D = 0.3$ m), as in the present experiment. Also shown in the figure are the conditions measured during the experiment, indicated by symbols. The relation between σ_D and the transition to bluff body dynamics in the VAWT wake is explored in the next section.

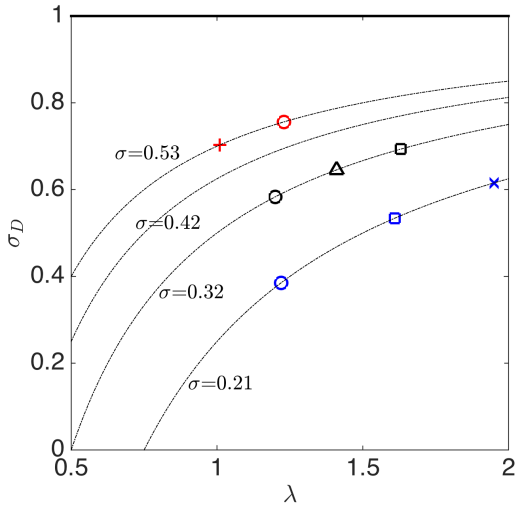

Figure 4.16: Dynamic solidity, σ_D, variation with λ and σ. Measured values are shown with colors and symbols that correspond to the following: the 2-bladed turbine for λ = 1.95(×), 1.61(□), and 1.22(○), the 3-bladed turbine for λ = 1.63(□), 1.41(△), and 1.20(○), the 5-bladed turbine for λ = 1.23(○) and λ = 1.01(+).

4.3.4 Effect of dynamic solidity on wake transition

Figure 4.17 shows a plot of Strouhal number versus normalized downstream distance for all of the cases shown in Figure 4.16 with the addition of the stationary cylinder measurements. Each point in the figure indicates the frequency of the maximum amplitude in a single velocity spectrum, denoted as $St_{\max}$. The plot was constructed by computing the single-point velocity spectra for all of the PIV measurements at each of the streamwise locations downstream of each model. This is a convenient way to express all of the data at once, and it illustrates what has already been shown for a few cases, e.g., the bi-modal behavior of the VAWT wake. As the near-wake vortices decay, the transition to bluff-body oscillations in the far wake is indicated in Figure 4.17 by the collapse of the data toward $St = 0.2$. The streamwise location of the start of the transition in each case is marked by dashed vertical lines in the figure. These were selected to correspond to the final streamwise location where the effect of blade shedding can be seen as the dominant peak in the spectra. The scatter of the data in the far wake is due in part to the spectral resolution, which was $St \approx \pm 0.05$ for all cases, limited by the sample size. Additionally, the slight increase away from $St = 0.2$ is speculated to be an effect of the VAWT's rotation. In rotating cylinder experiments, Lam

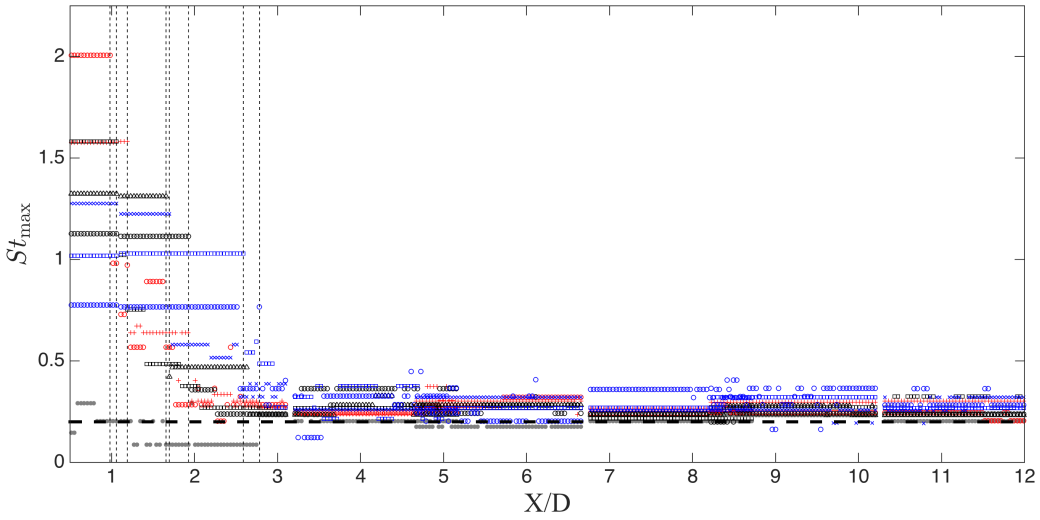

Figure 4.17: Normalized frequency of the maximum amplitude in the velocity spectra, $St_{\max}$. Colors and symbols correspond to the following: the 2-bladed turbine for $\lambda = 1.95(\times)$, $1.61(\square)$, and $1.22(\circ)$, the 3-bladed turbine for $\lambda = 1.63(\square)$, $1.41(\triangle)$, and $1.20(\circ)$, the 5-bladed turbine for $\lambda = 1.23(\circ)$ and $\lambda = 1.01(+)$, and the stationary cylinder $(\bullet)$. Downstream distance, X, is normalized by the model diameter, D. The horizontal dashed line corresponds to $St_{\max} = 0.2$. Vertical dashed lines correspond to the location of the streamwise transition points in each case, i.e., $X/D_{\text{transition}}$.

(2009) observed an increase in the vortex shedding frequency from $St = 0.18$ to 0.29 as the cylinder's rotation was increased from $\lambda = 0$ to 1.68.

It was found that there exists a strong correlation between the dynamic solidity, σ_D, and the downstream transition location, $X/D_{\text{transition}}$, as shown in Figure 4.18. Note that the transition location for the cylinder is defined to be $X/D_{\text{transition}} \equiv 0$. The linear equation that describes this correlation is referred to in the subsequent sections and is given as the following:

$$X/D_{\text{transition}} = 4.78 - 4.93\sigma_D. \tag{4.2}$$

When the abscissa of each case in Figure 4.17 is normalized by $X/D_{\text{transition}}$, given by equation 4.2, and the ordinate axis by the non-dimensional blade-passing frequency in each case, St_{blade}, defined as

$$St_{\text{blade}} = \frac{f_{\text{blade}} D}{U_0} = \left(\frac{nU_0\lambda}{\pi D}\right)\frac{D}{U_0} = \frac{n\lambda}{\pi},$$

the result is shown in Figure 4.19, which indicates a collapse of the data in the near wake

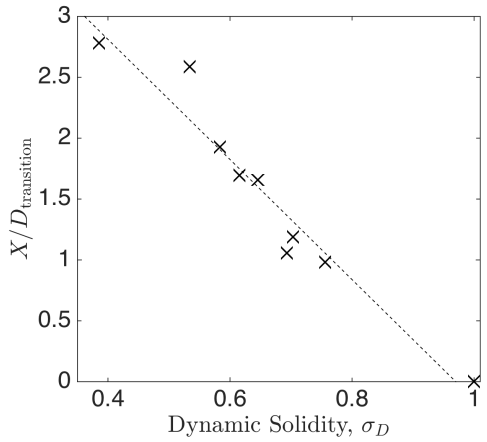

Figure 4.18: Linear correlation ($R^2 = 0.94$) between the streamwise location of wake transition, i.e., $X/D_{\text{transition}}$, and dynamic solidity, σ_D.

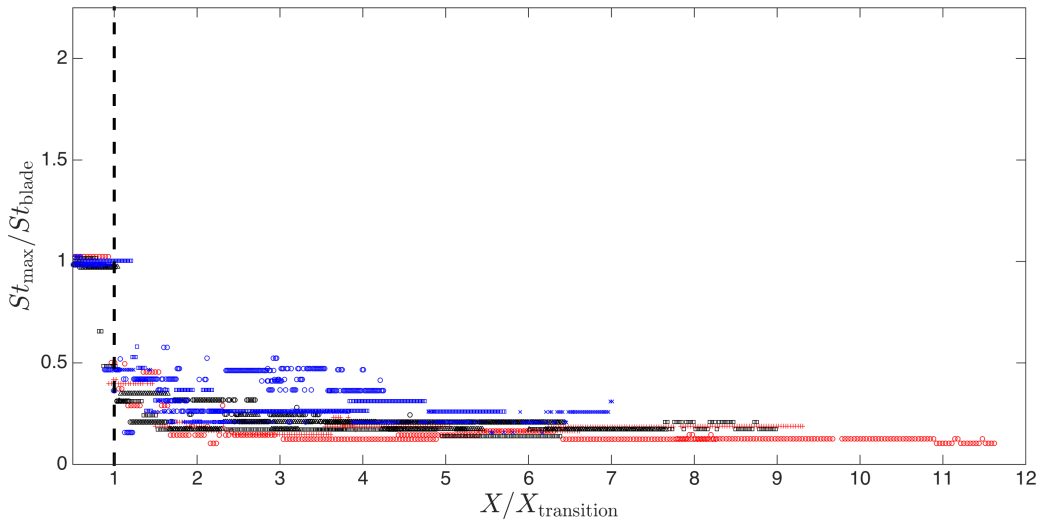

Figure 4.19: Ratio of St_{max} to the normalized blade-passing frequency, St_{blade}. Colors and symbols correspond to the following: the 2-bladed turbine for $\lambda = 1.95(\times)$, $1.61(\square)$, and $1.22(\circ)$, the 3-bladed turbine for $\lambda = 1.63(\square)$, $1.41(\triangle)$, and $1.20(\circ)$, and the 5-bladed turbine for $\lambda = 1.23(\circ)$ and $\lambda = 1.01(+)$. Downstream distance, X, is normalized by $X_{\text{transition}}$ given by equation 4.2. The vertical dashed line corresponds to $X/X_{\text{transition}} = 1$, the streamwise transition location in the VAWT wake.

and an alignment of the start of the far-wake transition. The implication of this finding is that the downstream distance at which point the VAWT wake begins to transition to a state dominated by bluff body dynamics, i.e., $X_{\text{transition}}$, can be predicted using a simple relation between the turbine geometry and its kinematics.

4.3.5 Effect of dynamic solidity on velocity recovery

Having explored the behavior of the VAWT wake dynamics, it is of interest to see how this relates to the recovery of the wake velocity deficit. For a given streamwise location, the minimum velocity was found by taking the minimum across the span (neglecting measurement points near the walls). Figure 4.20 shows the time-average of the minimum streamwise component of velocity, $\overline{U}_{\text{min}}$, measured for the cases corresponding to Figure 4.17. Upon examining Figure 4.20, it can be observed that the velocity deficit and its subsequent recovery happen in a similar manner for all cases. However, the recovery occurs at a different rate initially in each case, indicated by the slopes of the curves. Additionally, we can compare the absolute minimum of the streamwise component of velocity in the wake, taken to be the minimum of the velocity profiles shown in Figure 4.20. Figure 4.21 shows a plot of this absolute minimum velocity versus the dynamic solidity in each case. There is again a significant correlation between these two variables. Physically, this is consistent with the idea that the more solid the turbine appears to the incoming flow, the greater the initial velocity deficit is in the wake.

To compare the rate of recovery of the velocity deficit, we first rescale the ordinate axis of Figure 4.20 by the absolute minimum velocity, $\min(\overline{U}_{\text{min}})$, such that all of the curves have the same initial deficit, shown in Figure 4.22. If we then assume that the recovery rate reaches an equilibrium in all cases by 12 D downstream of the turbine center (i.e., the furthest downstream measurement point) and plot this rescaled velocity against dynamic solidity, the result is shown in Figure 4.23. The strong correlation between the final rescaled minimum velocity and the dynamic solidity indicates that increasing the dynamic solidity results in a faster rate of recovery of the velocity deficit in the wake.

Since there is a strong correlation between the recovery of the velocity deficit and the

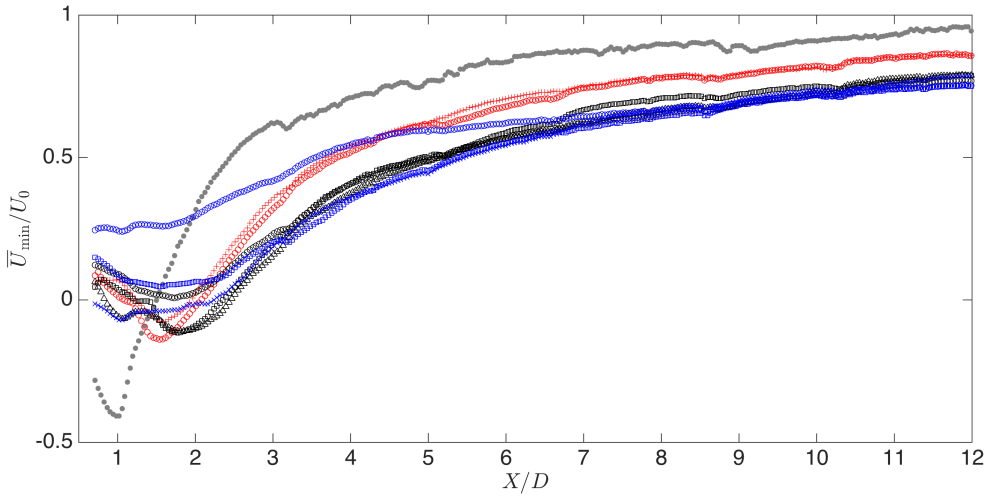

Figure 4.20: Minimum streamwise velocity across the span, $\overline{U}_{\min}$. Colors and symbols correspond to the following: the 2-bladed turbine for $\lambda = 1.95(\times)$, $1.61(\square)$, and $1.22(\circ)$, the 3-bladed turbine for $\lambda = 1.63(\square)$, $1.41(\triangle)$, and $1.20(\circ)$, the 5-bladed turbine for $\lambda = 1.23(\circ)$ and $\lambda = 1.01(+)$, and the stationary cylinder ($\bullet$). Downstream distance, X, is normalized by the model diameter, D, and velocity by the freestream speed, U_0.

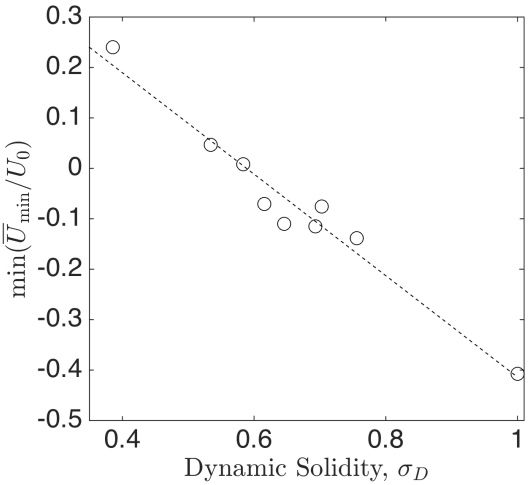

Figure 4.21: Linear correlation ($R^2 = 0.96$) between the normalized absolute minimum streamwise velocity across the span, $\min(\overline{U}_{\min}/U_0)$ and the dynamic solidity, σ_D.

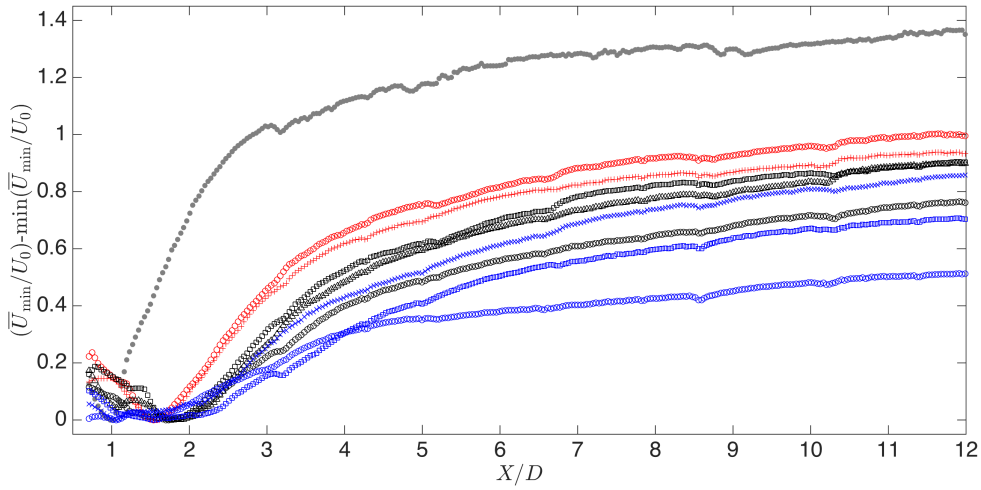

Figure 4.22: Minimum streamwise velocity, $\overline{U}_{\min}$, rescaled by the absolute minimum velocity across the span, i.e., $\min(\overline{U}_{\min})$. Colors and symbols correspond to the following: the 2-bladed turbine for $\lambda = 1.95(\times)$, $1.61(\square)$, and $1.22(\circ)$, the 3-bladed turbine for $\lambda = 1.63(\square)$, $1.41(\triangle)$, and $1.20(\circ)$, the 5-bladed turbine for $\lambda = 1.23(\circ)$ and $\lambda = 1.01(+)$, and the stationary cylinder $(\bullet)$. Downstream distance X is normalized by the model diameter, D, and velocity by the freestream speed, U_0.

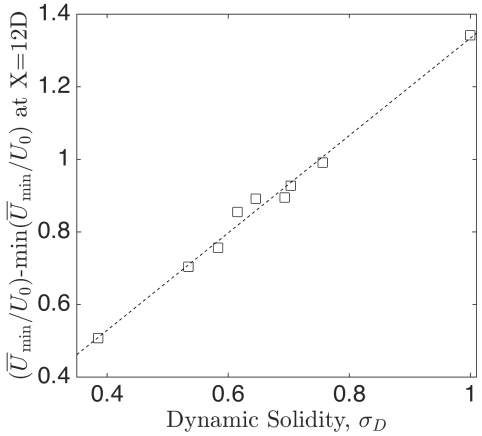

Figure 4.23: Linear correlation ($R^2 = 0.99$) between the rescaled streamwise velocity of Figure 4.22 at $X/D = 12$ and the dynamic solidity, σ_D.

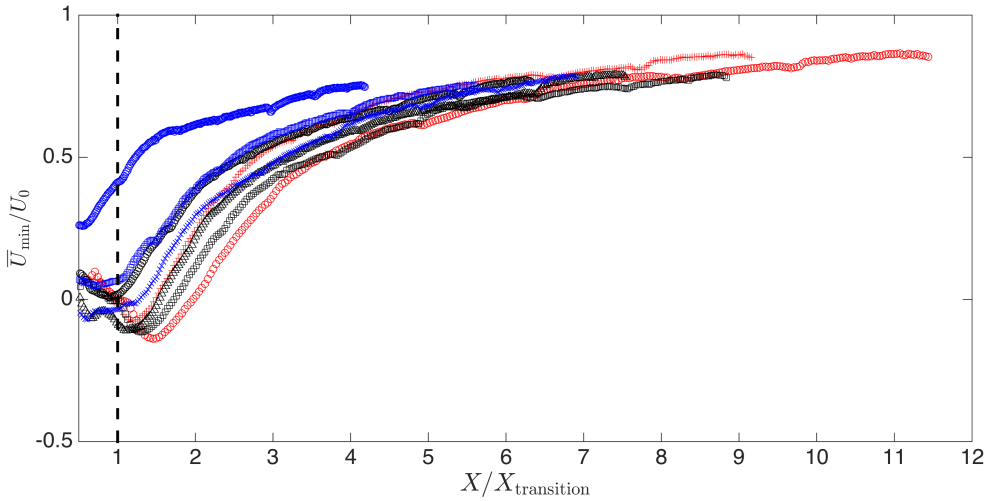

Figure 4.24: Normalized minimum streamwise velocity, $\overline{U}_{\min}/U_0$, versus downstream distance X normalized by the streamwise transition location, $X_{\text{transition}}$. Colors and symbols correspond to the following: the 2-bladed turbine for $\lambda = 1.95(\times)$, $1.61(\square)$, and $1.22(\circ)$, the 3-bladed turbine for $\lambda = 1.63(\square)$, $1.41(\triangle)$, and $1.20(\circ)$, and the 5-bladed turbine for $\lambda = 1.23(\circ)$ and $\lambda = 1.01(+)$.

dynamic solidity, we can rescale the abscissa of the velocity curves by the $X/D_{\text{transition}}$ location as was done before in Figure 4.19. The result of this transformation on the measured minimum velocity (c.f. Figure 4.20) is shown in Figure 4.24. Notably, all of the velocity profiles recover at approximately the same rate, indicated qualitatively by their slope. However, the transformation is incomplete since the ordinate axis was not scaled. Additionally, the imperfect scaling of the abscissa is attributable to the imperfect means used to predict the transition location, i.e., equation 4.2. Most important, however, is that the collapse of the velocity profiles in the transformed coordinate suggests that the bluff body mode is instrumental in the recovery of the velocity deficit, perhaps because it controls the entrainment of energy into the wake.

Furthermore, the collapse suggests the possibility of extracting an equation relating the minimum velocity, $\overline{U}_{\min}/U_0$, to the $X/X_{\text{transition}}$ position in the wake. Invoking Prandtl's mixing length hypothesis, Schlichting (1960) derived an expression for the recovery of the centerline velocity deficit, i.e., the minimum, in the wake of a bluff body. For a two-

Table 4.2: Power law coefficients corresponding to equation 4.3.

Model	σ	λ	σ_D	c_1	c_2	c_3	R^2
cylinder	1	0	1	1.33	-0.956	-0.068	0.983
5-bladed turbine	0.53	1.23	0.756	2.14	-1.095	-0.006	0.998
5-bladed turbine	0.53	1.01	0.703	1.615	-1.149	0.017	0.998
3-bladed turbine	0.32	1.63	0.693	1.71	-0.991	0.013	0.997
3-bladed turbine	0.32	1.41	0.645	1.498	-0.902	-0.021	0.997
3-bladed turbine	0.32	1.20	0.583	1.168	-0.684	-0.098	0.998
2-bladed turbine	0.21	1.95	0.615	1.491	-0.579	-0.277	0.998
2-bladed turbine	0.21	1.61	0.534	1.201	-0.587	-0.199	0.998
2-bladed turbine	0.21	1.22	0.385	0.542	-0.622	0.033	0.987

dimensional wake, this is given as:

$$\frac{u}{U_0} \sim \left(\frac{X}{D}\right)^{-\frac{1}{2}},$$

and for a circular wake (i.e., 3D axisymmetric), as:

$$\frac{u}{U_0} \sim \left(\frac{X}{D}\right)^{-\frac{2}{3}},$$

where $u = U_0 - \overline{U}_{\min}$. Assuming that the maximum velocity deficit in the wake of the VAWT follows the above form, we seek solutions to the following equation:

$$\frac{u}{U_0} = c_1 \left(\frac{X}{X_t}\right)^{c_2} + c_3. \tag{4.3}$$

The coefficients for this power law fit in each case are give in table 4.2. In general, the power law appears to be an excellent fit to the measured data in the transformed coordinate, with an $R^2 \sim 0.99$ in all cases. Note that the curves were fit to the measured data downstream of the absolute minimum in velocity for each case. A curve fit to the cylinder data is also included, but this was done without applying a transformation to its abscissa, since by definition the transition occurs immediately at $X/D = 0$.

Additionally, the exponential coefficients (c_2 in table 4.2) indicate the importance of considering the three-dimensionality of the flow, especially with increasing dynamic solidity. For $\sigma_D < 0.65$, the minimum velocity in the wake increases approximately in proportion

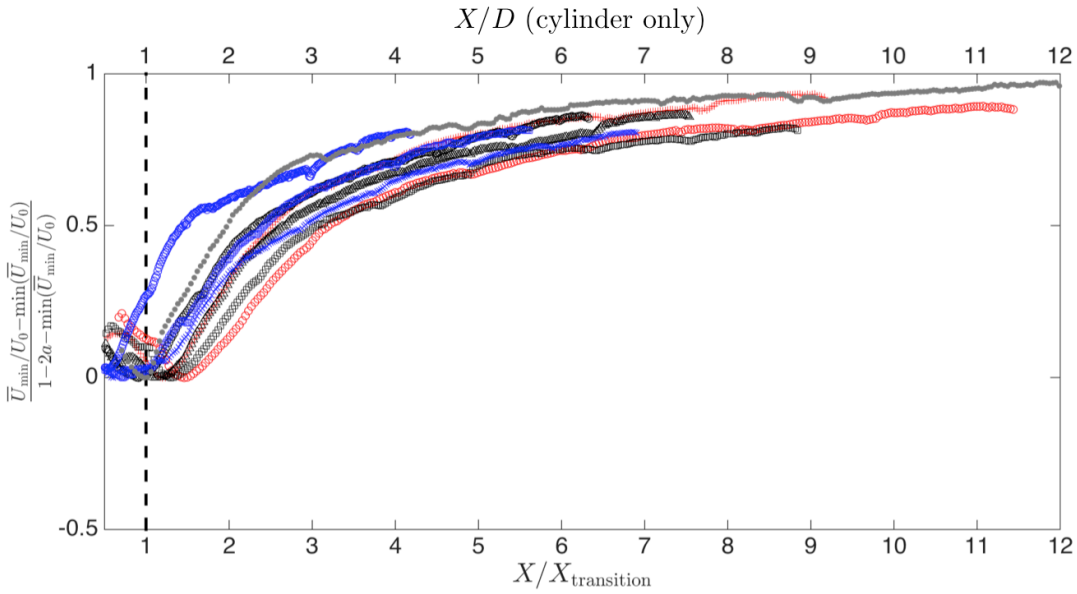

Figure 4.25: Minimum streamwise velocity, $\overline{U}_{\min}$, rescaled by the absolute minimum streamwise velocity across the span, $\min(\overline{U}_{\min})$, and the induction factor, a (derived from the power coefficient, C_p). Downstream distance X is normalized by the streamwise transition location, $X_{\text{transition}}$, for the turbine data, and D for the cylinder. Colors and symbols correspond to the following: the 2-bladed turbine for $\lambda = 1.95(\times)$, $1.61(\square)$, and $1.22(\circ)$, the 3-bladed turbine for $\lambda = 1.63(\square)$, $1.41(\triangle)$, and $1.20(\circ)$, the 5-bladed turbine for $\lambda = 1.23(\circ)$ and $\lambda = 1.01(+)$, and the stationary cylinder $(\bullet)$.

to $X^{-0.6}$, which could perhaps be roughly approximated by the aforementioned theoretical expressions. For $\sigma_D > 0.65$, the minimum velocity in the wake increases approximately in proportion to X^{-1}, including for the cylinder, which is further indication of the similarity between the two flow fields. It also indicates that for small aspect ratio and large dynamic solidity, neither 2D nor 3D-axisymmetric assumptions are valid in the VAWT wake. This is physically consistent with the idea that the finite aspect ratio of the models plays an increasingly dominant role in the wake recovery as the dynamic solidity increases. To this end, the effect of the three-dimensionality of the flow is explored further in the next section.

All of the measured values, including the cylinder data, are plotted in Figure 4.25 with a proposed scaling of the ordinate axis. This rescaling includes subtracting the absolute minimum velocity in each case, $\min(\overline{U}_{\min})$, as well as normalizing by the total velocity deficit recovery, including an induction factor, a, to account for the energy lost from the flow (neglecting viscous losses) in cases where shaft work was done. This induction factor

is derived from the turbine power coefficient, C_p, using actuator disk theory (see, e.g., Hau, 2005), and is given as $C_p = 4a(1-a)^2$. From this, the velocity in the far wake can be approximated as $U/U_0 = 1-2a$. Upon examining Figure 4.25, the closeness of the cylinder data to that of the transformed VAWT data offers another interpretation to this coordinate transformation, which is a mapping of the minimum deficit in the VAWT wake onto that of the cylinder. This suggests that a simplified approach to approximate the wake of a VAWT of arbitrary dynamic solidity could be achieved by applying the inverse transformation to the wake of a stationary cylinder. Although this would not account for effects such as wake asymmetry, it could give a first-order approximation for the velocity deficit recovery.

4.3.6 Insight into three-dimensional effects

Thus far, the analysis has focused exclusively on the 2D PIV measurements. Next we examine the out-of-plane (XZ) PIV measurements to provide insight into the three-dimensionality of the flow, which was suggested in the last section to be significant for high dynamic solidity cases.

Figure 4.26 shows time-averaged PIV measurements of the streamwise and vertical components of velocity, $\overline{U}$ and $\overline{W}$, respectively, for each of the previous experimental cases. These measurements corresponded to a single streamwise position, $X/D = 3.75$, which was located in the middle of the field of view of the XZ-PIV measurements. Also shown for comparison in each plot are measurements of the freestream velocity, taken at the same X/D location, but with the model removed. A fully-developed turbulent boundary layer profile is observed from these freestream measurements. Near the top of the measurement window, there is a slight distortion to the boundary layer profile as the flow tries to adjust to the plexiglass sheet used to dampen free surface effects. This effect on the boundary layer profile is negligible given its limited spatial extent.

Qualitatively, the flow appears nearly symmetric about the midspan for all cases, but with a significant variation of the streamwise velocity along the Z-axis. Despite the large variation in $\overline{U}$ along the height, ranging from approximately 0 to 0.6 U_0, the average vertical velocity never exceeds about 0.07 U_0. This suggests at least two possibilities that may occur

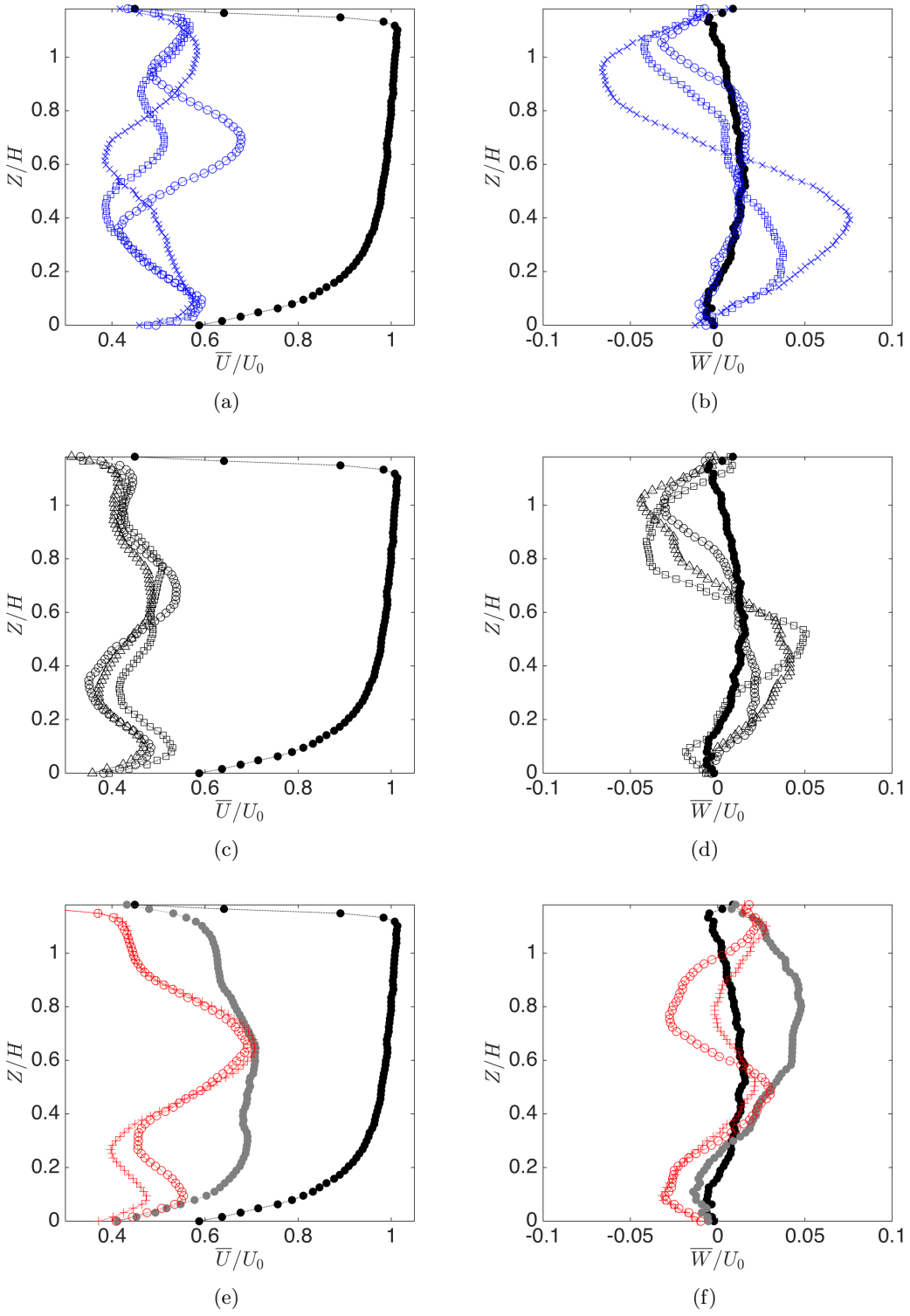

Figure 4.26: Time-averaged PIV measurements of streamwise, $\overline{U}$ (left column), and vertical, $\overline{W}$ (right column), velocity components at $X/D = 3.75$. Measurements are shown along the Z-axis, normalized by the height of the rotor, H, where $Z/H = 0.64$ is at the rotor midspan. The freestream measurements are indicated by solid black circles in each plot. Data in each panel corresponds to the following: (a),(b) the 2-bladed turbine for $\lambda = 1.95(\times)$, $1.61(\square)$, and $1.22(\circ)$; (c),(d) the 3-bladed turbine for $\lambda = 1.63(\square)$, $1.41(\triangle)$, and $1.20(\circ)$; (e),(f) the stationary cylinder $(\bullet)$ and the 5-bladed turbine for $\lambda = 1.23(\circ)$ and $\lambda = 1.01(+)$.

in the experiment related to three-dimensional wake effects. The first is that 3D effects may have dissipated by this downstream position, such that the flow may be reasonably represented by two-dimensional slices at different heights. The second is that since the turbine almost completely fills the height of the channel, the limited space above and below the turbine may have a similar effect on the flow as using end-plates, which tend to suppress three-dimensional effects.

It is interesting to note that the cylinder velocity profile, shown in Figures 4.26(e) and 4.26(f) along with the 5-bladed turbine, appears to recover faster than all the other cases, which is consistent with the previous wake recovery analysis. An important question left to answer, however, is how the Reynolds stresses compare in the different measurement planes, since this is more telling of which direction provides more of a contribution to the wake recovery. The Reynolds stresses, i.e., $< u'v' >$ and $< u'w' >$, at the same X/D location are shown in Figure 4.27 for the cases shown in Figure 4.26. Notable from these figures is that the vertical shear stress, i.e., $< u'w' >$, is roughly the same order as the spanwise shear stress, i.e., $< u'v' >$, but that the maximum shear appears in the uv-plane. This indicates that while the vertical velocity fluctuations play an important role in the dynamics and recovery of the wake, the dominant effect may be characterized by the spanwise fluctuations, as was done in the present analysis.

4.3.7 Rotating cylinder comparison

As a final case to consider, the cylinder was rotated at a fixed $\lambda = 1.7$ and its wake velocity was examined relative to that of the stationary cylinder case. Figure 4.28 shows contours of the time-averaged streamwise component of velocity. In this figure, the magnus effect can readily be observed as a deflection in the wake, which is not unlike the asymmetry in the VAWT wake for large dynamic solidity cases. Figure 4.29 shows the single-point velocity spectra in the wake of the rotating cylinder. From this, it is apparent that in the near wake, the dominant peak in the spectra is more closely aligned with the frequency of the rotation of the cylinder, and only in the very far wake does any dominant peak resemble that of the stationary cylinder, i.e., near $St = 0.2$. This suggests that the rotating cylinder and

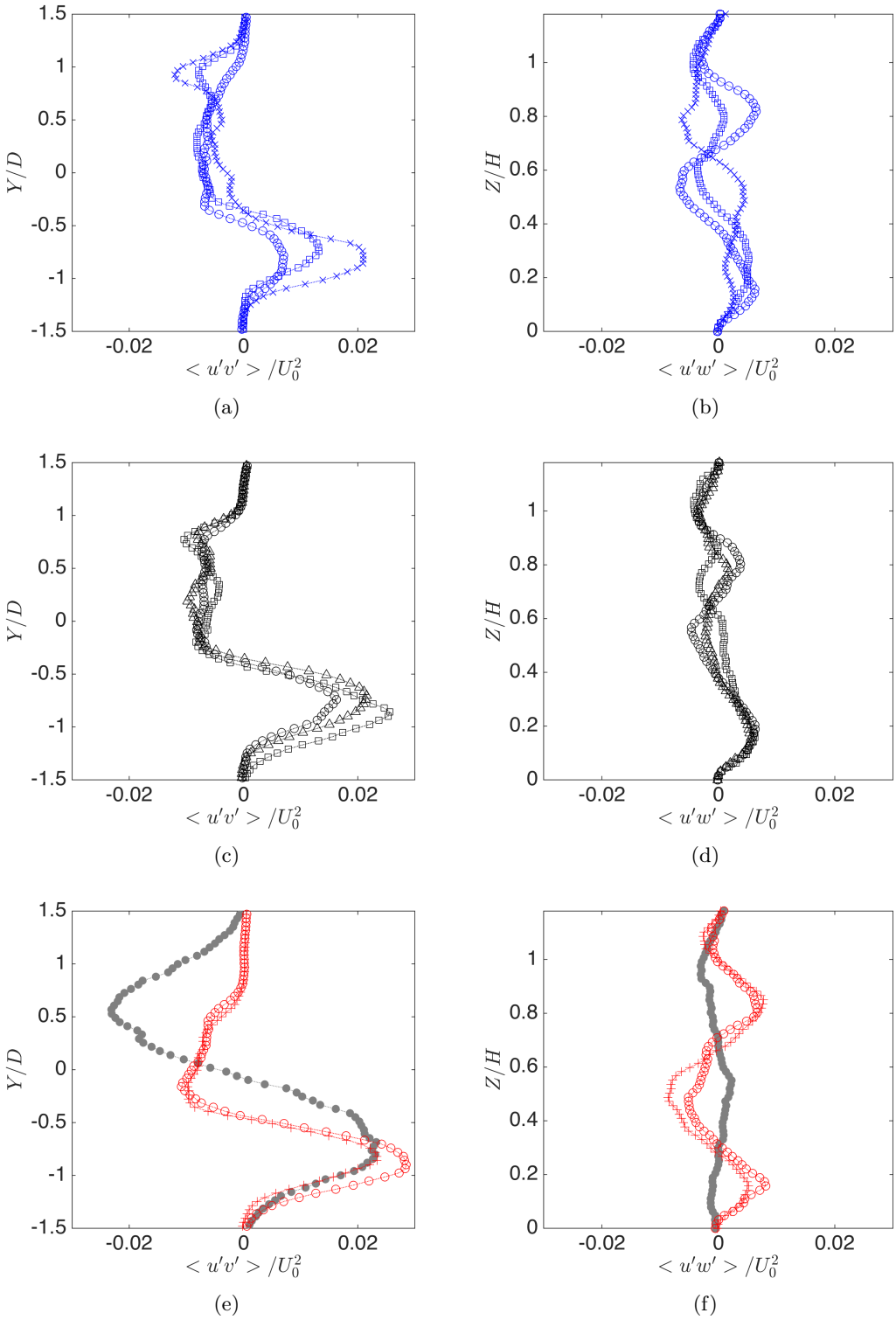

Figure 4.27: PIV measurements of the Reynolds stresses, i.e., $< u'v' >$ and $< u'w' >$, at $X/D = 3.75$. Measurements of $< u'v' >$ (left column) are shown along the Y-axis normalized by the model diameter; measurements of $< u'w' >$ (right column) are shown along the Z-axis, normalized by the height of the rotor, H, where $Z/H = 0.64$ is at the rotor midspan. Data in each panel corresponds to the following: (a),(b) the 2-bladed turbine for $\lambda = 1.95(\times)$, $1.61(\square)$, and $1.22(\circ)$; (c),(d) the 3-bladed turbine for $\lambda = 1.63(\square)$, $1.41(\triangle)$, and $1.20(\circ)$; (e),(f) the stationary cylinder ($\bullet$) and the 5-bladed turbine for $\lambda = 1.23(\circ)$ and $\lambda = 1.01(+)$.

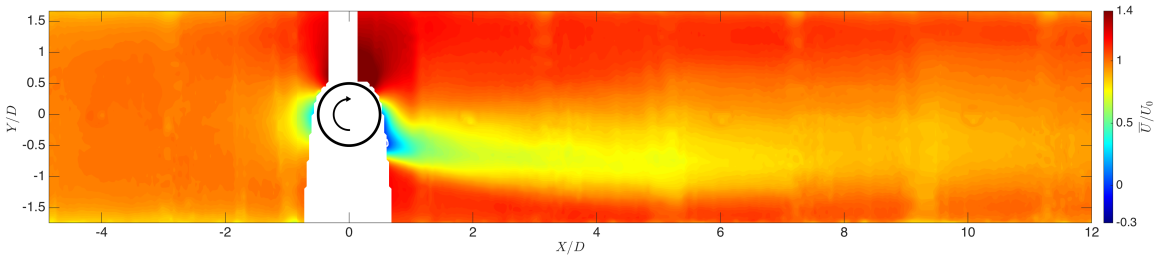

Figure 4.28: Contours of PIV measurements of $\overline{U}/U_0$ for the cylinder rotating at $\lambda = 1.69$.

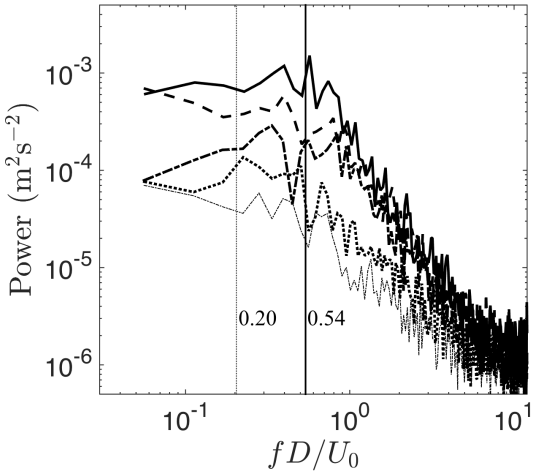

Figure 4.29: Single-point spectra of the velocity fluctuations (v') taken at $X/D = 0.9$ (——), $X/D = 1.7$ (- - -), $X/D = 3.3$ (----), $X/D = 7.3$ (------), and $X/D = 10.0$ (·····) for the rotating cylinder. The solid vertical line corresponds to the rotation rate of the cylinder, and the dotted vertical line to the shedding frequency of the stationary cylinder.

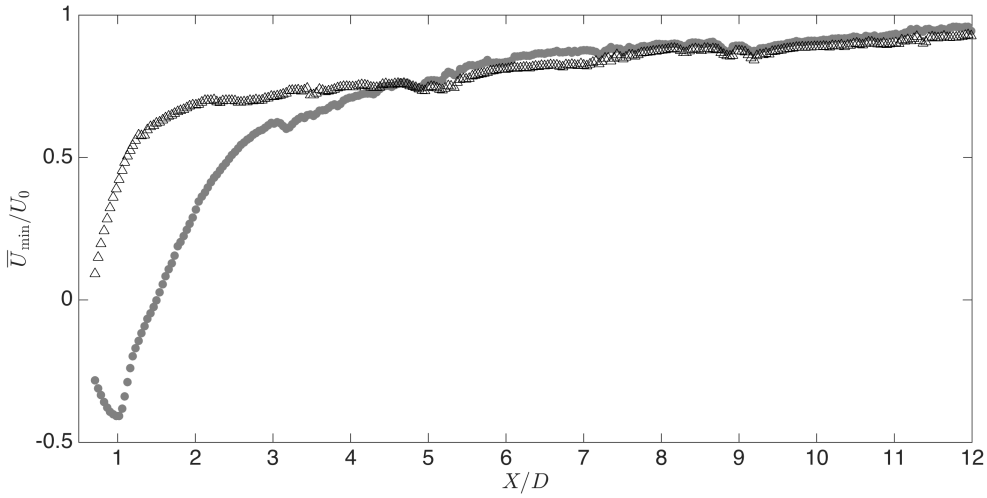

Figure 4.30: Normalized minimum streamwise velocity, $\overline{U}_{\min}/U_0$, versus normalized downstream distance, X/D, for the rotating ($\triangle$) and stationary cylinder ($\bullet$).

the VAWT are similar in the respect that they both modify the local vorticity distribution depending on their rotation rate, and that far downstream the flow again returns to a state where bluff-body oscillations appear, if only briefly for the rotating cylinder. However, the spectral peaks in the rotating cylinder case are generally more diffuse than in the stationary case (c.f. Figure 4.9(d)), which could be an early indication of vortex suppression, as has been observed by others near $\lambda \approx 2$ (Kumar *et al.*, 2011; Chan *et al.*, 2011; Pralits *et al.*, 2010; Mittal & Kumar, 2003). Figure 4.30 shows the recovery of the minimum velocity in the wake of both the rotating and stationary cylinders. It is apparent that the rotation leads to a much faster recovery initially, but that the two velocities recover at approximately the same rate far downstream. This suggests that perhaps a different transformation could be applied to the rotating cylinder data that maps it onto the stationary cylinder wake, thus providing a connection between the VAWT wake and rotating cylinder wake. The issue of the rotating cylinder implicitly adding energy to the flow could perhaps be accounted for by including the negative values of C_p in the rescaling of the velocity. However, this is left to future work as it is beyond the scope of this thesis.

4.4 Concluding remarks

The most important conclusion to be drawn from this chapter is that the dynamics of the VAWT wake can be quantitatively related to that of a solid cylinder. It was shown how this relation may be quantified through a newly defined parameter, the dynamic solidity, σ_D, which is a ratio of characteristic length and time scales within the flow. Spectral analysis of the VAWT wake revealed it to be characterized by two dominant frequencies of velocity fluctuations. The near wake is dominated by the periodic shedding of vortices from the turbine blades, and the far wake exhibits low-frequency oscillations characteristic of bluff bodies, i.e., near $St \approx 0.26$. In between these two regions of the flow, there is a transition, where it is likely that a shear-layer instability develops; this is thought to be the underlying mechanism that leads to the far-wake oscillations in VAWTs just as it does for any other bluff body. The transition location was found to be strongly correlated with σ_D, thus providing a method to predict the wake transition given the turbine geometry and kinematics. In general, increasing σ_D led to an earlier transition in the wake. These observations were supported by a POD analysis of the velocity fluctuations, which gave insight into the physical structure of the most energetic wake oscillations. It was observed that as σ_D was increased, the frequency content and spatial structure of the dominant POD mode approached that of the solid cylinder in the far wake. Furthermore, increasing σ_D consistently led to weaker vortices shed by the turbine. This has interesting parallels to what has been observed in rotating cylinders, where vortex shedding is suppressed when vorticity of sufficient strength is unable to diffuse to the flow outside of closed streamlines, which are formed around the cylinder surface due to its rotation (Mittal & Kumar, 2003).

Additionally, it was found that an earlier transition in the wake was correlated to a greater initial velocity deficit as well as a faster rate of recovery of this deficit. Using σ_D, a transformation was proposed that closely aligned the velocity recovery profiles of the VAWT wake to that of the solid cylinder. In this transformed coordinate system, the minimum velocity recovery closely followed a power law in accordance with the theoretical predictions of Schlichting (1960) for turbulent free-shear flows. For cases with $\sigma_D < 0.65$ the recovery of the minimum velocity was in proportion to $X^{-0.6}$, while for higher dynamic solidity

(including the cylinder) the recovery was proportional to X^{-1}, indicating the importance of 3D effects. The connection between the velocity recovery and the bluff-body oscillations suggests that these oscillations are more conducive to entraining energy into the wake. This is supported by a look at the Reynolds stresses, i.e., $< u'v' >$ and $< u'w' >$, at a fixed streamwise location. It was found that although the vertical shear stress, i.e., $< u'w' >$, is of the same order as the spanwise shear stress, i.e., $< u'v' >$, indicating its importance in the wake recovery, the maximum Reynolds shear stress was consistently found to be in the uv-plane. This indicates that the dominant effect of the velocity fluctuations on the wake recovery can be characterized by the present analysis in the uv-plane. Furthermore, it is reasonable to assume that the aspect ratio of the turbine plays a significant role in the structure of the wake, just as it does for circular cylinders. Therefore, it would be expected that the spanwise (y) fluctuations, which are dominant in the present analysis, would become more significant in the overall wake recovery as aspect ratio is increased.

There is an apparent design tradeoff for a single turbine between extracting more power from the flow and achieving a faster rate of recovery in its wake, the later of which can be estimated by its dynamic solidity. It can be argued that the relevant parameters in optimizing wind farm performance are the total power produced by the farm, the spacing among turbines, and the structural loads on each turbine. For given flow conditions, the independent dimensionless parameters which strongly affect these three metrics are the tip-speed ratio and solidity of each turbine, which are captured together in the definition of dynamic solidity. Therefore, dynamic solidity can serve as a dependent 'tuning parameter' that can be used to predict wake transition for a given turbine with a specified load. This knowledge can then be used to predict wake velocity recovery and fatigue loads on downstream turbines, which serve as feedback in wind farm optimization. Furthermore, the results also suggest a control strategy for influencing the wake recovery, which is to artificially initiate the wake transition leading to bluff-body oscillations. One such method would be to accelerate the decay of the vortices shed by the blades by perhaps either suction or blowing near the turbine. This would potentially allow sooner development of the bluff body mode, thus entraining more energy into the wake, and recovering its deficit at a faster rate.

Chapter 5

Summary and future work

5.1 Summary of thesis contributions

The comprehensive aim of this thesis was to contribute to an understanding of VAWT aerodynamics, particularly as it pertains to wake interactions within a wind farm. To this end, the main contributions of this thesis can be summarized as the following:

1. **Development of the leaky Rankine body (LRB) model of wind farm aerodynamics:** In chapter 2, it was shown how the low-order LRB model was developed. In comparison with full-scale measurements, the model proved to have sufficient accuracy to not only asses differences among individual turbines within an array but also to predict the ranking of performance of unique VAWT arrays. A key conclusion drawn from the results is that there are two primary competing fluid mechanisms within a VAWT array that contribute to the overall performance. This includes turbine blockage, which can locally accelerate the flow adjacent to a turbine and thereby increase the performance of neighboring turbines above their performance in isolation, and the turbine wake, which locally decelerates the flow and leads to a decrease in performance for downstream turbines. A major benefit to using the LRB model is that optimal array configurations can be found with significantly less computational expense than higher fidelity simulations and much more rapidly than in experiments.

2. **Establishment of the appropriate criteria for motor-driven turbine experiments:** A common practice in wind turbine experiments is the use of a motor to actively drive the motion of the turbine blade(s) to achieve kinematic similarity with

what is observed at full-scale. This adds additional forces to the turbine system, which, if left unchecked, can lead to results that are inconsistent with a flow-driven turbine. In chapter 3, particle image velocimetry (PIV) was used to measure the velocity in the near wake of a 3-bladed VAWT under motor-driven and flow-driven conditions. It was shown that motor-driven turbine experiments are justified provided that the net (i.e, time-averaged) torque due to drag does not exceed the net torque due to lift. It was shown that this limit can be determined either by direct measurements of shaft torque or by calculation of the net circulation in the wake, both of which show a sign change above a certain threshold in tip-speed ratio (λ). However, the zero-crossing in torque was suggested to be a more conservative estimate of the λ threshold, since it is often difficult to quantify torque losses, e.g., due to bearing friction, in small-scale VAWT experiments.

3. **Characterization of the near and far wake of a VAWT:** Further PIV experiments at a fixed Reynolds number ($\mathrm{Re} \approx 0.8 \times 10^5$) were conducted to measure the velocity in the wake of a 2-, 3-, and 5-bladed VAWT with fixed aspect ratio, as was detailed in chapter 4. From these measurements, spectral analysis and proper orthogonal decomposition (POD) revealed the VAWT wake to be characterized by three distinct regions of flow: (1) the near wake, where periodic blade vortex shedding dominates; (2) a transition region, where growth of a shear-layer instability occurs; (3) the far wake, where bluff-body wake oscillations dominate. The far-wake characterization is of particular importance for wind farm design due to its practical implications, such as fatigue loads on downstream turbines and energy entrainment.

4. **Establishment of a quantitative connection between the dynamics of the VAWT wake and that of a solid cylinder:** Also presented in chapter 4 were the results of PIV measurements conducted in the wake of a right circular cylinder of the same aspect ratio as the model VAWTs. A new parameter, the dynamic solidity (σ_D), was defined to quantify the combined effect of turbine geometry and rotation on how 'solid' the turbine rotor appears to the incident flow, with $\sigma_D = 1$ equivalent to the rotor appearing as a solid cylinder. Significant correlations were found to show

that increasing σ_D led to an earlier transition, a greater initial velocity deficit, and a faster rate of recovery in the VAWT wake. These observations were supported by a POD analysis of the velocity fluctuations, which showed that as σ_D was increased, the frequency content and spatial structure of the dominant POD mode approached that of the solid cylinder in the far wake. Furthermore, a coordinate transformation was proposed using σ_D in which the velocity recovery profiles of the VAWT wake matched that of the cylinder wake, suggesting that the bluff-body oscillations are more conducive to the entrainment of energy into the wake. The ability to predict the VAWT wake transition may impact the layout of multiple turbines within a wind farm, since bluff-body oscillations may enhance energy entrainment, but may also lead to early fatigue of downstream turbines.

5.2 Avenues for future work

There are several extensions to the work presented in this thesis that were either beyond its scope, or only briefly addressed. The first is to further examine the flow around rotating cylinders as they pertain to VAWTs. In chapter 4, the POD analysis indicated that increasing σ_D consistently led to weaker vortices shed by the turbine, which has interesting similarities to vortex suppression observed in rotating cylinder investigations found in the literature (Kumar *et al.*, 2011; Chan *et al.*, 2011; Pralits *et al.*, 2010; Mittal & Kumar, 2003). A single case of a rotating cylinder was presented in chapter 4, which led to the suggestion that perhaps a different transformation could be applied to the rotating cylinder data that maps it onto the stationary cylinder wake, thus providing a connection between the VAWT wake and rotating cylinder wake. This would give additional merit to the use of a rotating cylinder as a physical model for a VAWT, which is a simple approach that could potentially provide significant insight into the energy exchange within a VAWT wind farm.

Another extension of the current work would be to characterize the VAWT wake as a function of the turbine aspect ratio. Although the three-dimensionality of the flow in the current set of experiments was addressed in chapter 4, the aspect ratio was held fixed among all of the models. From what is known about the flow around circular cylinders, as well

as the established connection between cylinders and VAWTs presented in this thesis, the effect of varying the aspect ratio is expected to play a significant role in the VAWT wake recovery. Related to this extension would be to further examine the three-dimensionality of the flow, including the effect of the height of the flow above/below the turbine as it pertains to the wake recovery. Furthermore, the three-dimensionality of the flow is expected to play a significant role in the wake of VAWTs with curved blades, such as the darrieus or helical blade design, which was not addressed at all in this thesis.

Finally, another direct extension to the work of this thesis would be to use the LRB model to try to find optimal turbine array configurations, or to extend the model to 3D to try to further refine its predictions. Some effort on the former suggestion is already in progress, with plans for future field measurements to support it. An additional benefit to a return to field measurements would be to try to detect the bluff-body oscillations shown to be characteristic of the far wake of a VAWT in this thesis, which could serve to measure its effect on downstream turbines in the field. All of these potential avenues for future work share the common goal of advancing the technology necessary to improve the efficiency of wind farming. This is just one of many socially responsible alternative energy solutions that can have an impact on reducing the negative effects that burning fossil fuels have on human health and the environment.

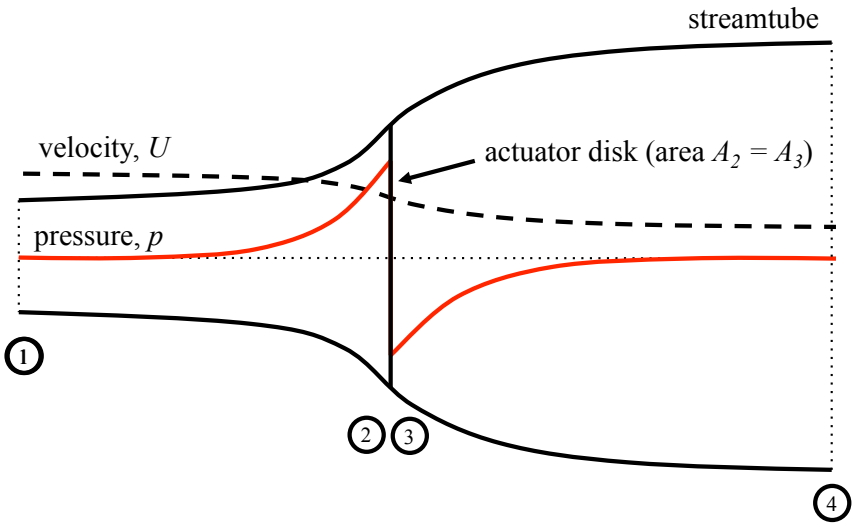

Figure 5.1: Schematic of the flow through a turbine modeled as an actuator disk. The variable streamtube cross-sectional area, velocity, and static pressure fore and aft of the turbine are indicated.

APPENDIX A: DETAILED DEVELOPMENT OF THE LRB MODEL

The purpose of this section is to provide additional background information and details on the development of the LRB model. As introduced in section 2.2, the LRB model is an application of the simplified model of wind turbine aerodynamics known as actuator disk theory (see, e.g., Spera (2009); Hau (2005)). In what follows, actuator disk theory is briefly reviewed and then related to the LRB model via potential flow theory.

In actuator disk theory, the turbine rotor is idealized as a permeable, non-rotating disk and the flow is assumed to be one-dimensional, frictionless, and incompressible. Mass is conserved and thus the velocity is continuous along a streamtube that encompasses the disk. A key assumption of the theory is the presence of a discontinuous pressure drop across the disk, which is an idealization of the mechanical extraction of energy by the turbine. An example schematic of this flow with the corresponding velocity and pressure distribution is shown in Figure 5.1. The lines drawn in this figure are only for illustrative purposes as the theory only stipulates the conditions at stations 1-4. Determination of the full distribution of velocity and pressure requires solution of the equations of fluid motion, e.g. by direct

numerical simulation. Conservation of mass requires that

$$\dot{m} = \rho U_1 A_1 = \rho U_2 A_2 = \rho U_4 A_4, \tag{A1}$$

where U_1, U_2, and U_4, are the flow velocities upstream of the rotor, at the rotor, and in the far wake of the rotor, respectively. Note from Figure 5.1 that $U_3 = U_2$ and $A_3 = A_2$, but that $p_3 < p_2$. Another key assumption of the theory is that the static pressure in the far wake (i.e. station 4) fully recovers to the value upstream (i.e. station 1), or $p_4 = p_1$. Applying Bernoulli's equation from station 1 to 2 and again from station 3 to 4 gives the following two equations for the static pressure directly in front of and behind the disk:

$$p_2 = \frac{1}{2}\rho U_1^2 + p_1 - \frac{1}{2}\rho U_2^2 \tag{A2}$$

$$p_3 = \frac{1}{2}\rho U_4^2 + p_4 - \frac{1}{2}\rho U_3^2. \tag{A3}$$

The magnitude of the force, F, acting on the disk is then $F = (p_2 - p_3)A_2$. By linear momentum conservation it can be shown that

$$\dot{m}(U_4 - U_1) = (p_2 - p_3)A_2. \tag{A4}$$

Combining equations A1 - A4 gives the following result for the velocity directly in front of the rotor:

$$U_2 = \frac{1}{2}(U_1 + U_4). \tag{A5}$$

The axial induction factor, a, is defined as the following:

$$a \equiv \frac{U_1 - U_2}{U_1}. \tag{A6}$$

By algebraic manipulation of equations A5 and A6, it can be shown that

$$U_2 = U_1(1 - a) \tag{A7}$$

$$U_4 = U_1(1 - 2a). \tag{A8}$$

Finally, the power, P, extracted from the flow by the turbine is given by $P = FU_2$, which upon substitution of equations A4 and A5 gives

$$P = \frac{1}{2}\rho A_2 U_2 (U_1^2 - U_4^2). \tag{A9}$$

The turbine power coefficient, C_p, is defined as

$$C_p \equiv \frac{P}{\frac{1}{2}\rho A_2 U_1^3} = 4a(1 - a)^2. \tag{A10}$$

It was shown in section 2.2 that the LRB model assumes that the mean flow around an individual VAWT can be represented by a potential flow consisting of a uniform flow of magnitude V_∞, a potential source of strength m_{so}, and a potential sink of strength m_{si}, with the source and sink separated by a distance s_s. Without loss of generality, it is illustrative to examine the case of a uniform flow of magnitude U_1 in the x-direction and with a source and sink placed along the x-axis. This results in a streamwise velocity along the x-axis, $U(x)$, that is dependent on the strength of the source and sink as well as their spacing. Assuming that the source is located at the origin, this streamwise velocity is given as follows:

$$U(x) = U_1 + \left[\frac{m_{so}}{2\pi x} - \frac{m_{si}}{2\pi(x - s_s)}\right]. \tag{A11}$$

The connection between this potential flow velocity profile and the aforementioned actuator disk theory is in the specification of m_{so} and m_{si} in equation A11. Given the C_p of a particular turbine, the induction factor, a, is immediately known from equation A10. By further specifying the freestream velocity, U_1, the velocity U_2 and U_4 are given by equations A7 and A8, respectively. An important distinction of the LRB model is that the velocity is indeterminate in the region very close to the turbine rotor due to the presence of the singularities. Therefore, it is not possible to sample the velocity directly at the turbine rotor. Instead, the velocity as seen by the rotor, i.e. U_2, is taken as the potential flow velocity just upstream of the turbine center at the position $x = -r_u$ in the LRB model.

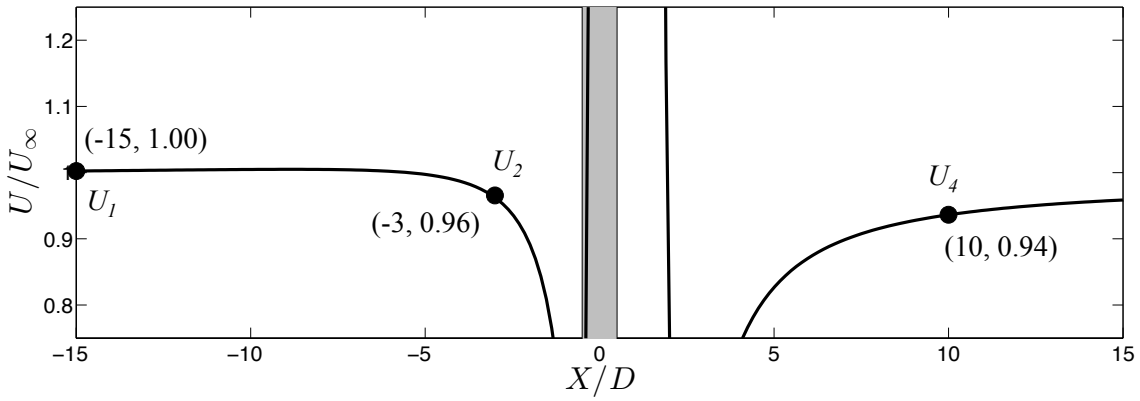

Figure 5.2: Axial velocity distribution for a single VAWT by the LRB model. Gray rectangle indicates turbine position.

Similarly, the far wake velocity, i.e. U_4, is positioned downstream of the turbine center at $x = r_w$. This results in the following system of equations:

$$U(-r_u) = U_2 = U_1 - \frac{m_{so}}{2\pi r_u} + \frac{m_{si}}{2\pi(r_u + s_s)} \tag{A12}$$

$$U(r_w) = U_4 = U_1 + \frac{m_{so}}{2\pi r_w} - \frac{m_{si}}{2\pi(r_w - s_s)}. \tag{A13}$$

Given the sink spacing, s_s, which is calibrated as described in section 2.3, the above system of equations can be solved for m_{so} and m_{si} for a single turbine. Taking $s_s/D = 1.44$, $r_u/D = 3$, and $r_w/D = 10$, the corresponding velocity magnitude (i.e. wind speed) along the x-axis given by the LRB model for a single VAWT is shown in Figure 5.2. In this plot, it can be observed that the velocity as seen by the rotor (U_2) is in accordance with equation A5 derived from actuator disk theory, i.e. $0.96 \approx \frac{1}{2}(1 + 0.94)$.

The primary utility of the LRB model is in assessing the performance of arrays of turbines. To do this, individual turbines within an array are modeled by a superposition of LRBs. By this approach, the resulting flow around each turbine in the array is different from the isolated LRB, which implies that the resultant turbine efficiency, i.e. C_p, is variable. The benefit of superposition is the speed of calculation (e.g. a few seconds for dozens of VAWTs). The tradeoff, however, is that the actual efficiency of each VAWT in the array is ill-defined because there does not exist an objective freestream (i.e. U_1), only the incident

speed U_2. For a single turbine with a given C_p, the turbine power scales as U_1^3, i.e. $P \sim U_1^3$. Since $U_1 = U_2/(1-a)$, and a is nominally a constant, then it can be similarly stated that the turbine power scales as the cube of the incident speed, i.e. $P \sim U_2^3$. Thus, this metric is a suitable choice for making relative, as opposed to absolute predictions of performance among turbine arrays, and it is used in the LRB model for just this purpose.

APPENDIX B

See table 5.1.

Table 5.1: Summary of selected wind turbine experimental and numerical studies.

	HAWT	VAWT	Numerical	Experimental	Flow -driven	Motor -driven	Torque/power reported
Ebert & Wood (1997)	X			X	X		X
Grant & Parkin (2000)	X			X	X		
Xu & Sankar (2000)	X		X			X	
Fujisawa & Shibuya (2001)		X		X		X	
Duque *et al.* (2003)	X		X			X	X
Bahaj *et al.* (2007)	X		X	X	X	X	X
Chao & van Dam (2007)	X		X			X	X
Lida *et al.* (2007)		X	X			X	X
Ferreira *et al.* (2009)		X		X		X	
Howell *et al.* (2010)		X	X	X	X	X	X
Cal *et al.* (2010)	X			X	X		X
Battisti *et al.* (2011)		X		X	X		X
Bazilevs *et al.* (2011)	X		X		X		X
Chamorro *et al.* (2011)	X			X	X		
Hsu & Bazilevs (2012)	X		X		X		X
Li *et al.* (2012)		X	X			X	
Martinelli & Smits (2012)		X	X			X	X
Bachant & Wosnik (2014)		X	X	X	X	X	X
Korobenko *et al.* (2014)		X	X			X	X
Le *et al.* (2014)		X	X		X	X	X
Nini *et al.* (2014)		X	X			X	
Shamsoddin & Porté-Agel (2014)		X	X			X	
Tescione *et al.* (2014)		X		X		X	

APPENDIX C

See figures 5.3 and 5.4.

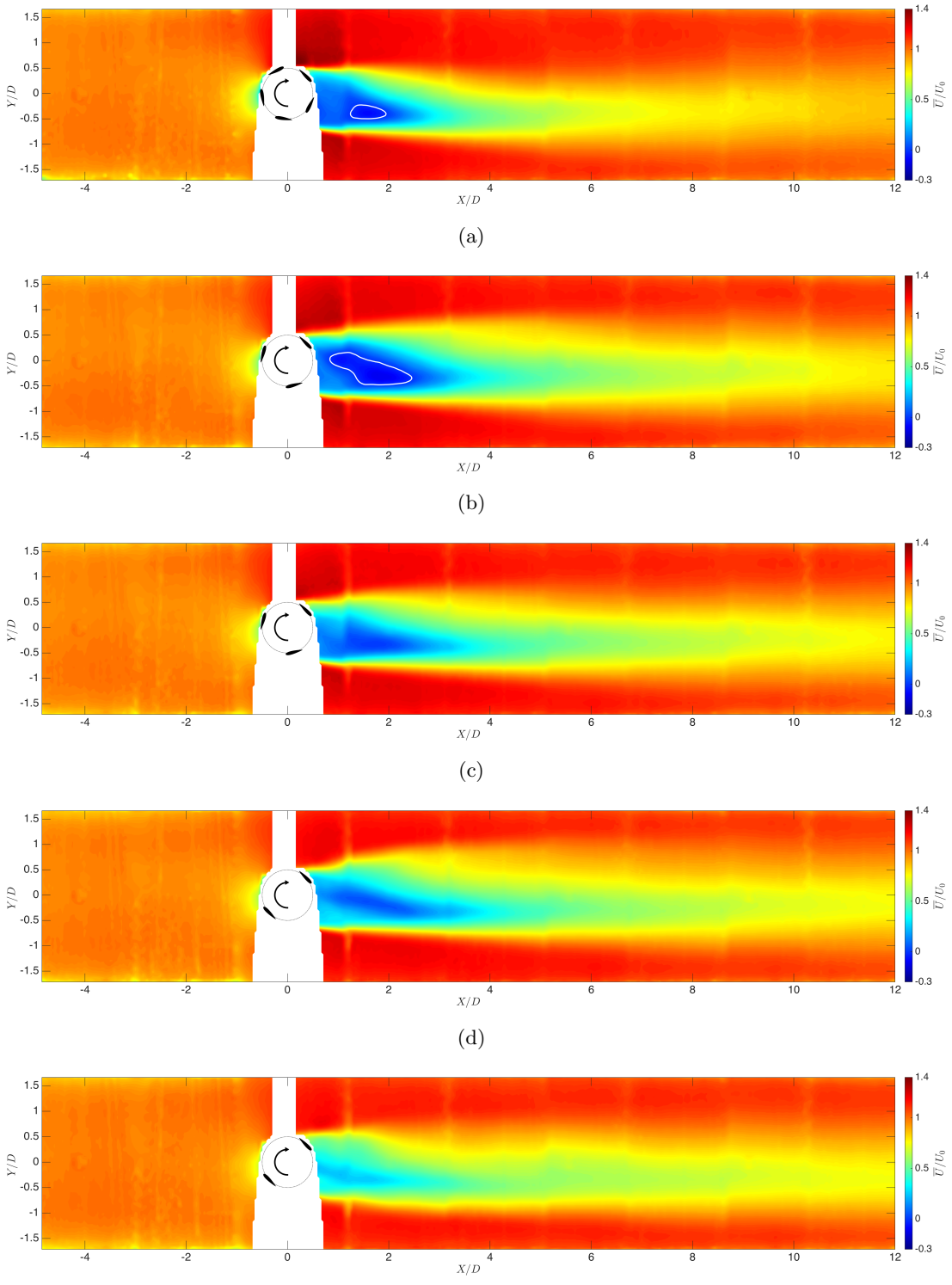

Figure 5.3: Contours of PIV measurements of $\overline{U}/U_0$ under loaded conditions. The plots are in order from top to bottom with decreasing σ_D (c.f. section 4.3.3) and correspond to the (a) 5-bladed VAWT at $\lambda = 1.01$, (b) 3-bladed VAWT for $\lambda = 1.41$, (c) 3-bladed VAWT for λ=1.20, (d) 2-bladed VAWT for $\lambda = 1.61$, and (e) 2-bladed VAWT for $\lambda = 1.22$. Airfoil cross-sections for the turbines are drawn to scale.

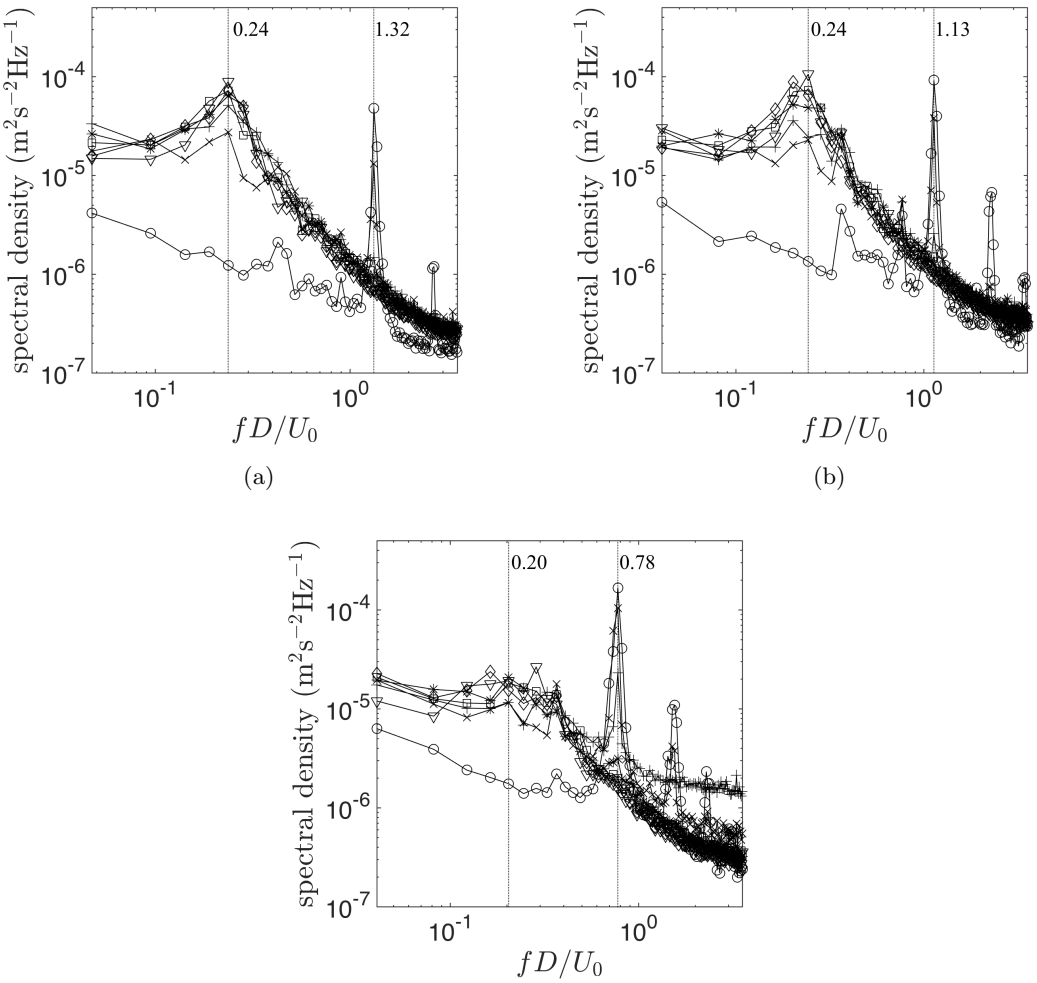

Figure 5.4: Spectra of the time-varying amplitude of the dominant POD mode for the velocity fluctuations under loaded conditions. The figures correspond to (a) the 3-bladed VAWT at $\lambda = 1.41$, (b) the 3-bladed VAWT at $\lambda = 1.20$, and (c) the 2-bladed VAWT at $\lambda = 1.22$. Each spectrum corresponds to PIV window 3 ($\circ$), 4 ($\times$), 5 ($+$), 6 ($*$), 7 ($\square$), 8 ($\diamond$) and 9 ($\triangledown$). Dotted vertical lines correspond to the selected near and far-wake frequencies of the maximum amplitude in the spectra.

Bibliography

Ammara, Idriss, Leclerc, Christophe & Masson, Christian 2002 A viscous three-dimensional differential/actuator-disk method for the aerodynamic analysis of wind farms. *J. Sol. Energ.* **124**, 345.

Araya, Daniel B., Colonius, Tim & Dabiri, John O. 2015 Transition to bluff body dynamics in the wake of vertical-axis wind turbines. *submitted* .

Araya, Daniel B., Craig, Anna E., Kinzel, Matthias & Dabiri, John O. 2014 Low-order modeling of wind farm aerodynamics using leaky Rankine bodies. *J. Renewable Sustainable Energy* **6**, 063118.

Araya, Daniel B. & Dabiri, John O. 2015 A comparison of wake measurements in motor-driven and flow-driven turbine experiments. *Exp. Fluids* **56** (7), 1–15.

Bachant, P. & Wosnik, M. 2014 Reynolds number dependence of cross-flow turbine performance and near-wake characteristics. In *Proceedings of the 2nd Marine Energy Technology Symposium*. Seattle, WA.

Bachant, Peter & Wosnik, Martin 2015 Characterising the near-wake of a cross-flow turbine. *J. Turbul.* **16** (4), 392–410.

Bahaj, A.S., Batten, W.M.J. & McCann, G. 2007 Experimental verifications of numerical predictions for the hydrodynamic performance of horizontal axis marine current turbines. *Renew. Energ.* **32**, 2479–2490.

Batchelor, G. K. 1967 *An Introduction to Fluid Dynamics*. Cambridge University Press.

Battisti, L., Zanne, L., Anna, S. Dell', Dossena, V., Persico, G. & Paradiso, B. 2011 Aerodynamic measurements on a vertical axis wind turbine in a large scale wind tunnel. *J. Energ. Resour.* **133**, 031201.

Bazilevs, Y., Hsu, M. C., Kiendl, J., Wüchner, R. & Bletzinger, K.-U. 2011 3D simulation of wind turbine rotors at full scale. Part II: Fluid-structure interaction modeling with composite blades. *Int. J. Numer. Meth. Fl.* **65**, 236–253.

Berkooz, Gal, Holmes, Philip & Lumley, John L. 1993 The proper orthogonal decomposition in the analysis of turbulent flows. *Annu. Rev. Fluid Mech.* **25**, 539–575.

Betz, A. 1920 Das maximum der theoretisch möglichen ausnützung des windes durch windmotoren. *Zeitschrift für das gesamte Turbinenwesen* **26**, 307.

Birkhoff, Garrett & Zarantonello, E. H. 1957 *Jets, Wakes, and Cavities*. Academic Press Inc.

Cal, Raúl Bayoán, Lebrón, José, Castillo, Luciano, Kang, Hyung Suk & Meneveau, Charles 2010 Experimental study of the horizontally averaged flow structure in a model wind-turbine array boundary layer. *J. Renewable Sustainable Energy* **2**, 013106.

Calaf, M., Meneveau, C. & Meyers, J. 2010 Large eddy simulation study of fully developed wind-turbine array boundary layers. *Phys. Fluids* **22**, 015110.

Chamorro, Leonardo P., Arndt, R. E. A. & Sotiropoulos, Fotis 2011 Turbulent flow properties around a staggered wind farm. *Bound.-Lay. Meteorol.* **141**, 349–367.

Chamorro, Leonardo P. & Porté-Agel, Fernando 2010 Effects of thermal stability and incoming boundary-layer flow characteristics on wind-turbine wakes: a wind-tunnel study. *Bound.-Lay. Meteorol.* **136** (3), 515.

Chan, A. S., Dewey, Peter A., Jameson, A., Liang, C. & Smits, A. J. 2011 Vortex suppression and drag reduction in the wake of counter-rotating cylinders. *J. Fluid Mech.* **679**, 343–382.

Chao, D. D. & van Dam, C. P. 2007 Computational aerodynamic analysis of a blunt trailing-edge airfoil modification to the NREL Phase VI rotor. *Wind Energy* **10**, 529–550.

Choi, Haecheon, Jeon, Woo-Pyung & Kim, Jinsung 2008 Control of flow over a bluff body. *Annu. Rev. Fluid Mech.* **40**, 113–139.

Dabiri, John & Brownstein, Ian 2015 Optimization of wind farm performance using low-order models [Abstract]. In *Proceedings of the 68th annual meeting of the APS Division of Fluid Dynamics*. Boston, MA.

Dabiri, J. O. 2011 Potential order-of-magnitude enhancement of wind farm power density via counter-rotating vertical-axis wind turbine arrays. *J. Renewable Sustainable Energy* **3**, 043104.

Dawson, C. W. 1977 A practical computer method for solving ship-wave problems. In *Proceedings of Second International Conference on Numerical Ship Hydrodynamics*, pp. 30–38.

Dunne, Reeve & McKeon, Beverley J. 2015 Dynamic stall on a pitching and surging airfoil. *Exp. Fluids* **56** (8), 1–15.

Duque, Earl P.N., Burklund, Michael D. & Johnson, Wayne 2003 Navier-Stokes and comprehensive analysis performance predictions of the NREL phase VI experiment. *J. Sol. Energ.* **125**, 457–467.

Ebert, P. R. & Wood, D.H. 1997 The near wake of a model horizontal-axis wind turbine - I. Experimental arrangements and initial results. *Renew. Energ.* **12**, 225–243.

Edwards, Jonathan M., Danao, Louis Angelo & Howell, Robert J. 2015 PIV measurements and CFD simulation of the performance and flow physics and of a small-scale vertical axis wind turbine. *Wind Energy* **18**, 201–217.

Feng, Li-Hao, Wang, Jin-Jun & Pan, Chong 2011 Proper orthogonal decomposition analysis of vortex dynamics of a circular cylinder under synthetic jet control. *Phys. Fluids* **23**, 014106.

Ferreira, C. S., van Kuik, G., van Bussel, G. & Scarano, F. 2009 Visualization by PIV of dynamic stall on a vertical axis wind turbine. *Exp. Fluids* **46**, 97–108.

Fujisawa, N. & Shibuya, S. 2001 Observations of dynamic stall on Darrieus wind turbine blades. *J. Wind Eng. Ind. Aerod.* **89**, 201–214.

Grant, I. & Parkin, P. 2000 A DPIV study of the trailing vortex elements from the blades of a horizontal axis wind turbine in yaw. *Exp. Fluids* **28**, 368–376.

Haggett, Claire 2008 Over the sea and far away? A consideration of the planning, politics and public perception of offshore wind farms. *J. Environ. Pol. Plan.* **10** (3), 289–306.

Hansen, M. O. L., Sørensen, J. N., Voutsinas, S., Sørensen, N. & H. Aa. Madsen 2006 State of the art in wind turbine aerodynamics and aeroelasticity. *Prog. Aerosp. Sci.* **42**, 285.

al Hassan, Ahmad Y. & Hill, Donald R. 1986 *Islamic Technology: An Illustrated History*.

Hau, E. 2005 *Wind Turbines*, 2nd edn. Springer Verlag, Berlin.

Hess, J. L. 1990 Panel methods in computational fluid dynamics. *Annu. Rev. Fluid Mech.* **22**, 255.

Howell, Robert, Qin, Ning, Edwards, Jonathan & Durrani, Naveed 2010 Wind tunnel and numerical study of a small vertical axis wind turbine. *Renew. Energ.* **35**, 412–422.

Hsu, Ming-Chen & Bazilevs, Yuri 2012 Fluid-structure interaction modeling of wind turbines: simulating the full machine. *Comput. Mech.* **50**, 821–833.

Islam, Mazharul, Ting, David S.-K. & Fartaj, Amir 2008 Aerodynamic models for Darrieus-type straight-bladed vertical axis wind turbines. *Renew. Sust. Energ. Rev.* **12** (4), 1087.

Iungo, G. V., Viola, F., Camarri, S., Porté-Agel, F. & Gallaire, F. 2013 Linear stability analysis of wind turbine wakes performed on wind tunnel measurements. *J. Fluid Mech.* **737**, 499–526.

Kang, Hyung Suk & Meneveau, Charles 2010 Direct mechanical torque sensor for model wind turbines. *Meas. Sci. Technol.* **21**, 105206.

Kinzel, M., Mulligan, Q. & Dabiri, J. O. 2012 Energy exchange in an array of vertical-axis wind turbines. *J. Turbul.* **13** (38), 1.

Korobenko, A., Hsu, M. C., Akkerman, I. & Bazilevs, Y. 2014 Aerodynamic simulation of vertical-axis wind turbines. *J. Appl. Mech.* **81**, 021011.

Kumar, S., Cantu, C. & Gonzalez, B. 2011 Flow past a rotating cylinder at low and high rotation rates. *J. Fluids Eng.* **133**, 041201.

Lam, K. M. 2009 Vortex shedding flow behind a slowly rotating circular cylinder. *J. Fluid. Struct.* **25**, 245–262.

Laneville, A. & Vittecoq, P. 1986 Dynamic stall: The case of the vertical axis wind turbine. *J. Sol. Energ. Eng.* **108**, 140–145.

Le, Tuyen Quang, Lee, Kwang-Soo, Park, Jin-Soon & Ko, Jin Hwan 2014 Flow-driven rotor simulation of vertical axis tidal turbines: A comparison of helical and straight blades. *Int. J. Nav. Archit. Ocean Eng.* **6**, 257–268.

Li, Zhi Chuan, Sheng, Qi Hu, Zhang, Liang, Cong, Zhi Ming & Jiang, Jin 2012 Numerical simulation of blade-wake interaction of vertical axis tidal turbine. *Adv. Mat. Res.* **346**, 318–323.

Lida, Akiyoshi, Kato, Keiichi & Mizuno, Akisato 2007 Numerical simulation of unsteady flow and aerodynamic performance of vertical axis wind turbines with LES. In *Proceedings of the 16th Australasian Fluid Mechanics Conference*. Gold Coast, Australia.

Lissaman, P. B. S. 1979 Energy effectiveness of arbitrary arrays of wind turbines. *J. Energy* **3** (6), 323.

Lissaman, P. B. S., Gyatt, G. W. & Zalay, A. D. 1982 Numeric modeling sensitivity analysis of the performance of wind turbine arrays. *Tech. Rep.* PNL-4183. Pacific Northwest Laboratory.

Marmidis, Grigorios, Lazarou, Stavros & Pyrgioti, Eleftheria 2008 Optimal placement of wind turbines in a wind park using Monte Carlo simulation. *Renew. Energ.* **33** (7), 1455.

Martinelli, Luigi & Smits, Alexander J. 2012 High-fidelity computational fluid dynamics (CFD) for the wind/tidal energy industry. In *Proceedings of the HKIE Civil Division International Conference*. Hong Kong.

Meyers, Johan & Meneveau, Charles 2012 Optimal turbine spacing in fully developed wind-farm boundary layers. *Wind Energy* **15**, 305.

Milne-Thomson, L. M. 1960 *Theoretical Hydrodynamics*. The Macmillan Company.

Mittal, Sanjay & Kumar, Bhaskar 2003 Flow past a rotating cylinder. *J. Fluid Mech.* **476**, 303–334.

Nini, Michele, Motta, Valentina, Bindolino, Giampiero & Guardone, Alberto 2014 Three-dimensional simulation of a complete Vertical Axis Wind Turbine using overlapping grids. *J. Comput. Appl. Math.* **270**, 78–87.

Porté-Agel, Fernando, Wu, Yu-Ting & Chen, Chang-Hung 2013 A numerical study of the effects of wind direction on turbine wakes and power losses in a large wind farm. *Energies* **6**, 5297–5313.

Pralits, Jan O., Brandt, Luca & Giannetti, Flavio 2010 Instability and sensitivity of the flow around a rotating circular cylinder. *J. Fluid Mech.* **650**, 513–536.

Protas, Bartosz 2008 Vortex dynamics models in flow control problems. *Nonlinearity* **21**, R203.

Rajagopalan, R. Ganesh, Rickerl, Ted L. & Klimas, Paul C. 1990 Aerodynamic interference of vertical axis wind turbines. *J. Propul. Power* **6** (5), 645.

Rankine, W. J. M. 1865 On the mechanical principles of the action of propellers. *Transactions of the Instititue of Naval Architects* **6**, 13.

Raupach, M. R., Marland, G., Ciais, P., Quéré, C. L., Canadell, J. G., Klepper, G. & Field, C. B. 2007 Global and regional drivers of accelerating CO_2 emissions. *Proc. Natl. Acad. Sci.* **104**, 10288.

Richter, Burton 2014 *Beyond smoke and mirrors: Climate change and energy in the 21st century*, 2nd edn. Cambridge University Press.

Rolin, V. & Porté-Agel, F. 2015 Wind-tunnel study of the wake behind a vertical axis wind turbine in a boundary layer flow using stereoscopic particle image velocimetry. *J. Phys.: Conf. Ser.* **625**, 012012.

Roshko, Anatol 1961 Experiments on the flow past a circular cylinder at very high reynolds number. *J. Fluid Mech.* **10**, 345–356.

Schlichting, Hermann 1960 *Boundary Layer Theory*, 4th edn. McGraw-Hill Book Company, Inc.

Shamsoddin, Sina & Porté-Agel, Fernando 2014 Large eddy simulation of vertical axis wind turbine wakes. *Energies* **7**, 890–912.

Sirovich, Lawrence 1987 Turbulence and the dynamics of coherent structures part I: coherent structures. *Q. Appl. Math.* **XLV**, 561–571.

Spera, David A., ed. 2009 *Wind Turbine Technology: Fundamental Concepts of Wind Turbine Engineering*, 2nd edn. ASME Press.

Sutherland, Herbert J., Berg, Dale E. & Ashwill, Thomas D. 2012 A restrospective of VAWT technology. *Tech. Rep.* SAND2012-0304. Sandia National Laboratories.

Templin, R. J. 1974 Aerodynamic performance theory for the NRC vertical-axis wind turbine. Technical Report LTR-LA-160. National Aeronautical Establishment Laboratory.

Tescione, G., Ragni, D., He, C., Ferreira, C. J. Simão & van Bussel, G.J.W. 2014 Near wake flow analysis of a vertical axis wind turbine by stereoscopic particle image velocimetry. *Renew. Energ.* **70**, 47–61.

Theunissen, R., Sante, A. Di, Riethmuller, M. L. & den Braembussche, R. A. Van 2008 Confidence estimation using dependent circular block bootstrapping: application to the statistical analysis of PIV measurements. *Exp. Fluids* **44**, 591–596.

Touryan, K. J., Strickland, J. H. & Berg, D. E. 1987 Electric power from vertical-axis wind turbines. *J. Propul. Power* **3** (6), 481.

Tsai, Hsieh-Chen & Colonius, Tim 2014 Coriolis effect on dynamic stall in a vertical axis wind turbine at moderate Reynolds number. In *proceedings of the 32nd AIAA Applied Aerodynamics Conference*.

U.S. Environmental Protection Agency 2015 Clean Power Plan.

Vasconcelos, G. L., Moura, M. N. & Schakel, A. M. J. 2011 Vortex motion around a circular cylinder. *Phys. Fluids* **23**, 123601.

Welch, Peter D. 1967 The use of fast Fourier transform for the estimation of power spectra: a method based on time averaging over short, modified periodograms. *IEEE Trans. Audio Electroacoust.* **15**, 70–73.

Whittlesey, Robert W. & Dabiri, John O. 2013 Optimal vortex formation in a self-propelled vehicle. *J. Fluid Mech.* **737**, 78–104.

Whittlesey, R. W., Liska, S. & Dabiri, J. O. 2010 Fish schooling as a basis for vertical axis wind turbine farm design. *Bioinsp. Biomim.* **5**, 035005.

Wu, T. Yao-Tsu 1962 A wake model for free-streamline flow theory Part 1. Fully and partially developed wake flows and cavity flows past an oblique flat plate. *J. Fluid Mech.* **13**, 161.

Xu, Guanpeng & Sankar, Lakshmi N. 2000 Computational study of horizontal axis wind turbines. *J. Sol. Energ.* **122**, 35–39.

Yang, Di, Meneveau, Charles & Shen, Lian 2014 Large-eddy simulation of offshore wind farm. *Phys. Fluids* **26**, 025101.

Zhang, Bao-ji, Ma, Kun & Ji, Zhuo-shang 2009 The optimization of the hull form with the minimum wave making resistance based on Rankine source method. *J. Hydrodyn.* **21**, 277.